UC Riverside

UC Riverside Electronic Theses and Dissertations

Title

Frustrated Magnetism in Low-Dimensional Lattices

Permalink

https://escholarship.org/uc/item/60d7j4nv

Author

Tovar, Mayra

Publication Date

2011

Peer reviewed|Thesis/dissertation

eScholarship.org Powered by the California Digital Library
University of California

UNIVERSITY OF CALIFORNIA
RIVERSIDE

Frustrated Magnetism in Low-Dimensional Lattices

A Dissertation submitted in partial satisfaction
of the requirements for the degree of

Doctor of Philosophy

in

Physics

by

Mayra Tovar

June 2011

Dissertation Committee:

Dr. Kirill Shtengel, Chairperson
Dr. Shan-Wen Tsai
Dr. Vivek Aji

Copyright by
Mayra Tovar
2011

The Dissertation of Mayra Tovar is approved:

Committee Chairperson

University of California, Riverside

Acknowledgments

First, I would like to thank my advisor, Dr. Kirill Shtengel, for allowing me the opportunity to work under his guidance. I want to thank him for his help, dedication, imparted knowledge, patience and trust on me. I want to express my profound gratitude also for his encouragement during my doubtful moments; it was very uplifting. Throughout the years under his counsel, Kirill offered me a friendly environment where talking to him was always a great experience. I hope to become one day like him, very involved in science and having such an extensive network of colleagues. ¡Gracias Kirill!

I would also like to thank Dr. Kumar Raman for his collaboration in the project leading up to my first paper. I am very grateful for his cordial disposition to clear out my doubts when the need came. I also thank my committee members, Dr. Shan-Wen Tsai and Dr. Vivek Aji. They are inspirational individuals whose professional careers instigate one to emulate. I have to thank Dr. Tsai too for not finding my occasional knocks on her door importunistic.

My gratitude extends beyond the boundaries of UCR. I am specially and genuinely thankful to Dr. Paul Canfield for his help and great counsel; thanks to his listening and actions, taking an important decision was easier. Other figures who played an important role in my academic success include Mrs. Betty Hornung, Dr. Cristina Cadavid, Dr. Nicolas Kioussis, Dr. Julio Blanco and Dr. Matthew Penn. Each and everyone of them helped to shape my path towards what I believe has been a thriving ending.

I am leaving school not only with a degree, but with the strongest friendships in my life, ever! Graduate school without friends is simply not a possibility. To say that I won't miss the people with whom I shared six years of my life on a daily basis, again, is not possible. My thanks and love go out to my dear friends, my physics family: My wonderful sisters Hülya, Hsiang-Ku and Ling; *the guys*, Vincent, Kyungwook, Peng and Nick. It was such an honor and

privilege sharing office with them. Their company, support, advice, laughters, their wonderful personalities, everything just added up for an unforgettable and memorable experience. I am forever indebted to each and every one of them for being with me always and helping me from beginning to end in this endeavor. They will always be in my heart!

And of course, the source of my strength and support throughout these years couldn't be other but my family. At times, being away from family became lonely. However, even at a distance, my family was and has always been very close to me. My parents, Amador and Maria de Jesus, have always had for me unconditional love. They always told me the right words to make me feel good and persevere. I thank them for believing in me. My brothers, Esau, Ismael and Amador (*Madito*), were always there too to give me an embrace and tell me how proud they were of me; their love drove me forward. I want to specially thank my beautiful little sister Alba, *mi manis*, for always being just a call away from me. Distance was never an obstacle to be close to her. She has always stood by my side, and her love and encouragement have been crucial for my success. Thanks also to my sisters-in-law Mariana and Yeni for sharing with me moments of enjoyment and relaxation. I certainly cannot leave out a special mention of my nieces and nephews: their candid smiles have brought spring to me the year round! And last, but not least, I want to express my love and appreciation to my dear husband Abel. His coming into my life in the last years of school brought a new light and a new energy that revitalized my perspective in life. Thanks to him, I learned that there is more beyond school. I want to thank him for his steadfast company, his understanding, his openness, his support, his invigorating words of advice, his patience, his disposition, and his infinite love: everything has meant so much to me!

Dedico esta disertación a mis papás, agradeciéndoles todo su amor y apoyo durante todos estos años. ¡Los quiero mucho!

ABSTRACT OF THE DISSERTATION

Frustrated Magnetism in Low-Dimensional Lattices

by

Mayra Tovar

Doctor of Philosophy, Graduate Program in Physics
University of California, Riverside, June 2011
Dr. Kirill Shtengel, Chairperson

In this dissertation we present the results of a theoretical investigation of spin models on two-dimensional and quasi one-dimensional lattices, all unified under the concept of quantum frustrated antiferromagnetism, and all discussing various aspects of the antiferromagnetic Heisenberg model on the kagomé lattice. In the Introduction (Chapter 1), we discuss at some length such concepts as frustration and superexchange, among others, which are of common relevance in the rest of the chapters. In Chapter 2, we study the effect of Dzyaloshinskii–Moriya (DM) interactions on the zero-temperature magnetic susceptibility of systems whose low energy can be described by valence bond states. Our work shows that this treatment is consistent with the experimentally observed non-vanishing susceptibility – in the specified temperature limit – of the spin-1/2 kagomé antiferromagnetic compound $ZnCu_3(OH)_6Cl_2$, also known as herbertsmithite. Although the objective of this work is explaining the aforementioned characteristic of the experimental system, our methods are more general and we apply them to the checkerboard and Shastry-Sutherland lattices as well. In Chapter 3, we discuss our findings in the study of ghost-mediated domain wall interactions in the diamondback ladder. These domain walls are spin excitations – the kinks and the antikinks – separating degenerate ground states along one chain of the ladder. While as individual entities an antikink is energetically costly and a kink

energetically free, our study finds that both interact via *ghosts* that they produce in the opposite side of the ladder. Through the study of these ghosts, we find that domain walls proliferate in the system above a critical value of the system's coupling constants. This proliferation makes their treatment as free, non-interacting particles impossible, so we study here their interactions both quantitatively and qualitatively in the region below the critical point where interactions can be treated perturbatively. Based on the calculated two-body interaction potential, domain walls interact attractively (repulsively) when separated by even (odd) distances, with a strength that decays as $1/s^p$, where s is their separation and $p < 1$. In the last chapter, Chapter 4, we present our study of the spin-1 kagomé Heisenberg antiferromagnet. Our approach is to first consider an SU(2)-symmetric parent Hamiltonian with known ground states on the $S = 1$ kagomé lattice, in which nearest-neighbor Heisenberg interactions are already present. We then enhance these interactions by an additional Heisenberg term added perturbatively in order to move the system closer to a pure Heisenberg antiferromagnet. The results of this enhancement is obtaining a description of the system in terms of an effective Hamiltonian, which we use to analyze the possible valence bond ground state of the system.

Contents

List of Figures xi

List of Tables xiii

1 Introduction 1
- 1.1 Frustration . . . 3
- 1.2 Unconventional phases . . . 6
- 1.3 Superexchange . . . 8
  - 1.3.1 Heisenberg Hamiltonian . . . 8
  - 1.3.2 Dzyaloshinskii-Moriya Interaction . . . 9

2 Dzyaloshinskii–Moriya Interactions in Valence Bond Systems 12
- 2.1 Introduction . . . 12
  - 2.1.1 Motivation . . . 13
- 2.2 Model and Formalism . . . 16
  - 2.2.1 Dimer basis and overlap expansion . . . 17
  - 2.2.2 Perturbation theory for the magnetic susceptibility . . . 19
    - 2.2.2.1 Assumptions of the unperturbed Hamiltonian . . . 20
    - 2.2.2.2 Derivation of the susceptibility χ . . . 21
- 2.3 Application to the Shastry-Sutherland model of $SrCu_2(BO_3)_2$ . . . 34
  - 2.3.1 SS Model . . . 35
  - 2.3.2 Comparison with experiment . . . 38
- 2.4 Application to the generalized Klein model on the checkerboard lattice . . . 40
- 2.5 Application to the kagomé lattice and $ZnCu_3(OH)_6Cl_2$ . . . 43
  - 2.5.1 Model . . . 44
  - 2.5.2 Comparison with experiment . . . 47
- 2.6 Discussion . . . 48

3 Ghost-Mediated Interactions Between Domain Walls in the Diamondback Ladder 52
- 3.1 Introduction . . . 52
- 3.2 Model . . . 56
  - 3.2.1 Decoupling the diamondback ladder's chains by perturbation theory . . . 56
- 3.3 Methodology . . . 59
- 3.4 Self-energy calculations of the kinks, antikinks, and their ghosts . . . 60
  - 3.4.1 Energy of a single defect . . . 60

3.4.2 Proliferation of domain walls . . . 62
3.5 Ghost-mediated domain wall interactions . . . 64
3.5.1 Two-body domain wall interactions . . . 64
3.5.2 Qualitative effects of interactions on the non-interacting wave function 69
3.5.3 Many-body domain wall interactions . . . 75
3.6 Conclusions . . . 81

4 A Spin-1 Kagomé Antiferromagnet 83
4.1 Introduction . . . 83
4.1.1 $\mathbf{S} = \mathbf{1}$ KHAF: experiment and theory . . . 84
4.1.2 AKLT models: Projective Hamiltonians . . . 85
4.2 The Model . . . 87
4.2.1 The Hamiltonian . . . 87
4.2.2 The ground states . . . 88
4.2.2.1 Schwinger boson representation . . . 89
4.2.2.2 Valence bond states basis . . . 90
4.2.2.3 Non-orthogonality: A calculation of the ground states' overlaps 92
4.3 Perturbing the Hamiltonian back to the nearest-neighbor Heisenberg form . . . 98
4.3.1 Perturbation theory calculations . . . 98
4.3.2 Effective Hamiltonian . . . 103
4.4 Analysis of effective Hamiltonian . . . 105
4.4.1 Discussion of the effective Hamiltonian's interactions . . . 105
4.4.2 Order by disorder . . . 107
4.4.3 Low-energy states . . . 108
4.4.3.1 Discussion of the ground state . . . 109
4.5 More features of the parent Hamiltonian . . . 113
4.6 Conclusions . . . 115

Bibliography 116

List of Figures

1.1 Classical frustration in the triangular and kagomé lattices: global and local degeneracy. . . . 4

2.1 Structure of the herbertsmithite compound, $ZnCu_3(OH)_6Cl_2$. . . . 14
2.2 Transition graph: Superposition of two dimer coverings on the square lattice. . 18
2.3 Assumed energy spectrum of the unperturbed Hamiltonian in the calculation of the magnetic susceptibility. . . . 20
2.4 There are two different cases for $H_{\mathrm{DM}}^{\langle ij\rangle}$ to operate on: the link $\langle ij\rangle$ (a) has a dimer; (b) is empty, but has dimers emerging from its sites. . . . 25
2.5 Possible overlaps of pairs of vectors in the set $\{\mathcal{P}H_{\mathrm{DM}}^{\langle ij\rangle}|d_\alpha\rangle\}_{\langle ij\rangle}$ with respect to a generic 2D lattice. . . . 30
2.6 The Shastry–Sutherland (SS) lattice and its topologically equivalent structure formed by the copper ions in $SrCu_2(BO_3)_2$. . . . 35
2.7 The checkerboard lattice: sign convention; the minimal loop (length 8) and the next minimal loop (length 12) in the overlap of two dimer coverings. . . . 40
2.8 Relations between the directions of the out-of-plane and in-plane components of the DM vectors for nearest-neighbor interactions in the kagomé lattice. . . . 46

3.1 In the degenerate ground states of the sawtooth chain, a spin-1 excitation decays into a kink and an antikink, spin-1/2 excitations (spinons). . . . 54
3.2 The diamondback ladder with coupling constant J. $S = 1/2$ spins occupy each site of the lattice. . . . 55
3.3 Perturbative separation of the upper and lower chains of the diamondback ladder. Lower chain obtained as renormalized Heisenberg chain with defects. . . . 57
3.4 Heisenberg chain plus one defect. Calculation of $\Delta\epsilon$. . . . 60
3.5 Plot of $\Delta\epsilon(K/J)$, the energy gained by the system when a ghost is produced in the lower chain of the ladder. . . . 62
3.6 Kink, antikinks and their ghosts: a calculation of the kink-antikink chemical potential. . . . 63
3.7 A plot of the kink-antikink chemical potential. Critical point indicates the proliferation of domain walls in the system. . . . 63
3.8 Heisenberg chain plus two defects: calculation of two-body domain wall interaction potential. . . . 65
3.9 Plots of $U(s)$, the two-body interaction potential. Power law fits. . . . 67
3.10 The "1D-box" problem: An antikink moving within the walls imposed by type-B kinks. . . . 69

3.11 Ground state energy and wave function of an antikink moving between two kinks; plotted for various interaction strengths. 71
3.12 Two interacting antikinks, each constrained in motion by their respective kinks. 73
3.13 Probability density function plots of the two-antikinks system: qualitative effects of interactions. 74
3.14 Multiple-defects chains. A look into many-body interactions. 75
3.15 E/N vs $1/L$ for different s and K/J. 79
3.16 The total, many-body, interaction potential as a function of K/J: (a) W/N_0 and (b) W/N_Δ. 79

4.1 2D layer of the organic compound m-MPYNN· X (X=BF_4, ClO_4), an effective spin-1 kagomé antiferromagnet. 85
4.2 Construction of the AKLT ground state in an $S = 1$ quantum chain. 86
4.3 Spin-1 kagomé AF: a valence bond ground state of the parent Hamiltonian. . . 88
4.4 Valence bond states: a proof of their linear independence. 91
4.5 Two loop cases of a single-hexagon mismatch in the overlap of two ground states. 96
4.6 Three-hexagons system size used to determine the matrix elements of the Heisenberg perturbation. 99
4.7 Pseudospin and corresponding valence bond states of the eight three-hexagons states used to compute $\langle\Psi|H^{ij}_{\text{Heis}}|\Psi\rangle$. 100
4.8 Hidden order: A non-zero S^z is always followed by a non-zero S^z of the opposite sign, independent of how many $S^z = 0$ occur in between. 100
4.9 a and b bosons can occupy a site. Valence bonds connect bosons of different type only. 101
4.10 Overall signs of the plaquette operators $\sigma^x_i\sigma^z_j\sigma^z_k$: proof that the K_3 terms vanish. 106
4.11 Competing order-by-disorder ground states of the triangular Ising model in a transverse field. 109
4.12 Previously proposed ground states of the spin-1 Heisenberg antiferromagnet. . 112
4.13 Magnetic and non-magnetic excitations of the parent Hamiltonian, Eq. (4.2). . . 114

List of Tables

2.1 Matrix elements results for the contributing cases 1, 5, 6, and 8 in Fig. 2.5(a). For the $S^h = \pm 1$ components, the results are the same, so they are given in the same column. The subscripts indicate the bonds involved in each case. 31

Chapter 1

Introduction

In this dissertation we present the results of a theoretical investigation of spin models on two-dimensional and quasi one-dimensional lattices, all unified under the concept of quantum frustrated antiferromagnetism. Although the systems we study here are of a quantum mechanical nature, they have an intrinsic connection to their classical relatives. By the time quantum frustrated magnetism came to being, its classical counterpart had already been around for several decades. The inception of the field can be attributed to Pauling's work on ice resulting in the six-vertex model [75]; however, the study of Ising spins on a triangular lattice by Wannier [93] in 1950 is considered the classical paradigm. The quantum aspect of the field gained real prominence after Anderson's association of these systems with superconductivity [7], and interest in quantum frustrated magnets flourished with his introduction of the resonating valence bond (RVB) state in 1973 [6]. As a new phase unlike any of the conventional ones, Anderson's proposal of the RVB state as a spin liquid really opened up a new chapter in condensed matter, namely, that of the search for exotic and novel phases of matter. Parting from Anderson's proposition, the belief has been that both quantum fluctuations and geometric frustration can destroy long-range magnetic order and in its place establish some type of disordered ground state with

unbroken symmetry. Our subjects of study possess these characteristics, making them interesting systems of investigation. As will be evident in all chapters, each individual study involves some aspect of the antiferromagnetic Heisenberg model on the kagomé lattice, which stands out as one of the most captivating systems in two dimensions due to the high degree of frustration in the system, as will be elaborated later. In the next paragraph we opt for a small synopsis of the studies we conducted, reserving the more detailed version for the introduction of each individual project. In the rest of the present chapter, we instead establish some of the concepts that appear throughout the dissertation in hopes of facilitating the reading of this document.

In Chapter 2 – a work that was jointly published with Kumar Raman and Kirill Shtengel [89] – we study the effect of Dzyaloshinskii–Moriya (DM) interactions on the zero-temperature magnetic susceptibility of systems whose low energy can be described by valence bond states. This work was inspired by the experimental reports on the compound $ZnCu_3(OH)_6Cl_2$, also known as herbertsmithite, which is said to be the first structurally perfect spin-1/2 kagomé antiferromagnet. Although this experimental system is our main motivation, our methods are more general and we apply them to the checkerboard and Shastry-Sutherland lattices as well. Chapter 3 discusses our findings in the study of ghost-mediated domain wall interactions in the diamond-back ladder. Antikinks and kinks are spin excitations acting as domain walls between degenerate ground states along one chain of the ladder. While as individual entities the antikink is energetically costly and the kink energetically free, our study finds that both interact via *ghosts* that they produce in the opposite chain of the ladder. Through the study of these ghosts, we find that domain walls proliferate in the system above a critical value of the system's coupling constants. It is this proliferation that makes their treatment as free, non-interacting particles impossible, so we study here their interactions both quantitatively and qualitatively, in a region where they are yet not very strong, namely below the critical point. In the last chapter, Chapter 4, we present a study of the spin-1 kagomé Heisenberg antiferromagnet. Starting with an SU(2)-symmetric

parent Hamiltonian with known ground states on the $S = 1$ kagomé lattice, we perturb the system with a Heisenberg term, thereby enhancing the Heisenberg interactions already present, and moving the system closer to a pure Heisenberg antiferromagnet. This allows us to analyze the possible valence bond state of this system.

1.1 Frustration

As recently stated, the systems examined here are generally known as quantum frustrated antiferromagnets. The purpose of this section is to describe a little bit more about the "frustrated" part of this term. The frustration in these systems comes from the geometry of the lattice as well as quantum fluctuations. To illustrate the first point, one can start with the simple example of Ising spins on a triangular lattice [93, 34]. Assuming the interactions to be antiferromagnetic, meaning that any pair of spins is satisfied if they point opposite to each other, from the point of view of a single plaquette one can clearly see that complete energy optimization is unattainable since there is always one unsatisfied bond, i.e., one frustrated bond. Having one such bond in each plaquette is the best the system can do. Since there are many ways these bonds can be arranged in the whole lattice, there is not a single ground state, but rather a degenerate ground state manifold. In contrast, the same situation on the square lattice does not produce any degeneracy (aside from the overall spin flip) as it is possible to have each of the spins oriented antiparallel to all its neighbors. The triangular lattice illustrates the case where the geometry is the impediment for energy optimization, i.e., the case of geometric frustration.

Another example of a lattice with geometric frustration is the kagomé , which exhibits an even higher degree of frustration than the triangular lattice [43]. This is true for any spin dimension/value and is attributed to the fact that (triangular) plaquettes are side-sharing in the triangular lattice, while in the kagomé they are corner-sharing. This different level of frustration

can be appreciated if one considers classical Heisenberg spins, as illustrated in Fig. 1.1. In this case where spins can point in any direction, a ground state in both lattices is achieved when the total spin in a plaquette is equal to zero. This means a planar arrangement of the spins at 120° with respect to each other. However, the similarities stop here: the degeneracy obtained in the triangular lattice is only with respect to global rotations, while the degeneracy in the kagomé is local. This means that, once a particular arrangement has been selected for one plaquette (shaded

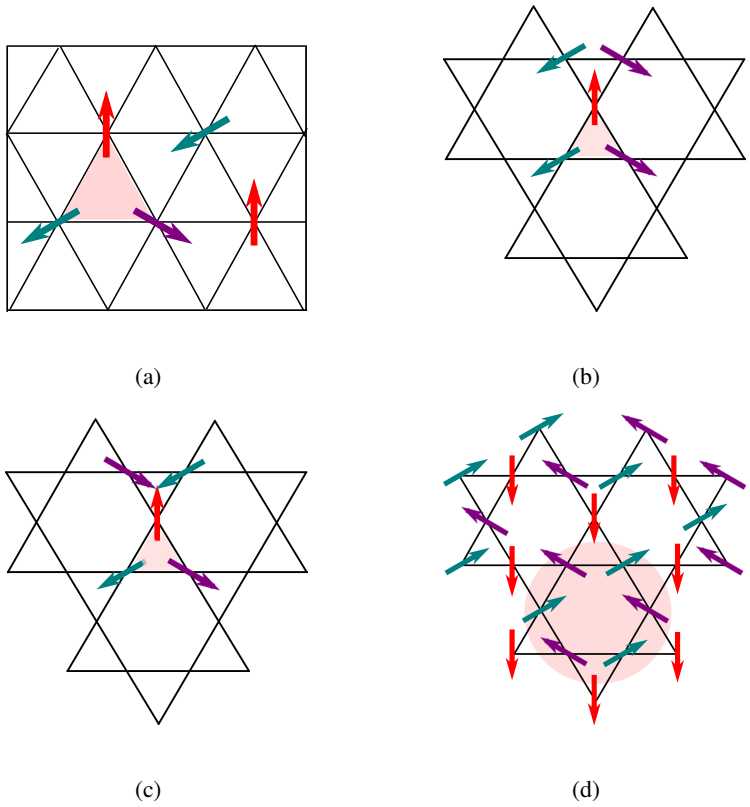


Figure 1.1: Ground state configurations of classical Heisenberg spins on the triangular (a) and kagomé (b, c, d) lattices illustrating the higher degree of frustration in the latter. An initial choice of spin arrangement (shaded triangle, 120° with respect to each other) yields a degeneracy (a) with respect to global rotations only in the triangular lattice; (b,c) that is local in the kagomé lattice. (d) An example of a zero-mode in the kagomé lattice. Spins in the shaded circle can be rotated at no energy cost.

triangle), the rest immediately follows in the triangular lattice (Fig. 1.1(a)). In contrast, initial selection in the kagomé still leaves some flexibility for the spin arrangement in the next and following plaquettes (Figs. 1.1(b) and 1.1(c)). This local degeneracy is so prevalent that *zero mode* configurations give rise, in which local spin rotations do not destroy the requirement of zero total spin per plaquette. An example of such a mode is illustrated in Fig. 1.1(d), where the spins within the shaded circle can be rotated with respect to the axis of the surrounding spins without imposing any energy penalty, that is, without leaving the ground state manifold.

The reason for this ground state degeneracy of (classical) frustrated magnets was given more formally by Moessner in Ref. [64]. Here, he defines the dimension of a ground state (D) as the difference between the degrees of freedom (F) and the ground-state constraints (K). For spins of n components, the constraint per unit of q spins is given by the n-component vector $\mathbf{L} = 0$, where $\mathbf{L}$ is the total spin of the unit; this is under the assumption of independent constraints, which might not always be possible to have. The point is that, once the constraints are not enough to define a ground state uniquely, the underconstraint is manifested as degrees of freedom in the ground state. The fewer spins two units share, the larger the number of degrees of freedom per unit is. Such case is exemplified by the kagomé lattice made up of corner-sharing triangles, where only one site is shared per unit. On the other hand, units in the triangular lattice share two sites and constraints are sufficient to define a non-degenerate ground state, up to global rotations.

Quantum fluctuations can also give rise to frustration. As classical Ising spins are changed to quantum Heisenberg spins, the previously "simple" ($H_{ij} = JS_i^z S_j^z$) interactions seeking the antiparallel alignment ($J > 0$) of individual pairs are now elevated to the interac-

tions of the type

$$\begin{aligned} H_{ij} = J\mathbf{S}_i \cdot \mathbf{S}_j &= J(S_i^x S_j^x + S_i^y S_j^y + S_i^z S_j^z) \\ &= \frac{J}{2}\left(S_i^+ S_j^- + S_i^- S_j^+\right) + JS_i^z S_j^z \end{aligned} \tag{1.1}$$

where the term in parenthesis, which flips spins (as it now wants to orient them along the plane), represents a competing interaction to the original Ising part. Competing interactions can destroy a previously existing order, such as the Néel order on the square lattice. This is due to the fact that the terms inside the parenthesis do not commute with the Ising piece. Thus, both geometric frustration and quantum fluctuations can enhance the disorder (a manifestation of frustration) in a system.

1.2 Unconventional phases

In the area of frustrated magnetism, the principal question is what happens to an antiferromagnet when the frustration that we mentioned earlier, in interplay with the system's small spin and coordination number, prevents the stabilization of conventional magnetic phases such as the Néel state. Classically, a system finds itself in a degenerate manifold of magnetic moment configurations commonly defined by some local requirement. The size of this manifold is exponential in the system's size [93]. In a quantum spin system, the system adopts an individual nonmagnetic state [6, 79, 95] whose order is unlike any of the conventional type. The systems that we will be discussing in this dissertation have the right features that make them favorable to exhibit nonconventional phases. Observing such novel phases is not out of the reach of theoretical modeling [82, 53, 61, 11, 54, 76], but having the experimental cues for their detection is still deficient and at the same time a subject of significant interest. The absence of a magnetic order at temperatures $T \ll J$ stands out as the simplest of indicators.

An alternative to forming a magnetic order in a frustrated system may be the formation of valence bond states. Essentially, a valence bond is a singlet pairing of spins. Distinct phases may emerge depending on the specifics. One particular phase is the valence bond crystal (VBC). In this state, near-neighbor spins arrange into some type of singlet configuration; a singlet can be between two spins, called a dimer, or, in general, between any $2n$ spins forming $2n$-mers $S = 0$ plaquettes [56]. In another phase, the short-range resonating valence bond (RVB) state, a singlet is formed between nearby spins too but, unlike the VBC, there is no specific order in the singlet formation. In both cases, there is no SU(2) symmetry breaking, the spin-spin correlations are exponentially decaying, provided the valence bonds are short-ranged, while the dimer-dimer (four-spin) correlations are long-ranged. With the exception of a quantum critical point, all excitations are gapped. To understand the origin of the gap, one imagines creating an excitation by breaking a singlet and elevating it into a triplet state. The energy cost for this is of order J. One fact specially relevant to us is the spin gap's manifestation in the magnetic susceptibility. At very low temperatures, the susceptibility vanishes exponentially as $\chi \sim e^{-\Delta/T}$, where Δ is the spin gap.

Another phase described by valence bonds is the long-range resonating valence bond (RVB) [6] spin liquid. As the name implies, valence bonds do not form a specified order. In this state, the singlets involve bonds of all lengths, the spin-spin correlations are algebraic, and the system has no gap to the excited states. As the valence bonds grow longer, it becomes energetically easier to break them, i.e., to separate its components. This is the reason for a gapless spectrum.

1.3 Superexchange

1.3.1 Heisenberg Hamiltonian

A recurring object of study in our different investigations is the antiferromagnetic (AF) Heisenberg Hamiltonian, $H_{ij} = J\mathbf{S}_i \cdot \mathbf{S}_j$, written here for spins at sites i and j ($J > 0$). Its frequent appearance is due to the fact that every system that we consider is described (or believed to be) by it. The Heisenberg Hamiltonian represents the exchange energy between electrons and allows a basic description of the magnetism in (Mott) insulators. The Hamiltonian is SU(2) invariant. Although a very well known fact, it seems relevant to remind the reader how this model turns out to be such a good representation. The systems that we treat consider the case of half-filling and are dominated by very large electron-electron interactions, so that each site of the lattice is occupied by a single electron. This Couloumb interaction is represented by a strong on-site repulsion, U. Conduction requires electrons moving through the lattice but, as observed, hopping to a different site already occupied is energetically costly. Under such unfavorable conditions, the system becomes an insulator. However, electrons can still gain some energy by virtually hopping to another site, i.e. by "virtual" delocalization. According to Anderson [5], this tendency results in an antiferromagnetic interaction, which he dubbed *superexchange*. This electron dynamics just described is encapsulated in the AF Heisenberg Hamiltonian, which is an effective model for Mott insulators of spin one half. Next, an outline of how this effective Hamiltonian is derived is given following Auerbach's book [9].

First, one starts by considering two orthogonal atomic wave functions, each occupied with a single electron. The zeroth-order Hamiltonian is given by the on-site interactions, $\mathcal{U} = U\sum_i n_{i\uparrow}n_{i\downarrow}$. The arrows denote the electron's spin orientation. The ground state for this term is a four-fold manifold characterized by states of single occupancy. To perturb the system, one takes into account the term that describes the tunneling between the states:

$\mathcal{T} = -t\sum_s \left(c_{1s}^\dagger c_{2s} + c_{2s}^\dagger c_{1s}\right)$, i.e., the hopping term. Here the sum is over spin, s, and $t/U \ll 1$. To first order in this perturbation, it is not possible for an electron to hop to the other atomic state since this would take it out of the ground state. However, second-order perturbation allows for virtual double occupancy, i.e. for superexchange. This delocalization lowers the kinetic energy of the electron. According to the Pauli principle, this gain in energy occurs only in the presence of an antiparallel neighboring spin, meaning that this is an antiferromagnetic effect. In effect, to this lowest (non-vanishing) allowed order of perturbation, the effective Hamiltonian that results is the Heisenberg with $J = 4t^2/U$. Since J is positive, one sees that the interaction is indeed antiferromagnetic.

1.3.2 Dzyaloshinskii-Moriya Interaction

The Heisenberg Hamiltonian derived above is not the only type of interaction occurring via a superexchange mechanism. Superexchange can also be defined as an indirect exchange interaction between two non-nearest-neighboring magnetic ions whose interaction is mediated by a non-magnetic ion placed in between [14], such as two copper ions and an oxygen ion, respectively. Yet another type of superexchange is the anisotropic exchange interaction known as the Dzyaloshinskii-Moriya interaction whose form is as given below,

$$H_{\mathrm{DM}}^{\langle ij\rangle} = \mathbf{D}_{ij} \cdot (\mathbf{S}_i \times \mathbf{S}_j), \tag{1.2}$$

and where $\mathbf{D}_{ij}$ is a vector that depends on the system. As the antisymmetric part of the most general bilinear spin-spin interaction, Eq. (1.2) was initially proposed in 1958 by Dzyaloshinskii [21] based on pure symmetry arguments. The microscopic explanation followed almost immediately. Contemporary to Dzyaloshinskii's suggestion was Anderson's theory of superexchange [5] which resulted in the isotropic superexchange interaction already discussed. In the presence of spin-orbit coupling, though, the theory had to be modified, as was done by Moriya in 1960

[65]. By extension of Anderson's theory, Moriya showed that the process of virtual transitions due to spin-orbit interaction [where the excited state is produced by the spin-orbit interaction in one of the magnetic ions] can cause an anisotropic exchange interaction, of the form of Eq. (1.2), which is a correction to the isotropic part. He also found the coupling constant D to be linear in the spin-orbit interaction. In addition, Moriya was able to show that this type of interaction is the dominant correction to the Heisenberg (isotropic) term when there is sufficiently low symmetry in the crystal. In fact, from a crystal symmetry point of view, there are certain rules that constrain the presence of the Dzyaloshinskii-Moriya interactions. As taken from Ref. [65], the rules for $\{\mathbf{D}_{ij}\}$ are the following. For two ions in the crystal located at points A and B, respectively, and C a point bisecting the segment AB,

1. When a center of inversion is located at C, $\mathbf{D} = 0$.
2. When a mirror plane perpendicular to AB passes through C, $\mathbf{D}$ lies in the mirror plane or $\mathbf{D} \perp AB$.
3. When there is a mirror plane including A and B, $\mathbf{D}$ is perpendicular to the mirror plane.
4. When a two-fold rotation axis perpendicular to AB passes through C, $\mathbf{D}$ is perpendicular to the two-fold axis.
5. When there is an n-fold axis $n \geq 2$ along AB, $\mathbf{D} \| AB$.

The implications of the aforementioned symmetry rules are several. For instance, according to rule 1, since the center of every bond in both the triangular and square lattices is a center of inversion, the DM interactions cannot be present. These can, however, occur in the kagomé lattice since every midpoint of a bond is not an inversion point. Rule 3 on the other hand implies that a perfect two-dimensional lattice, being itself a mirror plane, permits only the out-of-plane component D^z. These are some of the issues that we will pay attention to in Chapter 2, where DM interactions are considered. Another issue that will be taken into account is the antisymmetry

of (1.2), which requires adopting a convention for the orientation of the pair $\langle ij \rangle$. Whether it appears in the Hamiltonian as $\mathbf{S}_i \times \mathbf{S}_j$ or as $\mathbf{S}_j \times \mathbf{S}_i$ is something that needs to be decided. Our conventions for the systems in which the DM is added will be presented where appropriate. A final point we would like to make here about Eq. (1.2) is that it breaks the SU(2) symmetry and can be the source of departures from the pure Heisenberg behavior such as canting (preferred over the antiferromagnetic arrangement of spins) or small gaps.

Chapter 2

Dzyaloshinskii–Moriya Interactions in Valence Bond Systems

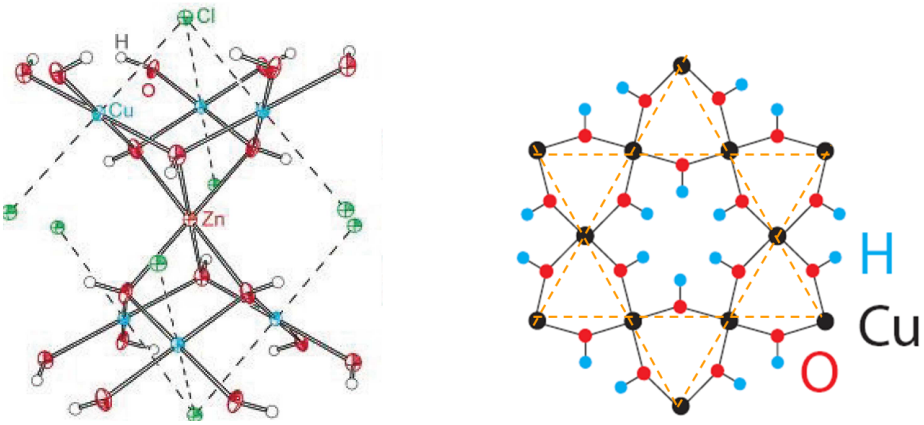
2.1 Introduction

In this chapter, we present our investigation of Dzyaloshinskii–Moriya (DM) interactions in valence bond systems. In particular, we study the effect of these interactions on the low–temperature magnetic susceptibility for a system whose low energy physics is dominated by short-ranged valence bonds, or singlets. Our approach is to introduce a nearest-neighbor DM interaction $H_{\rm DM}$ perturbatively into the unperturbed Hamiltonian, for which we have assumed three attributes: 1) it has a narrow band of low energy short-ranged valence bond states which are separated from the magnetic states by a spin gap; 2) its $S = 0$ band is connected to a narrow band of $S = 1$ magnetic states by $H_{\rm DM}$; 3) it conserves total spin. Under these assumptions, we obtain the new states of the system in the presence of DM, determine the resulting energy levels, and from these compute the powder magnetic susceptibility in the limit of $T \to 0$. How each of the mentioned premises is utilized should become clear in the context of the calculation. We

do this calculation analytically and generically for any valence-bond system. The general result obtained here is then subsequently applied to specific models that are expected to be in the class described above. The first in our list is the Shastry–Sutherland model of the spin-dimer compound $SrCu_2(BO_3)_2$, for which all the assumptions and approximations hold exactly. Second, we also specify our results for the case of the generalized Klein Hamiltonian on the checkerboard lattice [76, 70] (although there is no known physical realization of this lattice). The Klein Hamiltonian is known to have short-range valence bond ground states and a spectrum that approximately resembles that which we assume. The third and last model to which we apply our results, and really the motivation for this work, is the antiferromagnetic Heisenberg model of the $S = 1/2$ kagomé compound $ZnCu_3(OH)_6Cl_2$ synthesized a few years ago. Independent of the model considered, the main result is that a short-ranged valence bond phase, when perturbed with Dzyaloshinskii–Moriya interactions, will remain time-reversal symmetric in the absence of a magnetic field but the susceptibility will be nonzero in the $T \to 0$ limit. For $ZnCu_3(OH)_6Cl_2$ this means that our model is able to reconcile the experimental results - such as the lack of magnetic order and lack of any sign of a spin gap - with known theoretical facts about the kagomé Heisenberg antiferromagnet.

2.1.1 Motivation

Seeking the systems that would exhibit exotic phases such as a spin liquid had been, for the most part, a purely theoretical enterprise. Believed to exist in low-dimensional, low-spin and highly geometrically frustrated systems [77, 26], a significant portion of this search was directed to spin-$1/2$ antiferromagnets in the kagomé lattice, this due to the latter's higher degree of frustration (as indicated by the zero-point entropy of $0.50183k_{\mathrm{B}}$ [43] for an Ising AF, versus $0.32307k_{\mathrm{B}}$ in the triangular lattice[93]). The year 2005 finally saw the experimental re-



(a) (b)

Figure 2.1: (a) An illustration of the compound $ZnCu_3(OH)_6Cl_2$, also known as herbertsmithite [84]. (b) Separated by the Zn ions are these two-dimensional planes, where the magnetic copper ions of $S = 1/2$ form a kagomé structure [84, 37], indicated by the dashed lines.

alization of the mineral compound herbertsmithite, $ZnCu_3(OH)_6Cl_2$ [84], which is comprised of structurally perfect spin-$1/2$ kagomé layers of copper ions separated by nonmagnetic zinc ions. The $S = 1/2$ copper ions are the constituents responsible for the magnetic properties of the compound. Also found on the plane of each kagomé layer are the OH bonds that mediate the superexchange of Cu spins. A picture of herbersmithite is given in Fig. 2.1. Upon synthesis of this material, experimental measurements immediately followed, the powder magnetic susceptibility being one of those. When fitted to a Curie-Weiss law for high temperatures $T > 200$K [30], a Curie-Weiss temperature $\Theta \sim -300$K was found, translating into an antiferromagnetic exchange coupling $J \simeq 17$meV$\simeq 200$K. Consistent throughout a number of studies [30, 71, 51, 37] utilizing a variety of experimental methods was the lack of evidence for order: despite the low temperatures probed, as low as 50 mK, the system appeared to remain disordered, strongly indicating the presence of a nonmagnetic ground state.

Based on the experimental observations in $ZnCu_3(OH)_6Cl_2$, the spin-$1/2$ Heisenberg antiferromagnet on the kagomé lattice is the theoretical model that best seems to capture those experimental features. To begin, it is widely believed that the ground state of the $S = 1/2$ kagomé Heisenberg antiferromagnet (KHAF) is nonmagnetic, this in part due to the exact diagonalization results of Leung and Elser [46] which found the ground-state spin–spin correlation functions to be exponentially decaying with a correlation length of less than one lattice constant. According to an exact diagonalization study [92] also, a small spin gap $\Delta \sim J/20$ was determined. Below this gap lies a whole spectrum of singlet states growing exponentially with the system size and becoming gapless in the thermodynamic limit. These findings form the basis for the belief that the low energy physics of KHAF, and of herbertsmithite consequently, is governed by short-range valence bonds. As a matter of fact, a valence bond crystal (VBC) was proposed in references [50, 68, 86] as the ground state, although there are other studies [39, 85] that have suggested that the ground state is a spin liquid. (Reference [85] reported in 2010 the lowest energy found up to date for the system.) So far, this theory seems to describe herbertsmithite well except for one feature: the apparent absence of a spin gap, as indicated by magnetic susceptibility measurements. Previously, in the Introduction, it was mentioned that a reflection of a spin gap in a VBC is the exponentially vanishing susceptibility, $\chi \sim e^{-\Delta/T}$, at low temperatures . According to experiments, the behavior of χ when $T \to 0$ was anything but vanishing. In [30], χ continued to increase even at $T \ll \Delta$, whereas others indicated a saturation [71] or a probable decrease before saturation [73] to a nonzero value.

Several explanations for this discrepancy have been suggested. These range from stating that (i) the ground state of the KHAF could be a long-ranged valence bond spin liquid [78]; (ii) the absence of a gap is due to a disorder effect involving magnetic defects (Cu ions lying on the interplane sites) [12] and/or nonmagnetic impurities (Zn ions diluting the kagomé lattice)[12, 27] and (iii) that Dzyaloshinskii–Moriya interactions play an important role

[81, 80]. In this study we consider the last idea, so a mention of the work in References [81, 80] is pertinent. Here, Rigol and Singh [81, 80] are the first to suggest that Dzyaloshinskii-Moriya interactions should be considered as the reconciliatory mechanism between the spin gap present in the KHAF and its seeming absence in the susceptibility measurements. As they tried different perturbations of the pure Heisenberg Hamiltonian on the kagomé lattice, they found that adding DM interactions between nearest neighbors so that $D^p > |D^z|$, (D^p being the in-plane component), theory could explain the measured high-temperature susceptibility. The enhancement they found in the susceptibility under the above conditions derives from the ability of DM to mix the singlet states with the triplet states. In so doing, the $S = 1$ components contribute to obtain a non-vanishing low-T susceptibility. However, as they pointed out, the reliability of their numerical techniques is stronger for temperatures larger than $0.3J$ (higher than the spin-gap energy scale), so the work we present here is an attempt to provide the missing piece of information for very low temperatures. Although a priori the absence of a spin gap rules out a description in terms of a short-range valence bond state, in the following we show that it is possible to reconcile this apparent inconsistency if we add the Dzyaloshinskii-Moriya interactions.

2.2 Model and Formalism

In this section we set out to calculate, in the presence of a weak DM perturbation, the magnetic susceptibility for a system described by short-ranged valence bonds. Our calculation is general for any valence-bond system, but the valence bonds we consider here are between nearest neighbors only. Working with a basis of short-ranged valence bonds requires some care. Next we elaborate on the implications of this, mention some technicalities, and then proceed to calculate χ.

2.2.1 Dimer basis and overlap expansion

The arrangement of two nearest-neighbor spins coupled into a singlet is also known as a dimer. Having every spin in a lattice being part of a dimer gives rise to a lattice configuration $\{|d_\alpha\rangle\}$ known as a dimer covering. A pictorial representation of this is given in Fig. 2.2(a) for a square lattice. The wave functions which we will be using can be written as superpositions of these dimer coverings as

$$|\phi\rangle = \sum_\alpha a_\alpha |d_\alpha\rangle. \tag{2.1}$$

The care required in dealing with these wave functions is due to the fact that the dimer coverings are not orthogonal. One consequence is that the inner product of $|\phi\rangle$ with a state $|\psi\rangle = \sum_\alpha b_\alpha |d_\alpha\rangle$ is not simply $\sum_\alpha a_\alpha^* b_\alpha$ but

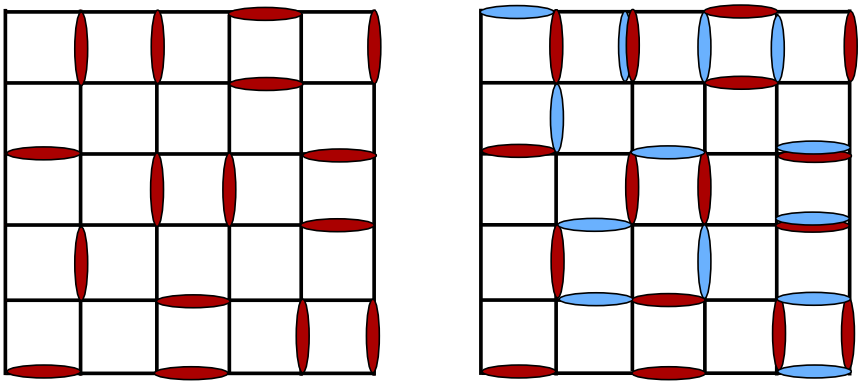
$$\langle\phi|\psi\rangle = 1 = \sum_{\alpha,\beta} a_\alpha^* b_\beta \Omega_{\alpha\beta} \tag{2.2}$$

where $\Omega_{\alpha\beta} \equiv \langle d_\alpha | d_\beta\rangle$ is the overlap matrix.

To calculate the overlap of two dimer coverings, one superposes them forming their *transition graph*, as shown in Fig. 2.2(b). As depicted there, the resulting picture contains double bonds (where the configurations coincide exactly) and loops of various even lengths. The magnitude of the corresponding overlap matrix element is:

$$|\Omega_{\alpha\beta}| = 2^{N_l} \prod_i x^{L_i} \tag{2.3}$$

where N_l is the number of loops in the transition graph; the product is over these loops, L_i being the length of the ith loop; and $x = 1/\sqrt{2}$. The actual signs of the overlap depend on the type of lattice involved. The expression given above, with no absolute value, is true for all bipartite lattices, while non-bipartite will contain some negative signs as well. Frequently, a transition graph will contain many long loops. As a result, the overlap between two arbitrary dimer coverings will often be small, although (for a finite system) never zero. On the other hand,



(a) (b)

Figure 2.2: (a) A general dimer covering of the square lattice. This represents a wave function, which we write as $|d_\alpha\rangle$, where a dimer across a link, shown as a red oval, means that the two spins are in a singlet bond. (b) Overlaying two different dimer coverings, shown by the red and blue ovals, gives the transition graph, which contains both double bonds – where the two coverings coincide –, and closed loops of various even lengths.

two valence-bond configurations could differ just by a single loop of minimal length, giving rise to the notion of a maximal overlap. Born from this latter concept is an approximation scheme known as the *overlap expansion* whose main idea is to treat x in Eq. (2.3) as a small parameter [82]. As an example, the overlap matrix of a set of dimer coverings on the square lattice, to leading order in this expansion, is

$$\Omega_{\alpha\beta}^{\text{square}} \approx \delta_{\alpha\beta} - 2x^4 \square_{\alpha\beta} + \dots \tag{2.4}$$

where $\square_{\alpha\beta}$ equals 0 unless the dimer coverings $|d_\alpha\rangle$ and $|d_\beta\rangle$ differ by exactly one minimal length loop, which on the square lattice has length four. In this case, $\square_{\alpha\beta} = \pm 1$, where the sign depends on the sign convention we take for the singlets (i. e. whether we take the singlet between spins i and j to be written as $\frac{1}{\sqrt{2}}(\uparrow_i\downarrow_j - \downarrow_i\uparrow_j)$ or $\frac{1}{\sqrt{2}}(\uparrow_j\downarrow_i - \downarrow_j\uparrow_i)$). It can be shown that for any lattice, we can choose the sign convention so that the overlap of two dimer coverings differing by exactly one minimal loop always comes with a negative sign [76]. For the square

lattice, this means that the entries of the matrix $\Box$ are always 0 or 1. We will assume this sign convention in this paper.

The overlap expansion can be applied to any operator $\mathcal{O}$. For example, on a square lattice,

$$\mathcal{O}_{\alpha\beta} \equiv \langle d_\alpha|\mathcal{O}|d_\beta\rangle \approx A_\alpha\delta_{\alpha\beta} - 2x^4 B_{\alpha\beta}\Box_{\alpha\beta} + \dots \tag{2.5}$$

where $A_\alpha = \mathcal{O}_{\alpha\alpha}$ and $B_{\alpha\beta}$ are constants. Eq. (2.5) is especially convenient when A_α and $B_{\alpha\beta}$ are independent of α, β.

Right at the foundation of our investigation are the valence bond, or dimer, states. Hence, implementation of the overlap expansion will be essential in our calculations. Although x is treated as a small parameter, in fact it is not so small, $1/\sqrt{2}$. This makes the approximation not a well controlled one. A better control is achieved in lattices where the minimal loop is large, and we expect the approximation to work fairly well at leading order in these cases. Such is the case of the kagomé lattice where the minimal loop has length six. Despite this concern, the expansion has proven to be a useful guiding principle in the construction of effective models of valence bond dominated phases [82, 24, 54, 55].

2.2.2 Perturbation theory for the magnetic susceptibility

In this section we derive the expression for the powder magnetic susceptibility utilizing perturbation theory. Prior to the actual derivation, we first discuss the assumptions we make about the unperturbed Hamiltonian, that is, in the absence of H_{DM}. The technicalities, and how we deal with them, of working with a non-orthogonal basis show up in this section. Formally, the DM perturbation we consider is

$$H_{\text{DM}} = \sum_{\langle ij\rangle} H_{\text{DM}}^{\langle ij\rangle} = \sum_{\langle ij\rangle} \mathbf{D}_{ij}\cdot(\mathbf{S}_i \times \mathbf{S}_j) \tag{2.6}$$

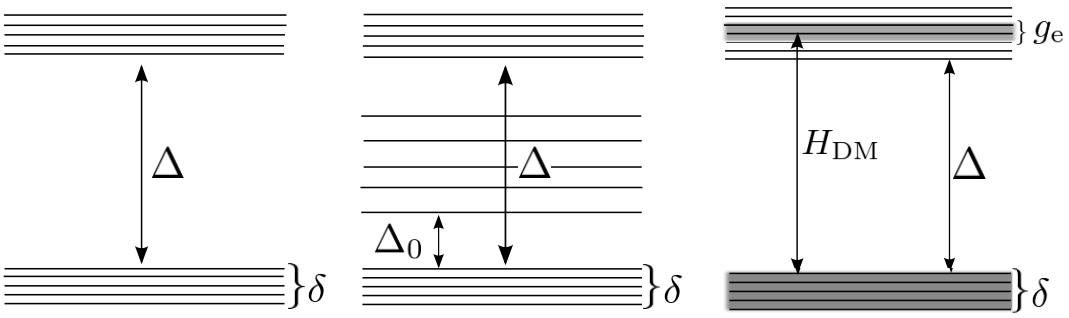


Figure 2.3: The generality of our first assumption allows us to consider different possibilities for the spectrum of the unperturbed Hamiltonian. (a) The low energy sector is comprised of a narrow band of states which are superpositions of dimer coverings, separated by a spin gap Δ from the excited states. (b) The same spectrum as in (a), but allowing a number of low-lying singlet states to exist in the gap. (c) Our second assumption: We assume $H_{\rm DM}$ connects the narrow band of low energy $S = 0$ states with a narrow band of higher energy $S = 1$ states.

where the sum is restricted to pairs of nearest-neighbor spins, where the contribution is the dominant, just as for the Heisenberg interaction.

2.2.2.1 Assumptions of the unperturbed Hamiltonian

The first thing we assume for the unperturbed Hamiltonian, from now on denoted as H_0, is that its spectrum has a low energy structure resembling Fig. 2.3(a). The figure depicts a set of low lying states $\{|n\rangle\}$, each of which can be written as a superposition of dimer coverings

$$|n\rangle = \sum_{\alpha} a_{n\alpha}|d_\alpha\rangle. \tag{2.7}$$

These states form a narrow band of width δ and are separated from magnetic excitations by a spin gap $\Delta \gg \delta$. While having a spin gap is crucial to the analysis, our formalism can be adapted to a situation where higher energy singlet states occur in the gapped region, as depicted in Fig. 2.3(b). A well-known class of toy models having (or widely believed to have) this structure are those of

the Klein–AKLT type [44, 1, 76, 70]. These are models for which dimer coverings, or a subset of them, are zero energy ground states and the collection of coverings $\{|d_\alpha\rangle\}$ forms a spin-gapped degenerate ground state manifold. In fact, we expect Fig. 2.3(a,b) to be a reasonably accurate caricature of a spin-gapped system even when there is no obvious reason for restricting our attention to nearest-neighbor valence bonds. We will discuss the suitability of this assumption (and the others) for the KHAF in section 2.5 but we refer the interested reader to the summary in section IIF of Ref. [55].

The second assumption is that $H_{\rm DM}$ connects the narrow band of low energy singlet states $\{|n\rangle\}$ with a band of $S = 1$ excited states $\{|e_\gamma\rangle\}$, whose bandwidth $\delta_{\rm e}$ is also small compared to Δ, as depicted in Fig. 2.3(c). While it is well-known that $H_{\rm DM}$ will mix the singlet and triplet sectors, we are assuming that the excited states $\{|e_\gamma\rangle\}$, for which the matrix elements $\langle d_\alpha|H_{\rm DM}|e_\gamma\rangle \neq 0$, are specifically $S = 1$ eigenstates. The simplest way to meet this requirement is via our third assumption: that the unperturbed Hamiltonian conserves total spin, which both the Klein and Heisenberg models do. We also assume these states form a narrow band. One way this condition may arise is if the magnetic excitations can be viewed as local disturbances of the low energy states. The simplest example of such a disturbance would be to break a single dimer by exciting the singlet to a triplet. Exactly how each of these assumptions is implemented will be made explicit during the derivation.

2.2.2.2 Derivation of the susceptibility χ

We mentioned before that the DM Hamiltonian (2.6) breaks SU(2) symmetry, so it does not commute with the total spin operator, $\mathbf{S} = \sum_i \mathbf{S}_i$, the sum being over sites in the lattice. This implies care when deriving an expression for the susceptibility. Consider the Hamiltonian

$$H = H_0 + H_{\rm DM} - g\mu_{\rm B}\mathbf{h}\cdot\mathbf{S} \tag{2.8}$$

where H_0 is the unperturbed Hamiltonian already discussed, $\mathbf{h}$ is the magnetic field, g the g-factor and $\mu_{\rm B}$ the Bohr magneton. If $\{E_\alpha, |\alpha\rangle\}$ are the eigenvalues and eigenstates of H, then the partition function is

$$Z[T, \mathbf{h}] = \sum_\alpha e^{-E_\alpha(\mathbf{h})/k_{\rm B}T} \tag{2.9}$$

where $k_{\rm B}$ is the Boltzmann constant and T the temperature. To compute the magnetization $\mathbf{M}$, we use the relation between the partition function Z and the free energy $F = -k_{\rm B}T \ln Z$. Thus, the μ component of $\mathbf{M}$ is calculated as

$$\begin{aligned} M^\mu &\equiv -\frac{\partial F}{\partial h_\mu} = -\frac{\partial}{\partial h_\mu}\left(-k_{\rm B}T \ln Z\right) = \frac{k_{\rm B}T}{Z}\frac{\partial Z}{\partial h_\mu} \\ &= -\frac{1}{Z}\sum_\alpha \frac{\partial E_\alpha}{\partial h_\mu} e^{-E_\alpha/k_{\rm B}T} \end{aligned} \tag{2.10}$$

and, from this, the susceptibility

$$\begin{aligned} \chi^{\mu\nu} &\equiv \frac{\partial M^\mu}{\partial h_\nu} = k_{\rm B}T\left(\frac{1}{Z}\frac{\partial^2 Z}{\partial h_\mu \partial h_\nu} - \frac{1}{Z^2}\frac{\partial Z}{\partial h_\mu}\frac{\partial Z}{\partial h_\nu}\right) \\ &= -\frac{1}{Z}\sum_\alpha \left(\frac{\partial^2 E_\alpha}{\partial h_\mu \partial h_\nu}\right) e^{-E_\alpha/k_{\rm B}T} \\ &+ \frac{1}{k_{\rm B}T}\left[\frac{1}{Z}\sum_\alpha \left(\frac{\partial E_\alpha}{\partial h_\mu}\frac{\partial E_\alpha}{\partial h_\nu}\right) e^{-E_\alpha/k_{\rm B}T}\right. \\ &- \left.\frac{1}{Z^2}\sum_\alpha \frac{\partial E_\alpha}{\partial h_\mu} e^{-E_\alpha/k_{\rm B}T} \sum_\beta \frac{\partial E_\beta}{\partial h_\nu} e^{-E_\beta/k_{\rm B}T}\right] \end{aligned} \tag{2.11}$$

Keeping in mind that our objective is to compare our results with experiment, we obtain an expression for the powder magnetic susceptibility, defined as $\chi_{\rm powder} = \frac{1}{3}(\chi^{xx} + \chi^{yy} + \chi^{zz})$. From our result above, adding all components,

$$\begin{aligned} \chi_{\rm powder} &= -\frac{1}{3Z}\sum_\alpha (\nabla^2_{\mathbf{h}} E_\alpha) e^{-E_\alpha/k_{\rm B}T} \\ &+ \frac{1}{3k_{\rm B}T}\Big[\frac{1}{Z}\sum_\alpha (\nabla_{\mathbf{h}} E_\alpha)^2 e^{-E_\alpha/k_{\rm B}T} \\ &- \frac{1}{Z^2}\Big(\sum_\alpha \nabla_{\mathbf{h}} E_\alpha e^{-E_\alpha/k_{\rm B}T}\Big)^2\Big] \end{aligned} \tag{2.12}$$

where $\nabla_{\mathbf{h}} \equiv (\frac{\partial}{\partial h_x}, \frac{\partial}{\partial h_y}, \frac{\partial}{\partial h_z})$ is the gradient operator.

A basic fact of quantum mechanics is that two commuting operators can have a common set of eigenfunctions. If $\mathbf{S}$ and H were two such operators, the states $\{|\alpha\rangle\}$ could be chosen as simultaneous eigenstates for the two and the eigenvalues would depend linearly on the magnetic field, i.e. $E_\alpha \sim \mathbf{h} \cdot \mathbf{S}_\alpha = \mathbf{h} \cdot \langle\alpha|\mathbf{S}|\alpha\rangle$. In this case, the second derivative term on the right-hand side of Eq. (2.11) would vanish and the remaining terms would give $T\chi^{\mu\nu} \sim [\langle S^\mu S^\nu\rangle - \langle S^\mu\rangle\langle S^\nu\rangle]$, which is a familiar version of the fluctuation-dissipation theorem. However, as already stated, H_{DM} does not commute with the total spin $\mathbf{S}$ and so H does not either. In this case, the field dependence of the eigenvalues is more complicated and one needs to exercise care.

Our first assumption was that the unperturbed Hamiltonian H_0 has a spectrum of the form shown in Fig. 2.3. Because we also assumed that H_0 commutes with $\mathbf{S}$ (assumption number three), the eigenstates of H_0 can be chosen to describe the system in the presence of a magnetic field (before any DM perturbation, that is). In addition, if $g\mu_{\text{B}}h$ is sufficiently small compared to Δ, the low energy spectrum of the Hamiltonian $H_1 = H_0 - g\mu_{\text{B}}\mathbf{h} \cdot \mathbf{S}$ will still resemble Fig. 2.3 and the lowest energy eigenstates will still be the collection of $S = 0$ states $\{|n\rangle\}$ of Eq. (2.7). However, the $S \neq 0$ bands will split into separate bands indexed by the spin component S^h along the field direction $\hat{\mathbf{h}}$. In particular, the triplet band $\{|e_\gamma\rangle\}$ mentioned earlier will split into three bands $\{|e_\gamma^{(S^h)}\rangle\}$, where $S^h = -1, 0, 1$. The spin gaps of the three bands are given by $\Delta^{(S^h)} = \Delta - g\mu_{\text{B}}hS^h$. From Eq. (2.13), one may verify that at low temperatures, the zero field susceptibility will vary as $\chi_{\text{powder}} \sim T^{-1}e^{-\Delta/T}$ which decreases to zero as $T \to 0$ as expected for a spin gapped system.

Thus far, we have included the magnetic field exactly into the system as it respects the low energy spectrum. Next, we see how this is all affected by the addition of a small DM interaction, Eq. (2.6). A not strictly necessary, but sufficient condition to have, is that $D = |\mathbf{D}|$

be small compared to the smallest of the spin gaps $\Delta^{(S^h)}$. Granted this, the spectrum of H will still resemble that of H_0, Fig. 2.3, having a set of low lying states separated by a gap (although no longer a *spin* gap since H does not conserve spin). Determining the low-temperature behavior of χ necessitates analyzing first how the low energy eigenvalues and eigenstates are modified as $H_{\rm DM}$ mixes these $S = 0$ states with $S \neq 0$ components.

To first order in perturbation theory, the states $\{|n\rangle\}$ become

$$|n'\rangle = |n\rangle + \sum_{k \neq n} \frac{\langle k|H_{\rm DM}|n\rangle}{E_n - E_k}|k\rangle \tag{2.13}$$

where the sum is over all eigenstates of $H_1 = H_0 - g\mu_{\rm B}\mathbf{h}\cdot\mathbf{S}$ except $|n\rangle$. The sum will get restricted by our assumption that $H_{\rm DM}$ connects the low energy sector $\{|n\rangle\}$ with a narrow band of $S = 1$ excited states $\{|e_\gamma\rangle\}$, split by the field into three separate narrow bands. Moreover, because the widths of these excited bands and of the low energy sector were assumed to be small compared to the gap, we may approximate the denominators by $E_k - E_n \approx \Delta^{(S^h)}$. In this case

$$\begin{aligned} |n'\rangle &= \sum_\alpha a_{n\alpha}\left(|d_\alpha\rangle - \sum_{S^h}\frac{1}{\Delta^{(S^h)}}\sum_\gamma \langle e_\gamma^{(S^h)}|H_{\rm DM}|d_\alpha\rangle|e_\gamma^{(S^h)}\rangle\right) \\ &\equiv \sum_\alpha a_{n\alpha}|d'_\alpha\rangle. \end{aligned} \tag{2.14}$$

One observes that, in augmenting H_1 with $H_{\rm DM}$ perturbatively, one has essentially placed all the effect onto the individual dimer states to create new ones

$$|d'_\alpha\rangle = |d_\alpha\rangle - \sum_{S^h}\frac{1}{\Delta^{(S^h)}}\sum_\gamma \langle e_\gamma^{(S^h)}|H_{\rm DM}|d_\alpha\rangle|e_\gamma^{(S^h)}\rangle. \tag{2.15}$$

Proceeding from this observation, our next job is to determine exactly how $H_{\rm DM}$ alters the dimer coverings. That is, to see what has changed from $|d_\alpha\rangle$ to $|d'_\alpha\rangle$. $H_{\rm DM}$ is a pairwise operator, acting on a link $\langle ij\rangle$ at a time. For this there are two cases to consider: either $\langle ij\rangle$ (a) is occupied by a dimer or (b) is an empty bond (see Fig. 2.4). It is appropriate now to introduce new notation.

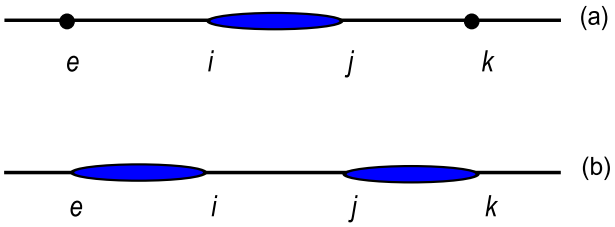


Figure 2.4: There are two different cases for $H_{\text{DM}}^{\langle ij\rangle}$ to operate on: the link $\langle ij\rangle$ (a) has a dimer; (b) is empty, but has dimers emerging from its sites.

The spin states between a pair i, j of spins are

$$(ij) \equiv \frac{1}{\sqrt{2}}\left(\uparrow_{i,n}\downarrow_{j,n} - \downarrow_{i,n}\uparrow_{j,n}\right) \tag{2.16a}$$

$$[ij]_0^n \equiv \frac{1}{\sqrt{2}}\left(\uparrow_{i,n}\downarrow_{j,n} + \downarrow_{i,n}\uparrow_{j,n}\right) \tag{2.16b}$$

$$[ij]_1^n \equiv \uparrow_{i,n}\uparrow_{j,n} \tag{2.16c}$$

$$[ij]_{-1}^n \equiv \downarrow_{i,n}\downarrow_{j,n} \tag{2.16d}$$

the singlet and the triplets, respectively, which are associated with the quantization axis $\hat{\mathbf{n}}$ where $\uparrow$ $(\downarrow)_{i,n}$ denotes the $S_i^n = \frac{1}{2}(-\frac{1}{2})$ eigenstate of the operator $\hat{S}_i^n$ and the subscripts $-1, 0, 1$ indicate the value of $S_i^n + S_j^n$ for the pair $\langle ij\rangle$. The notation for a singlet (ij) does not have a superscript because the singlet state is independent of the choice for $\hat{\mathbf{n}}$.

Determining the action of H_{DM} on the states (2.16) is more conveniently done with respect to the $\hat{\mathbf{z}}$ quantization axis. For this, we also write H_{DM} in terms of the raising ($S^+ = S^x + iS^y$) and lowering operators ($S^- = S^x - iS^y$), yielding

$$\begin{aligned} H_{\text{DM}} &= \sum_{\langle ij\rangle} H_{\text{DM}}^{\langle ij\rangle} = \sum_{\langle ij\rangle} \mathbf{D}_{ij}\cdot(\mathbf{S}_i \times \mathbf{S}_j) \\ &= \frac{D^x}{2i}\left(S_i^+S_j^z - S_i^-S_j^z - S_i^zS_j^+ + S_i^zS_j^-\right) + \frac{D^y}{2}\left(S_i^zS_j^+ + S_i^zS_j^- - S_i^+S_j^z - S_i^-S_j^z\right) \\ &\quad + \frac{D^z}{2i}\left(S_i^-S_j^+ - S_i^+S_j^-\right) \\ &= \frac{D^-}{2i}\left(S_i^+S_j^z - S_i^zS_j^+\right) - \frac{D^+}{2i}\left(S_i^-S_j^z - S_i^zS_j^-\right) + \frac{D^z}{2i}\left(S_i^-S_j^+ - S_i^+S_j^-\right) \end{aligned} \tag{2.17}$$

where we have defined $D^{\pm} \equiv D^x \pm iD^y$ and dropped the subscripts for a cleaner look. We now apply $H_{\text{DM}}^{\langle ij \rangle}$ to the case where i and j form a dimer, Fig. 2.4(a)

$$H_{\text{DM}}^{\langle ij \rangle}(ij) = \frac{D^z}{2i}[ij]_0^z - \frac{D^-}{2\sqrt{2}i}[ij]_1^z + \frac{D^+}{2\sqrt{2}i}[ij]_{-1}^z. \tag{2.18}$$

When $\langle ij \rangle$ is an empty bond, Fig. 2.4(b), the same application gives

$$\begin{aligned} H_{\text{DM}}^{\langle ij \rangle}((ei)(jk)) &= \frac{D^z}{4i}\left\{[ei]_1^z[jk]_{-1}^z - [ei]_{-1}^z[jk]_1^z\right\} \\ &- \frac{D^-}{4\sqrt{2}i}\left\{[ei]_1^z[jk]_0^z - [ei]_0^z[jk]_1^z\right\} \\ &- \frac{D^+}{4\sqrt{2}i}\left\{[ei]_{-1}^z[jk]_0^z - [ei]_0^z[jk]_{-1}^z\right\} \qquad (2.19) \\ &= -\frac{D^z}{4i}\left\{[ek]_0^z(ij) + (ek)[ij]_0^z\right\} \\ &+ \frac{D^-}{4\sqrt{2}i}\left\{[ek]_1^z(ij) + (ek)[ij]_1^z\right\} \\ &- \frac{D^+}{4\sqrt{2}i}\left\{[ek]_{-1}^z(ij) + (ek)[ij]_{-1}^z\right\}. \qquad (2.20) \end{aligned}$$

As observed in Eq. (2.18) and Eq. (2.19), the effect of $H_{\text{DM}}^{\langle ij \rangle}$ on a dimer covering is to convert any singlet emerging from the sites i and j involved into a triplet state. When written in the manner of Eq. (2.20), this and Eq. (2.18) make clear the fact that the state $H_{\text{DM}}|d_\alpha\rangle$ is a state of total spin with $S = 1$. Now, determining the new energies to first order of perturbation theory entails calculating terms like $\langle n|H_{\text{DM}}|n\rangle$, which are in turn sums of matrix elements of the type $\langle d_\alpha|H_{\text{DM}}|d_\beta\rangle$. For the reason recently stated, the latter evaluates to zero. Therefore, the energies of the states $|n\rangle$ are not modified to this order of perturbation.

Going to second order, the correction is given by

$$
\begin{aligned}
E_n^{(2)} &= \sum_{k\neq n} \frac{|\langle k|H_{\rm DM}|n\rangle|^2}{E_n - E_k} \\
&\approx -\sum_{S^h} \frac{1}{\Delta^{(S^h)}} \sum_{\alpha,\beta,\gamma} a^*_{n\alpha} a_{n\beta} \langle d_\alpha|H_{\rm DM}|e^{(S^h)}_\gamma\rangle\langle e^{(S^h)}_\gamma|H_{\rm DM}|d_\beta\rangle \qquad (2.21) \\
&= -\frac{1}{\Delta - g\mu_{\rm B}h} \sum_{\alpha,\beta,\gamma} a^*_{n\alpha} a_{n\beta} \langle d_\alpha|H_{\rm DM}|e^{(1)}_\gamma\rangle\langle e^{(1)}_\gamma|H_{\rm DM}|d_\beta\rangle \\
&\quad - \frac{1}{\Delta} \sum_{\alpha,\beta,\gamma} a^*_{n\alpha} a_{n\beta} \langle d_\alpha|H_{\rm DM}|e^{(0)}_\gamma\rangle\langle e^{(0)}_\gamma|H_{\rm DM}|d_\beta\rangle \\
&\quad - \frac{1}{\Delta + g\mu_{\rm B}h} \sum_{\alpha,\beta,\gamma} a^*_{n\alpha} a_{n\beta} \langle d_\alpha|H_{\rm DM}|e^{(1)}_\gamma\rangle\langle e^{(1)}_\gamma|H_{\rm DM}|d_\beta\rangle, \qquad (2.22)
\end{aligned}
$$

where the operators $\mathcal{P}^{(S^h)} \equiv \sum_\gamma |e^{(S^h)}\rangle\langle e^{(S^h)}|$ are projection operators that respectively select for the $S^h = 1$, 0, and -1 components of $H_{\rm DM}|d_\beta\rangle$. Therefore, it is very convenient to rewrite Eqs. (2.18)–(2.20) with respect to the two-spin states of the $\hat{\mathbf{h}}$ quantization axis, in other words, to generalize these states from the $\hat{\mathbf{z}}$ axis to the arbitrary field direction $\hat{\mathbf{h}} = \sin\theta\cos\phi\hat{\mathbf{x}} + \sin\theta\sin\phi\hat{\mathbf{y}} + \cos\theta\hat{\mathbf{z}}$. This is done by using the relations

$$|\hat{\mathbf{h}}+\rangle = \exp^{-i\phi/2}\cos\left(\frac{\theta}{2}\right)|S^z+\rangle + \exp^{i\phi/2}\sin\left(\frac{\theta}{2}\right)|S^z-\rangle \qquad (2.23a)$$

$$|\hat{\mathbf{h}}-\rangle = -\exp^{-i\phi/2}\sin\left(\frac{\theta}{2}\right)|S^z+\rangle + \exp^{i\phi/2}\cos\left(\frac{\theta}{2}\right)|S^z-\rangle \qquad (2.23b)$$

where $|S^z+\rangle$ corresponds to spin up ($\uparrow$) and $|S^z+\rangle$ to spin down ($\downarrow$). Equations (2.23) can be solved for $|S^z\pm\rangle$, which are substituted into Eqs. (2.18)–(2.20). The rest is all algebra. Eq. (2.18) is given by the new expression

$$H^{\langle ij\rangle}_{\rm DM}(ij) = \frac{D^h}{2i}[ij]^h_0 - \frac{D^{\perp -}}{2i\sqrt{2}}[ij]^h_1 + \frac{D^{\perp +}}{2i\sqrt{2}}[ij]^h_{-1} \qquad (2.24)$$

while Eqs. (2.19) and (2.20) become

$$\begin{aligned} H_{\rm DM}^{\langle ij\rangle}((ei)(jk)) &= \frac{D^h}{4i}\left\{[ei]^h_1[jk]^h_{-1} - [ei]^h_{-1}[jk]^h_1\right\} \\ &\quad - \frac{D^{\perp -}}{4i\sqrt{2}}\left\{[ei]^h_1[jk]^h_0 - [ei]^h_0[jk]^h_1\right\} \\ &\quad - \frac{D^{\perp +}}{4i\sqrt{2}}\left\{[ei]^h_{-1}[jk]^h_0 - [ei]^h_0[jk]^h_{-1}\right\} \qquad (2.25) \\ &= -\frac{D^h}{4i}\left\{[ek]^h_0(ij) + (ek)[ij]^h_0\right\} \\ &\quad + \frac{D^{\perp -}}{4i\sqrt{2}}\left\{[ek]^h_1(ij) + (ek)[ij]^h_1\right\} \\ &\quad - \frac{D^{\perp +}}{4i\sqrt{2}}\left\{[ek]^h_{-1}(ij) + (ek)[ij]^h_{-1}\right\}. \qquad (2.26) \end{aligned}$$

Above, we have introduced the notation,

$$D^h = \mathbf{D}\cdot\hat{\mathbf{h}} = D^x\sin\theta\cos\phi + D^y\sin\theta\sin\phi + D^z\cos\theta \qquad (2.27)$$

and

$$D^{\perp\pm} = -D^z\sin\theta + D^x(\cos\theta\cos\phi \mp i\sin\phi) \pm iD^y(\cos\phi \mp i\cos\theta\sin\phi). \qquad (2.28)$$

D^h is the projection of $\mathbf{D}$ along $\hat{\mathbf{h}}$ and $D^{\perp\pm}$ are the components along the perpendicular direction. The $\pm$ indicate that the latter are complex conjugates of each other. Perhaps it is useful to remind the reader that the S^h component in Eqs. (2.24)–(2.26) is determined by adding the subscripts, explicit and implicit, in each term. Thus, one observes that the magnitude of the $S^h = 0$ component depends on D^h and the $S^h = \pm 1$ on the $D^{\perp\mp}$. This is true for $\{\langle ij\rangle\}$. Going back to our calculation of the energy corrections, (2.21), we are essentially inserting the operator $H_{\rm DM}\mathcal{P}^{(S^h)}H_{\rm DM}$ between two dimer coverings, an action that actually occurs involving only two links at a time as $\langle d_\alpha|H_{\rm DM}^{\langle ab\rangle}\mathcal{P}^{(S^h)}H_{\rm DM}^{\langle cd\rangle}|d_\beta\rangle$. To calculate these matrix elements, we do two things first. One, we use the property of projection operators to write $\mathcal{P}^{(S^h)} = \mathcal{P}^{(S^h)}\mathcal{P}^{(S^h)}$. Two, we apply the overlap expansion approximation discussed in section 2.2.1 which involves

keeping only the diagonal term. When this is done, Eq. (2.22) becomes

$$E_n^{(2)} \approx -\sum_\alpha |a_{n\alpha}|^2 \Bigg\{ \frac{1}{\Delta - g\mu_{\rm B} h} \sum_{\langle ab\rangle\langle cd\rangle} \langle d_\alpha | H_{\rm DM}^{\langle ab\rangle} | \mathcal{P}^{(S^h=1)} \mathcal{P}^{(S^h=1)} | H_{\rm DM}^{\langle cd\rangle} | d_\alpha \rangle$$
$$+ \frac{1}{\Delta} \sum_{\langle ab\rangle\langle cd\rangle} \langle d_\alpha | H_{\rm DM}^{\langle ab\rangle} | \mathcal{P}^{(S^h=0)} \mathcal{P}^{(S^h=0)} | H_{\rm DM}^{\langle cd\rangle} | d_\alpha \rangle$$
$$+ \frac{1}{\Delta + g\mu_{\rm B} h} \sum_{\langle ab\rangle\langle cd\rangle} \langle d_\alpha | H_{\rm DM}^{\langle ab\rangle} | \mathcal{P}^{(S^h=-1)} \mathcal{P}^{(S^h=-1)} | H_{\rm DM}^{\langle cd\rangle} | d_\alpha \rangle \Bigg\} + O(x^{L_{\rm min}}). \quad (2.29)$$

The approximation we have made by keeping only the diagonal terms can be accurate if the overlaps of the dimer coverings $|d_\alpha\rangle$ and $|d_\beta\rangle$ are small or if the loops that occur in the transition graph have a large minimal length, $L_{\rm min}$. To the same order of approximation, $\sum_\alpha |a_{n\alpha}|^2 \approx 1 + O(x^{L_{\rm min}})$. A priori, we note that whether the matrix elements in (2.29) vanish or not will depend on the particular links $\langle ab\rangle$ and $\langle cd\rangle$ involved. And, as was already noted, projecting out the $S^h = 0$ component involves the $\{D_{ij}^h\}$, so the corresponding terms in (2.29) will be proportional to

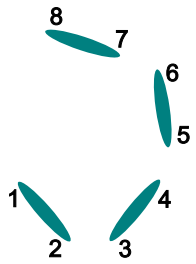
$$D_{ab}^h D_{cd}^h = (\mathbf{D}_{ab} \cdot \hat{\mathbf{h}})(\mathbf{D}_{cd} \cdot \hat{\mathbf{h}}), \quad (2.30)$$

while the $S^h = \pm 1$ projections will relate to a proportionality constant of the form given below. This is true even when no expansion approximation is made.

$$D_{ab}^{\perp -} D_{cd}^{\perp +} + D_{ab}^{\perp +} D_{cd}^{\perp -} = 2[\mathbf{D}_{ab} \cdot \mathbf{D}_{cd} - (\mathbf{D}_{ab} \cdot \hat{\mathbf{h}})(\mathbf{D}_{cd} \cdot \hat{\mathbf{h}})]. \quad (2.31)$$

For a dimer covering $|d_\alpha\rangle$, the set of vectors $\{\mathcal{P}^{(S^h)} H_{\rm DM}^{\langle ij\rangle} |d_\alpha\rangle\}_{\langle ij\rangle}$ can be determined by looking at Eqs. (2.24)–(2.26). Eq. (2.29) involves the sum of all possible overlaps between pairs of vectors in this set. These pairs can be classified into ten distinct types of combinations which are listed in Fig. 2.5(b) with reference to a dimer covering of the generic lattice depicted in Fig. 2.5(a). The terms that actually arise will depend on the connectivity of the lattice under consideration.

The dimer covering obtained from $\mathcal{P}^{(S^h)} H_{\rm DM}^{\langle ab\rangle} |d_\alpha\rangle$ is very similar to that of $|d_\alpha\rangle$ except for the dimers originating from the sites a and b, which have been raised to triplets.



(a)

1.	$H^{12}_{\rm DM}\mathcal{P}^{(S^h)}H^{12}_{\rm DM}$	6.	$H^{24}_{\rm DM}\mathcal{P}^{(S^h)}H^{23}_{\rm DM}$
2.	$H^{34}_{\rm DM}\mathcal{P}^{(S^h)}H^{12}_{\rm DM}$	7.	$H^{25}_{\rm DM}\mathcal{P}^{(S^h)}H^{23}_{\rm DM}$
3.	$H^{23}_{\rm DM}\mathcal{P}^{(S^h)}H^{12}_{\rm DM}$	8.	$H^{14}_{\rm DM}\mathcal{P}^{(S^h)}H^{23}_{\rm DM}$
4.	$H^{45}_{\rm DM}\mathcal{P}^{(S^h)}H^{12}_{\rm DM}$	9.	$H^{15}_{\rm DM}\mathcal{P}^{(S^h)}H^{23}_{\rm DM}$
5.	$H^{23}_{\rm DM}\mathcal{P}^{(S^h)}H^{23}_{\rm DM}$	10.	$H^{67}_{\rm DM}\mathcal{P}^{(S^h)}H^{23}_{\rm DM}$

(b)

Figure 2.5: (a) A 2D generic lattice. Filled ovals denote dimers. (b) Calculating the second order (in DM) correction to the energy, $E_n^{(2)}$, involves computing all possible overlaps of pairs of vectors in the set $\{\mathcal{P}H^{\langle ij\rangle}_{\rm DM}|d_\alpha\rangle\}_{\langle ij\rangle}$ for each dimer covering in the superposition that defines the unperturbed state $|n\rangle$ (Eq. (2.7)). There are ten distinct cases to consider, indexed in this table by the link operators involved, in reference to the generic dimer covering in (a). The possibilities are both links involving dimers, (1)–(2); one link involving a dimer, (3)–(4); and neither link involving a dimer (5)–(10). If both links involve a dimer, they can be either (1) the same or (2) different dimers. If one link involves a dimer, then the other link is an empty bond that either (3) contains or (4) does not contain one of the spins of that dimer. If neither link involves a dimer, then the possibilities are (5) the two empty links are the same; the two links share exactly one spin while the other two spins either (6) form a dimer – this is possible if the lattice has triangular plaquettes or (7) do not form a dimer; or the two links do not share a spin (8)–(10). In this latter case, the two empty links may be connected by (8) two dimers – this is possible if the lattice has square plaquettes; (9) exactly one dimer; or (10) no dimers.

This means that, unless $\langle ab\rangle$ and $\langle cd\rangle$ involve the same dimers being modified, the matrix elements $\langle d_\alpha|H^{\langle cd\rangle}_{\rm DM}\mathcal{P}^{(S^h)}\mathcal{P}^{(S^h)}H^{\langle ab\rangle}_{\rm DM}|d_\alpha\rangle = 0$. From the cases listed in Fig. 2.5(b), only numbers 1, 5, 6 and 8 satisfy this requirement. The remaining cases don't contribute in the diagonal elements, but do so at higher orders in the overlap expansion involving off-diagonal matrix elements. We write the state of the dimer covering of the generic lattice (Fig. 2.5(a)) as $|d\rangle = (12)(34)(56)(78)$, where, according to the notation introduced before, (ij) denotes a sin-

$\langle d_\alpha \vert H_{\rm DM}^{\langle cd\rangle}\mathcal{P}^{(S^h)}\mathcal{P}^{(S^h)}H_{\rm DM}^{\langle ab\rangle}\vert d_\alpha\rangle$			
Case	$S^h=\pm 1$	$S^h=0$	Type
1	$(1/8)(\mathbf{D}_{ab}\cdot\mathbf{D}_{ab}-D^h_{ab}D^h_{ab})$	$(1/4)D^h_{ab}D^h_{ab}$	Dimer
5	$(1/16)(\mathbf{D}_{ab}\cdot\mathbf{D}_{ab}-D^h_{ab}D^h_{ab})$	$(1/8)D^h_{ab}D^h_{ab}$	Empty
6	$(-1/16)(\mathbf{D}_{ab}\cdot\mathbf{D}_{ac}-D^h_{ab}D^h_{ac})$	$(-1/8)D^h_{ab}D^h_{ac}$	Triangular
8	$(1/16)(\mathbf{D}_{ad}\cdot\mathbf{D}_{bc}-D^h_{ad}D^h_{bc})$	$(1/8)D^h_{ad}D^h_{bc}$	Square

Table 2.1: Matrix elements results for the contributing cases 1, 5, 6, and 8 in Fig. 2.5(a). For the $S^h=\pm1$ components, the results are the same, so they are given in the same column. The subscripts indicate the bonds involved in each case.

glet. Utilizing the results given in Eqs. (2.24) and (2.26), we calculate all the matrix elements for each of the cases mentioned above. In the process, one needs to ensure that the vectors $\{\mathbf{D}_{ij}\}$ are put back the subscripts since they are link-dependent. In Table 2.1 we present the results for the matrix elements of the contributing cases, indicating the type of plaquette formed by the links involved.

To finally determine the second-order energy corrections, $E_n^{(2)}$, we must add all the contributions given in Table (2.1), yielding

$$\begin{aligned}E_n^{(2)} = -\sum_\alpha |a_{n\alpha}|^2\Bigg\{&\sum_{\text{Empty}}\frac{1}{8\Delta}\big(D^2_{ab}+[D^2_{ab}-{D^h_{ab}}^2]\frac{h^2}{\gamma^2-h^2}\big)\\ &+\sum_{\text{Dimers}}\frac{1}{4\Delta}\big(D^2_{ab}+[D^2_{ab}-{D^h_{ab}}^2]\frac{h^2}{\gamma^2-h^2}\big)\\ &-\sum_{\text{Triangular}}\frac{2}{8\Delta}\big(\mathbf{D}_{ab}\cdot\mathbf{D}_{ac}+[\mathbf{D}_{ab}\cdot\mathbf{D}_{ac}-D^h_{ab}D^h_{ac}]\frac{h^2}{\gamma^2-h^2}\big)\\ &+\sum_{\text{Square}}\frac{2}{8\Delta}\big(\mathbf{D}_{ad}\cdot\mathbf{D}_{bc}+[\mathbf{D}_{ad}\cdot\mathbf{D}_{bc}-D^h_{ad}D^h_{bc}]\frac{h^2}{\gamma^2-h^2}\big)\Bigg\}.\end{aligned}\tag{2.32}$$

With the definition $\gamma\equiv\left(\frac{\Delta}{g\mu_{\rm B}}\right)^2$, one observes that all the field dependence of (2.32) is in the factor $\frac{h^2}{\gamma^2-h^2}$. As already indicated in Table (2.1) and is repeated here, each term of $E_n^{(2)}$ corresponds to a different configuration of the links involved. In a moment, we will explicitly state what each represents, but first we want to point out the factor of 2 in the *Triangular* and

Square sums, which comes from the double contribution in the sum of (2.29). The first term, *Empty*, consisting of a sum over links not occupied by a singlet, can be equivalently written as $\sum_{\text{Empty}}(\ldots) = \sum_{\text{All links}}(\ldots) - \sum_{\text{Dimers}}(\ldots)$. We replace this in (2.32) and combine like terms. In the sum over *All links* remaining, since there is no more dependence on any particular dimer covering, we can replace $\sum_\alpha |a_{n\alpha}|^2$ by 1. With these changes in place, Eq. (2.32) can be written more succinctly as

$$\begin{aligned} E_n^{(2)} = &-\frac{1}{8\Delta}\sum\nolimits_{\langle ab\rangle}^{(0)} \left(D_{ab}^2 + \eta\left[D_{ab}^2 - (\mathbf{D}_{ab}\cdot\hat{\mathbf{h}})^2\right]\right) \\ &- \frac{1}{8\Delta}\sum_\alpha |a_{n\alpha}|^2 \Bigg\{ \sum\nolimits_{(ab)\in|d_\alpha\rangle}^{(1)} \left(D_{ab}^2 + \eta\left[D_{ab}^2 - (\mathbf{D}_{ab}\cdot\hat{\mathbf{h}})^2\right]\right) \\ &- 2\sum\nolimits_{\triangle[a(bc)]\in|d_\alpha\rangle}^{(2)} \left(\mathbf{D}_{ab}\cdot\mathbf{D}_{ac} + \eta\left[\mathbf{D}_{ab}\cdot\mathbf{D}_{ac} - (\mathbf{D}_{ab}\cdot\hat{\mathbf{h}})(\mathbf{D}_{ac}\cdot\hat{\mathbf{h}})\right]\right) \\ &+ 2\sum\nolimits_{\square[(ab)(cd)]\in|d_\alpha\rangle}^{(3)} \left(\mathbf{D}_{ad}\cdot\mathbf{D}_{bc} + \eta\left[\mathbf{D}_{ad}\cdot\mathbf{D}_{bc} - (\mathbf{D}_{ad}\cdot\hat{\mathbf{h}})(\mathbf{D}_{bc}\cdot\hat{\mathbf{h}})\right]\right) \Bigg\} + O(x^{L_{\min}}) \end{aligned} \tag{2.33}$$

where we defined the new variable $\eta = \frac{h^2}{\gamma^2 - h^2}$. Labeled with superscript (0), this sum is over all the links of the lattice and is completely independent of dimer covering. All the states in the low-energy sector get this correction. The next terms, sums (1), (2) and (3), do depend on the particular dimer covering $|d_\alpha\rangle$ entering Eq. (2.7). For the contributing states, sum (1) is over all the links $\langle ab\rangle$ occupied by a dimer; sum (2) is over all triangular plaquettes with vertices a, b and c, where $\langle bc\rangle$ contains a dimer; and sum (3) is over all square plaquettes $\{a, b, c, d\}$ with dimers (ab) and (cd). We finalize the description of Eq. (2.33) by stating that sums (2) and (3) will only contribute if the lattice has triangular or square plaquettes.

Eq. (2.33) hence gives the magnetic-field-dependence of the energies for the states in the low energy manifold. Now, let us refocus on our main objective of determining the low temperature behavior of the magnetic susceptibility. If we restrict T and h to be small compared to the gap Δ, we expect that the thermal averages of Eq. (2.11) will get the main contribution

from the low lying states due to the Boltzmann factors. Hence, if we make the approximation of restricting the sums to the low energy manifold, the leading h-dependence is quadratic. This immediately means that the zero field susceptibility will be determined by the second derivative terms of Eq. 2.11 which, as mentioned above, vanish for systems where total spin is conserved.

Taking the necessary derivatives, we obtain the following for the powder magnetic susceptibility in the limit of $T \to 0$

$$\chi_{\text{powder}} = \frac{(g\mu_B)^2}{6\Delta^3}\Bigg\{\sum\nolimits_{\langle ab\rangle}^{(0)} D_{ab}^2 + \frac{1}{Z}\sum\nolimits_n{}' w_n \sum_\alpha |a_{n\alpha}|^2 \Big(\sum\nolimits_{(ab)\in|d_\alpha\rangle}^{(1)} D_{ab}^2 - 2\sum\nolimits_{\triangle[a(bc)]\in|d_\alpha\rangle}^{(2)} \mathbf{D}_{ab}\cdot\mathbf{D}_{ac} + 2\sum\nolimits_{\square[(ab)(cd)]\in|d_\alpha\rangle}^{(3)} \mathbf{D}_{ad}\cdot\mathbf{D}_{bc}\Big)\Bigg\}, \tag{2.34}$$

where $w_n = e^{-E_n/k_BT}$ is the Boltzmann factor of state $|n\rangle$ and the primed sum is restricted to the low energy manifold. The expression can be simplified if we assume the magnitude of $\mathbf{D}$ to be the same on every link and the products $\mathbf{D}_{ab}\cdot\mathbf{D}_{ac} = D^2\cos\theta_\triangle$ and $\mathbf{D}_{ad}\cdot\mathbf{D}_{bc} = D^2\cos\theta_\square$ are the same for every triangular and square plaquette respectively. In this case, Eq. 2.34 becomes

$$\chi_{\text{powder}} = \frac{N(g\mu_B)^2D^2}{6\Delta^3}\left(\frac{z+1}{2} - 2\cos\theta_\triangle\frac{\langle N_\triangle\rangle}{N} + 2\cos\theta_\square\frac{\langle N_\square\rangle}{N}\right). \tag{2.35}$$

This needs further explanation. With the assumptions made above, the D's can come out of the sums. Next, the sum with superscript (0) counts all the links on the lattice. This is given by $zN/2$, where z is the coordination number and N is the total number of spins. In the sum with superscript (1), we are basically calculating the average number of dimers on the lattice. As each dimer is between two spins, this number is given by $N/2$. Similarly, for sums with superscripts (2) and (3), we have defined $\langle N_{\triangle,\square}\rangle \equiv \frac{1}{Z}\sum{}' w_n \sum_\alpha |a_{n\alpha}|^2 N_{(\triangle,\square),\alpha}$, where $N_{(\triangle,\square),\alpha}$ is the number of triangular (square) plaquettes which contain one (two) dimer(s) in dimer covering $|d_\alpha\rangle$.

Looking at Eq. (2.35), the main conclusion arrived at is that, when a DM interaction is introduced perturbatively, the low-temperature zero-field powder magnetic susceptibility is not zero but instead approaches a constant that depends on D. Equally important is the observation that, obtaining a quadratic field dependence of the energies as we did, Eq. (2.33), according to Eq. (2.10), the low-temperature zero-field magnetization is zero. This is indeed a good result for it means that the scheme of a short-range valence bond phase plus DM interactions provides qualitative agreement with the experimental observations [30, 72, 51, 37] on herberstmithite of a non-vanishing $T \to 0$ susceptibility and lack of magnetic order. With Eq. (2.33) under our sleeve, in the next sections we place this general result in the context of several spin lattice models. The models that we consider are known or widely believed to capture the assumptions that we made in arriving to Eq. (2.33).

2.3 Application to the Shastry-Sutherland model of $SrCu_2(BO_3)_2$

The first spin model we consider is that illustrated in Fig. 2.6(a). This is the Shastry-Sutherland (SS) lattice, named after its authors who first considered it in 1981 [83]. The model gained more relevance thanks to the compound $SrCu_2(BO_3)_2$ studied in References [42, 59]. The structure of the compound consists of spin-1/2 Cu^{2+} ions forming a topologically equivalent lattice to the SS (see Fig. 2.6(b)). The Cu planes are separated by Sr^{2+} ions. We believe that this model satisfies the assumptions we made in section 4.2 almost exactly, and it is the reason why apply our formalism to this model first.

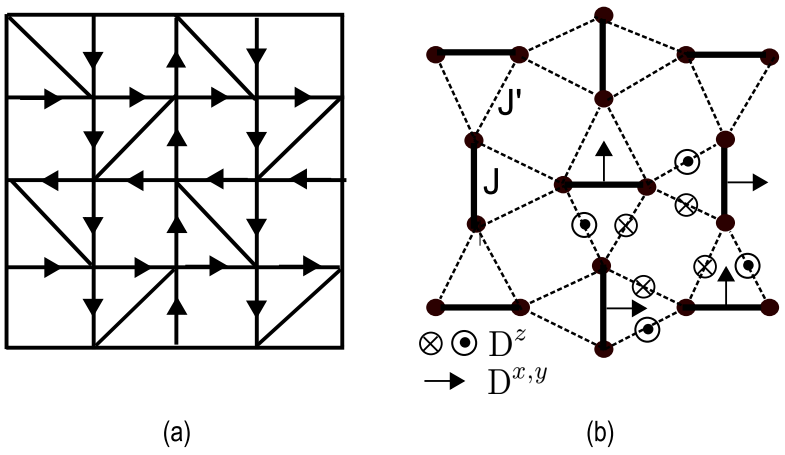


Figure 2.6: (a) The Shastry–Sutherland (SS) lattice. In its ground state, the spins connected by the diagonal bonds form singlets. The arrows on the links denote their orientations in terms of the sign convention for $H_{\rm DM}$, i.e. which spin comes first in the cross product. The orientation of the diagonal bonds can be taken as going from the lower site to the upper site, though this fact will not enter the calculation. (b) The structure formed by the copper ions in $SrCu_2(BO_3)_2$. This is topologically equivalent to the SS lattice. Indicated in this figure are the directions of the $\mathbf{D}$ vectors on the various links, where the orientation convention of (a) has been assumed.

2.3.1 SS Model

The Hamiltonian of the Shastry-Sutherland model is

$$H_0 = J\sum_{\langle ij\rangle}^{\rm diag}\mathbf{S}_i\cdot\mathbf{S}_j + J'\sum_{\langle ij\rangle}^{\rm horiz,vert}\mathbf{S}_i\cdot\mathbf{S}_j, \tag{2.36}$$

illustrating that the interaction between spins depends on whether they are connected via a horizontal, vertical or diagonal bond. The sum is restricted to nearest neighbors along the specified direction, and J and J' are positive constants. Setting $J = 0$ reduces the model to the square lattice Heisenberg antiferromagnet, which is widely believed to have a Néel ordered ground state. If, on the other hand, $J' = 0$, the ground state is a product state of singlets on the diagonal bonds: $|\Psi\rangle = \prod_{\langle ij\rangle}^{\rm diag}(ij)$. Shastry and Sutherland showed that this product state is an exact eigenstate of the full Hamiltonian (2.36); more precisely, a ground state up to a critical value

of J'/J. For strontium copper borate, Ref. [59] determines $(J'/J)_c = 0.71$ and $J = 100$, $J' = 68$, placing the compound very near the transition point. When $J' = 0$, magnetic excitations with spin gap equal to J occur when the singlets in the dimer state are replaced by triplets. In Ref. [59], it was shown that the excitations remain nearly localized with a small dispersion when $J' \neq 0$, except for very close to the transition (in fact, it has been shown that even singlet excitations are gapped [19] in this parameter range). Therefore, in its valence bond phase, the SS model has a spectrum like Fig. 2.3(a), where the low energy sector in this case consists of just one state $|\Psi\rangle$.

In order to apply our formalism, we need to perturb Eq. (2.36) with a small Dzyaloshinskii-Moriya term. For this we keep in mind the rules governing the $\mathbf{D}$ vectors. The model being treated is an ideal two-dimensional lattice, so that only the D^z component is present. For the J' bonds, one finds that the directions alternate (in the squares) as indicated in Fig. 2.6. The J bonds contain a midpoint with inversion symmetry [19], which means, according to the rules, that $\mathbf{D} = 0$. However, in relation to the strontium copper borate compound, $SrCu_2(BO_3)_2$, Ref. [58] cites the occurrence of buckling in the planes that destroys their mirror symmetry. In this case, though, the rules tell us that $\mathbf{D}$ can have a component perpendicular to the bond. Since there are two inequivalent types of J bonds, horizontal and vertical, this implies a different component in each: D^x in the vertical, and D^y in the horizontal. As we anticipate a comparison of our results to the experiments, we consider the DM interactions shown in Fig. 2.6(b). Note that the latter description would be different if given in terms of Fib. 2.6(a).

In adapting Eq. (2.34) to the current model, a few things are in order. First, one notes that $H_{\rm DM}$ couples the ground state to two different bands of magnetic excitations (each of which gets split into three bands upon application of a magnetic field). To see this, let's first consider the $J' = 0$ case, recalling that when $H_{\rm DM}$ acts on a bond, its effect is to transform the containing or emerging singlet(s) into triplet(s). Now, referring to Fig. 2.5(b), we see that case 1 connects

$|\Psi\rangle$ to the set of magnetic eigenstates where one of the dimers is now a triplet. These states have an energy $\Delta_1 = J$ above the ground state. Cases 5 and 6 connect $|\Psi\rangle$ to eigenstates where two of the dimers are triplets (case 8 terms, while not forbidden by the lattice, do not occur in our considered ground state). These states have energy $\Delta_2 = 2J$ above the ground state. These two bands are orthogonal to each other, and for that reason we can consider them separately in the calculation. In particular, the argument which used the assumption of having a narrow band can be easily generalized to the present case because both of these bands are narrow. For instance, one may verify that the proper generalization of Eq. (2.15) is (d_α has been replaced with Ψ because there is a unique ground state):

$$|\Psi'\rangle = |\Psi\rangle - \sum_{S^h} \frac{1}{\Delta_1^{(S^h)}} {\sum_\gamma}' \langle e_\gamma^{(S^h)}|H_{\rm DM}|\Psi\rangle |e_\gamma^{(S^h)}\rangle$$
$$- \sum_{S^h} \frac{1}{\Delta_2^{(S^h)}} {\sum_\gamma}'' \langle e_\gamma^{(S^h)}|H_{\rm DM}|\Psi\rangle |e_\gamma^{(S^h)}\rangle. \qquad (2.37)$$

The sums, being both over the $S = 1$ states, correspond to the bands $E = \Delta_1 = J$ and $E = \Delta_2 = 2J$, respectively. One may still treat these separately when $J' \neq 0$ (away from the transition point) although the values for the energy gaps become renormalized [59, 19] when the excitations acquire a small dispersion (and Δ_2 will no longer be $2\Delta_1$). We will account for this in our calculation by using the actual gap values $\Delta_{1,2}$ in Eq. (2.37).

A similar adaptation is executed for the powder susceptibility. Two separate parts are generated, each of the form of Eq. 2.34, corresponding to the two bands of excited states. Consider the terms associated to the Δ_1 band. Here, we take into account only the terms affecting one dimer. This means that in this case the number of links is equal to the number of dimers. In addition, half of these dimers contain D^x and the other half D^y, each totaling $N/4$. In mathematical terms, $\sum^{(0)} D_{ab}^2 = \sum^{(1)} D_{ab}^2 = N\left[(D^x)^2 + (D^y)^2\right]/4$. The other sums in (2.34) do not contribute in this band. For the terms associated with the Δ_2 band, we look for the contributions coming from two affected dimers, in other words, action of $H_{\rm DM}$ on empty

links. The first sum is $\sum^{(0)} D_{ab}^2 = 4(N/2)(D^z)^2 = 2N(D^z)^2$ (the factor of 4 comes from $(z-1)$, where $z=5$ is the coordination number). The second sum does not contribute because this type belongs in the Δ_1 band. In the third sum corresponding to the triangular plaquettes, $\sum^{(2)} \mathbf{D}_{ab} \cdot \mathbf{D}_{ac}$, the contribution of each triangle is the same, namely $\mathbf{D}_{ab} \cdot \mathbf{D}_{ac} = -(D^z)^2$ (in the two bonds involved, the D^z's point in the opposite direction, the reason for the minus sign), and there are two of these triangles for every dimer, $2N_d = N$. The case represented by the fourth sum does not occur here. Collecting all terms, the final result is

$$\chi_{\text{powder}} \approx \frac{N(g\mu_B)^2}{12} \left(\frac{(D^x)^2 + (D^y)^2}{\Delta_1^3} + \frac{8(D^z)^2}{\Delta_2^3} \right). \tag{2.38}$$

The fact that the low energy sector of the unperturbed model consists of a unique state which is a dimer covering indicates that there are no more terms in the overlap expansion beyond the diagonal term kept in the approximation. Briefly stated, the overlap expansion is exact, and the only approximations in Eq. (2.38) are those inherent in perturbation theory.

2.3.2 Comparison with experiment

The most prominent feature of the temperature dependence of the zero field[1] susceptibility of $SrCu_2(BO_3)_2$ is a peak, which occurs around $T = 18.5$ K, followed by a rapid decrease to nearly zero as the temperature is further lowered [42]. The interpretation given to this fast decay is a reduction of entropy as the physics becomes increasingly dominated by a non-magnetic ground state. After conducting ESR measurements, Nojiri et al. [69] reported having found two sets of triplet excitations with spin gaps $\Delta_1 \approx 35$ K and $\Delta_2 \approx 55$ K, respectively.[2] As stated there, the latter gap indicates that there is a strong interdimer coupling.

[1]The experiments we are referring to (Ref. [42]) were actually done in a magnetometer with a static field of $H = 1.0$ T, which for spin 1/2 corresponds to an energy scale $g\mu_B H \sim 1.3$ K. The temperature range of the experiment is from 1.7 K to 400 K, so the results can be interpreted by a zero-field theory except for perhaps the very lowest temperature points.

[2]Measurements of the NMR relaxation rate [42] determined the gap to the lowest magnetic state to be $\Delta_1 = 30$ K, consistent with the value of $\Delta_1 = 35$ K given in Ref. [69]. Fitting the susceptibility data gave a slightly lower value of $\Delta = 19$ K but these and other authors [59] have interpreted the ≈30 K values as the "spin gap". Therefore, we use this value for our estimate.

As previously mentioned, Ref. [59] determined $J'/J \approx 0.68$ for $SrCu_2(BO_3)_2$. This was based on their analysis of the temperature behavior of the susceptibility. With these parameter values, they found that the compound was adequately represented by Eq. (2.36). Although Eq. (2.36) has been successful at explaining the ground state and excitations of the material, there are certain experimental features that could not be included in this description. It was shown [19, 58, 57] that by including DM interactions, the model could also explain a number of features that occurred in the presence of a magnetic field, such as the appearance of uniform and staggered magnetizations [42, 45] in fields small compared to the spin gap scale.[3]

Given in Eq. (2.38) is the predicted behavior of the magnetic susceptibility at zero magnetic field and under the effect of DM interactions. Obtained in the limit of $T \to 0$, (2.38) shows that the susceptibility approaches a finite value rather than decaying to zero. Next, we determine this value from our derived expression by utilizing previously calculated parameters. From the ESR measurements of [69], we use $g \approx 2$, $\Delta_1 \approx 35$ K and $\Delta_2 \approx 55$ K; the estimated value of $D^z \approx 2$ K from [19]; and the suggestion of Ref. [58] that $D^{x,y} \sim D^z$. In order to compare our result with that of experiment, we multiply Eq. (2.38) by the factor N_A/N, where N_A is Avogadro's number, obtaining the molar susceptibility. Putting the numbers in, we get $\chi_{\text{powder}}(T=0) \approx 5 \times 10^{-5}$ emu/mol Cu. According to measurements by Kageyama et al. [42], the susceptibility (Fig. 2 in the paper) does not show a saturation to a finite value, but instead it is observed rising with decreasing temperature, after reaching a minimum of approximately 5×10^{-4} emu/mol Cu at around 4 K. As reported by the authors, this upturn seems to be due to magnetic impurities and/or defects of the copper ions. Precisely assessing the accuracy of Eq. (2.38) demands for more experiments on cleaner samples. Nevertheless, we reiterate that the assumptions made in our model are expected to hold well for the SS model, so to the extent

[3]The spin gap scale is $\sim \Delta/g\mu_B \sim 20$ T while the onset of a uniform magnetization is seen at around 18 T. We point out that these interesting field dependencies occur at fields much higher than the 1.0 T field of the magnetometer used in Ref. [42], the results of which we interpret with our zero field calculation.

that Eq. (2.36) with DM included is a good model of $SrCu_2(BO_3)_2$, we expect our order of magnitude estimate to be reliable.

2.4 Application to the generalized Klein model on the checkerboard lattice

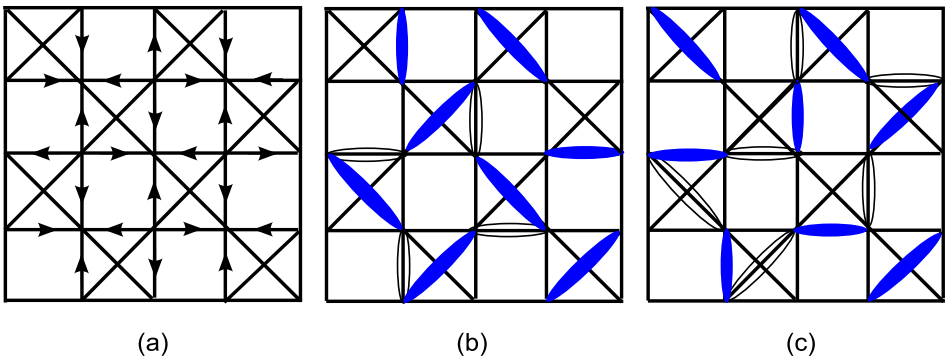


Figure 2.7: (a) The checkerboard lattice with arrows specifying the orientations of links with DM interactions. On horizontal and vertical links, we take $\mathbf{D} = D^z\hat{z}$ (i.e. the sign is always positive) while on diagonal links $\mathbf{D} = 0$. (b) The minimal loop on this lattice has length 8. (c) The next minimal loop has length 12.

In this section we apply our results to a toy model defined on the checkerboard lattice, shown in Fig. 2.7(a). What makes the connectivity of this lattice different from the square lattice are the additional diagonal bonds on alternate plaquettes. The sites connected by these bonds (not the crossing point) are considered nearest neighbors as well. The checkerboard lattice can be viewed as the two-dimensional projection of the three-dimensional pyrochlore lattice.

Experimental realizations of the checkerboard lattice have so far not been seen. Although materials exist [16] that possess a pyrochlore structure, we are unaware of any whose low-energy properties can be captured by a short-range valence-bond description. Notwithstanding, the theoretical motivation that brings us to this system should compensate for the

absence of a material representation. First, the model to be considered is among those for which the Hamiltonian and exact ground states are known. We also expect the assumptions presented in Section 4.2 to hold to a decent approximation and, for a reason to be stated later, the overlap expansion should converge fairly well. In short, this systems offers a scenario on which to test our formalism.

The generalized Klein model, introduced in Ref. [76], is written as

$$H = \sum_p \hat{h}_p \tag{2.39}$$

where the sum is over *crisscrossed* square plaquettes and

$$\hat{h}_p = (S_p^2)(S_p^2 - 2). \tag{2.40}$$

Here we have defined $\mathbf{S}_p \equiv \mathbf{S}_1 + \mathbf{S}_2 + \mathbf{S}_3 + \mathbf{S}_4$ as the total of the four spins located at the sites of plaquette p. As we do throughout this chapter, here we consider $\mathbf{S}_i = 1/2$. Since

$$\frac{1}{2} \otimes \frac{1}{2} \otimes \frac{1}{2} \otimes \frac{1}{2} = 0 \oplus 0 \oplus 1 \oplus 1 \oplus 1 \oplus 2 \tag{2.41}$$

the maximum S_p is 2. $\hat{h}_p$ is an operator that projects[4] the wave function onto this maximal value, annihilating any $S = 0$ and $S = 1$ components. The Hamiltonian (2.39) is a sum of projection operators of this type. This means that its eigenvalues are non-negative and that any state with zero eigenvalue is a ground state of it.

Considering an individual (crisscrossed) plaquette, one observes that, if the plaquette contains a dimer on any of its bonds, application of h_p on the resulting state yields the annihilation of the latter. The reason is that, by coupling two spins into a singlet, the total spin can be at most 1. Hence, a wave function having a dimer on every crisscrossed plaquette is a ground state of the Hamiltonian (2.39) with energy zero. References [76] and [70] give a counting argument proving that the wave functions constituting the ground-state manifold of Eq. (2.39)

[4]Note that, in our definition, Eq. (2.40) is missing a factor of $1/24$ in order to normalize the largest eigenvalue to 1 as it is for any projection operator.

are only dimer coverings, and their superpositions, with exactly one dimer in each crisscrossed plaquette. One can construct other types of dimer coverings, but which are not ground states of the Hamiltonian. For instance, a perfectly acceptable dimer covering is one where crisscrossed plaquettes contain two dimers. Although these are locally in a ground state, this arrangement necessarily leaves other crisscrossed plaquettes with no dimer at all, so overall the wave function has a non-zero eigenvalue. Having said that, we review the validity of our model's assumptions on the current system. So far, we have just seen how short-range dimers are at the base of this system, with states of the form described making up a degenerate ground state manifold. In regards to its excited spectrum, although it has not been proven, it is strongly suspected that Eq. (2.39) has a spin gap, and demonstrations of the existence of one have been attempted on various instances [48, 1, 76, 17]. Hence, the reasons remain strong that the generalized Klein Hamiltonian on the checkerboard lattice satisfies the requirements of our formalism.

Given the degeneracy of the ground state, we recognize the importance of the overlap expansion, which is directly related to the loop structure of the lattice. In the transition graph of Fig. 2.7(b), we show that the minimal loop that gives rise is of length 8, while the next one has length 12, an example of which is given in Fig. 2.7(c). By keeping only the diagonal terms as we did in our derivation, Section 2.2.1, having loops of the mentioned lengths introduces a relative error of $\sim x^{(12-8)} \sim x^4$. Compared to other lattices, such as the square whose error is $\sim x^2$, the error for the checkerboard lattice provides a very good reason to expect that the overlap expansion will be a good approximation.

We are now in the position to start introducing the Dzyaloshinskii-Moriya interactions. In this case we do not have a real material to compare with. Therefore, the fact that we are dealing with an ideal two-dimensional lattice signifies that the only component of $\mathbf{D}$ present is the D^z. There are three types of links, namely vertical, horizontal and diagonal. The latter's midpoint is a center of inversion symmetry, so $D^z = 0$ here too. Following the orientation

convention depicted in Fig. 2.7(a), we assume $\mathbf{D}^z$ to have the same magnitude and sign on all the links. As we adapt Eq. (2.35) to the checkerboard lattice, we note that all the non-zero contributions of the general lattice are applicable. The first sum will give $\sum^{(0)} D_{ab}^2 = 2N(D^z)^2$, where $2N$ is total number of non-diagonal links. The second sum over dimers counts all possible dimers ($N/2$) excluding those on the diagonal bonds (N_{diag}): $\sum^{(1)} D_{ab}^2 = (D^z)^2(\frac{N}{2} - N_{\text{diag}})$. As for the triangular terms, there are two of these for each diagonal dimer and $\mathbf{D}_{ab} \cdot \mathbf{D}_{ac} = (D^z)^2$. The square terms proceed from the squares, not the crisscrossed, having two dimers (on opposite sides). From the orientation convention, these contribute $-(D^z)^2$. Substituting into Eq. (2.35), we obtain

$$\begin{aligned}\chi_{\text{powder}} &= \frac{(g\mu_{\text{B}})^2(D^z)^2}{6\Delta^3}\Big[2N + \frac{1}{Z}\sum_n e^{-\beta E_n}\sum_\alpha |a_{n\alpha}|^2\left(\frac{N}{2} - N_{\text{diag}}\right) - 2(2N_{\text{diag}}) + 2N_{\square}(-1)\Big] \\ &= \frac{5N(g\mu_B)^2(D^z)^2}{12\Delta^3}\left[1 - \frac{2\langle N_{\text{diag}}\rangle}{N} - \frac{4\langle N_{\square}\rangle}{5N}\right] + O(x^8) \qquad (2.42)\end{aligned}$$

where, $\langle\cdots\rangle$ denotes thermal average as per the discussion after Eq. (2.35).

One thing that suggests itself for further study of this system is a numerical analysis studying the low energy sectors. Concretely determining the presence of a spin gap would provide a validation for our approach.

2.5 Application to the kagomé lattice and $ZnCu_3(OH)_6Cl_2$

In the present section, we turn to the system that initially motivated us to examine the effects of Dzyaloshinskii-Moriya interactions on valence bond systems. This system is the kagomé lattice, studied in the context of herbertsmithite, the $ZnCu_3(OH)_6Cl_2$ compound (see Fig. 2.1). Unlike the systems in sections 2.3 and 2.4 which had well-characterized Hamiltonians and ground states, the material is believed to be principally governed by $S = 1/2$ antiferromagnetic Heisenberg spins forming a kagomé lattice (i.e., to be a kagomé Heisenberg antiferromag-

net (KHAF)). But, despite the features the system is generally believed to posses, the KHAF still represents an unfinished project and for that reason one whose ground state has not been absolutely determined. For our purposes, we assume that the compound is indeed described by a KHAF, albeit the details of this are unnecessary for our analysis, so long as its spectral properties are well represented by Fig. 2.3.

We proceed by first reviewing some known properties of the KHAF that indicate a very good satisfaction of our formalism's assumptions. Then we adapt our general result of the susceptibility, Eq. (2.35), to the present case, only to be followed by a discussion of our results in terms of the experiments. To date, most theoretical investigations of this material have put an emphasis on the KHAF. However, there is not yet a consensus on what model best describes herbertsmithite.

2.5.1 Model

As it was already mentioned in the Motivation, exact diagonalization studies of the KHAF have suggested that the ground state is nonmagnetic [46, 92] and that the system has a spin gap of the order of $J/20$ [92]. Found within the gap was an exponentially (in the system size) large number of nonmagnetic states, said to be become a gapless continuum, adjacent to the ground state, in the thermodynamic limit. Reference [92] asserted that, because of the small gap (smaller than J) and the nonmagnetic continuum, the inclusion of long-range valence bonds in a singlet product representation was necessary. Yet, on a different study [49], restricting to nearest-neighbor valence bonds obtained the same continuous gapless spectrum that was calculated exactly. Not only was this captured, but also the exponentially-increasing number of these states.

In a more recent work by Singh and Huse [86] based on series expansions on the KHAF Hamiltonian, the energies of various dimer states were analyzed. The authors found a

state, denoted as the honeycomb valence bond crystal, that was favored among the others as the optimal of all dimer coverings. These other states had an energy that was very close, within a bandwidth that was smaller than the spin gap. (This honeycomb VBC state, consisting of so-called perfect hexagons, had already been noted by Marston and Zeng [50] a few years earlier.) The ground state energy per bond estimated in Ref. [86] was comparable to that found by exact diagonalization techniques of the same model. Put together, these facts suggest that spectra such as Fig. 2.3(a,b), where the low energy physics is determined by a narrow band of dimer states, are decent caricatures of what happens in the KHAF. Singh and Huse's continuation of the above work [87] reaffirms what was just said plus, it is consistent with the assumption in section 4.2 of a narrow $S = 1$ band. Namely, for an infinite-lattice model of the honeycomb VBC phase mentioned before, they found the lowest triplet excitation to have a spin gap of approximately $0.08J$ and a bandwidth of only around $0.01J$. Despite the absence of a Hamiltonian on the kagomé lattice for which it can be explicitly shown that all our assumptions in section 4.2 are satisfied, based on the results we have just cited, we believe that these assumptions are reasonable as it pertains the KHAF model.

As it is the customary order now, we proceed to the adaptation of Eq. (2.35) to the $ZnCu_3(OH)_6Cl_2$ compound. Were we dealing with the ideal two-dimensional kagomé lattice, the DM $\mathbf{D}$ vectors we add when perturbing the system would contain only the out-of-plane component D^z. However, in the material, the (OH) groups that mediate the superexchange of the copper ions break the mirror symmetry of the lattice. Therefore, since the midpoint of every bond of the lattice does not possess inversion symmetry, $\mathbf{D}$ can exist in all the links and with both, in-plane and out-of-plane components. Once an initial choice is made for the $\mathbf{D}$ vectors, the rest follows from symmetry considerations. The convention we have adopted for the orientation of the pair $\langle ij \rangle$ in the Hamiltonian (2.6) is illustrated in Fig. (2.8). We immediately

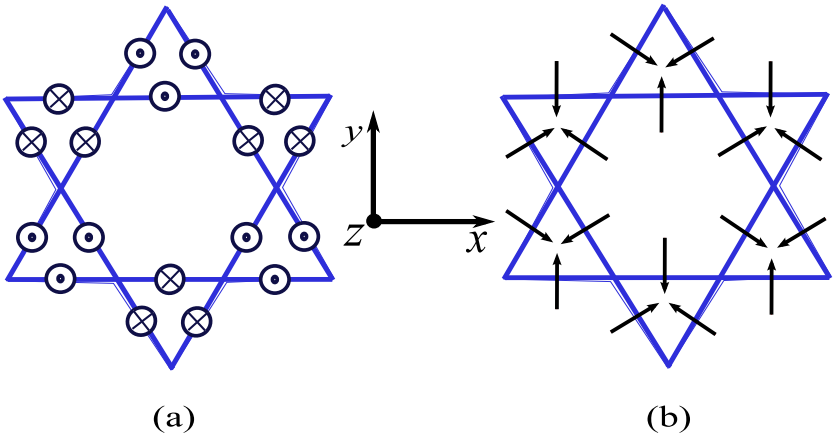


Figure 2.8: The relations between the directions of the (a) out-of-plane and (b) in-plane components of the DM vectors for nearest-neighbor interactions in the kagomé lattice are summarized. The directions are determined by the physical requirement that $H_{\rm DM}$ preserves the symmetries of the lattice, but also by the convention of how we orient the links as they appear in the Hamiltonian. The figure uses the convention of Ref. [80] where the DM interaction on the link $\langle ij \rangle$ appears in the Hamiltonian with the lower spin or, on horizontal links, the left spin, being the first member of the cross product. A different choice, which is sometimes convenient, is where the links are oriented clockwise around each triangle. [22] In this convention, all of the D^z's come with the same sign.

observe that case 8 of Fig. 2.5(b) does not occur here. The number of links for this lattice is $4N/2$ with 4 being the coordination number z. The number of dimers is given by $N/2$. In the case of the triangular terms, we have every dimer belonging to a triangular plaquette. Thus we need to compute the contribution of each. For a dimer occupying the link $\langle bc \rangle$ of a particular triangle, the two $\mathbf{D}$ vectors involved are, according to Fig. (2.8), $\mathbf{D}_{ab} = \frac{\sqrt{3}}{2} D_p \hat{\mathbf{x}} - \frac{1}{2} D_p \hat{\mathbf{y}} + D^z \hat{\mathbf{z}}$ and $\mathbf{D}_{ac} = -\frac{\sqrt{3}}{2} D_p \hat{\mathbf{x}} - \frac{1}{2} D_p \hat{\mathbf{y}} + D^z \hat{\mathbf{z}}$, which gives $\mathbf{D}_{ab} \cdot \mathbf{D}_{ac} = -\frac{1}{2}(D^p)^2 + (D^z)^2$. Substitution into Eq. (2.35) yields

$$\begin{aligned} \chi_{\rm powder} &\approx \frac{(g\mu_{\rm B})^2}{6\Delta^3} \left(\frac{5}{2} N D^2 - 2 \frac{N}{2} \left[-(1/2)(D^p)^2 + (D^z)^2 \right] \right) + O(x^6) \\ &= \frac{(g\mu_{\rm B})^2}{4\Delta^3} N \left(2D^2 - (D^z)^2 \right) + O(x^6). \end{aligned} \tag{2.43}$$

2.5.2 Comparison with experiment

One outstanding feature of $ZnCu_3(OH)_6Cl_2$ that has been observed by different experimental techniques [30, 72, 51, 37] is the lack of magnetic order for temperatures as low as ~ 50mK. This finding is consistent with our result that a weak DM does not induce a zero field magnetization, as can be verified by Eq. (2.10) and Eq. (2.33). Our main result, Eq. (2.43), is an expression for the $T = 0$ powder susceptibility. Next, we determine the implication of this result on the magnitude of the DM interactions. To do this, we assume that $D^z \approx D$; $\Delta \sim J/20$ [92] or possibly a little higher $\sim J/10$ [87]; and $J \sim 170$ K [81].

One experiment suggesting that the susceptibility saturates in the $T \to 0$ limit is that by Ofer et al. [72]. They measured χ_{powder} using μSR in a 2 kG magnetic field at temperatures ranging from 60 mK to 200 K. The susceptibility is observed increasing monotonically with decreasing temperature up to around 200 mK, below which it saturates to $\chi_{\text{powder}} = 15.7(5) \times 10^{-3}$ cm^3/mol Cu. With the use of (2.43), this value is compatible with D ranging from $0.03J$ to $0.08J$, based on the gap values cited before.

The second experiment we discuss here indicating a finite χ in the limit of $T \to 0$ is a ^{17}O NMR study by Olariu et al. [73]. This technique can identify the various contributions to the susceptibility. The magnetic energy $g\mu_B h$ corresponding to the 6.5 T field used in the experiment is comparable to our lower estimate of the gap, $\Delta \sim J/20$. This fact introduces some doubt about the direct application of Eq. (2.43), which was derived under the assumption that the Boltzmann factors of the excited states were relatively small compared to the low energy manifold. However, if the actual gap is closer to the higher value, $\Delta \sim J/10$, then (2.43) might produce a reliable estimate. The measurements of Ref. [73] suggest [18] a $T = 0$ susceptibility per spin of $\chi = 0.13$ which implies a molar susceptibility of $\sim 1.1 \times 10^{-3}$ emu/mol Cu. From Eq. (2.43), this implies that D ranges from $0.008J$ to $0.02J$.

A word of caution must be given along with the estimates above. The numbers cited for the susceptibility depend on a limited number of data points and in both experiments it is uncertain that DM interactions are the only factors playing a role. Also, the qualitative dependence of χ on the temperature is different in both experiments, so both cannot explain the same quantity we are calculating. Our results, however, seem to suggest that the magnitude of the DM interactions may be considerably smaller than other previously stated values. We discuss this in the next section.

2.6 Discussion

In this chapter our main focus was the $ZnCu_3(OH)_6Cl_2$ compound whose synthesis engendered an abundant number of both experimental and theoretical studies. Based on the early findings, the material appears to have a nonmagnetic low-temperature phase, although its nature is still not fully understood. Owing to its nonmagnetic state, the system can be regarded in terms of either a short-range or long-range valence bond phase. In section 2.5 we were able to show that a very good low-temperature description of the system is achieved when a short-range valence bond phase is combined with a small DM interaction. Overall, this analysis was able to reconcile the outstanding features of herbertsmithite: observation of a nonmagnetic order; apparent absence of a spin gap; and known facts of the kagomé Heisenberg antiferromagnet. To conclude this chapter, we would like to discuss our results in light of other theories and experiments.

From an analysis of high-temperature electron spin resonance (ESR), Zorko *et al.* [98] determined the magnitude of the DM coupling constants as $|D_z|/J \sim 0.08$ and $|D_p|/J \sim 0.01$. These numbers are somewhat smaller than those reported by Rigol and Singh [81]. Here, numerical fits of the pure Heisenberg model with DM perturbations as well as high-temperature

expansions can only account for the observed experimental data in the high temperature region ($T > 0.3J$). Recalling that our estimates of D are based on an analysis of the low-temperature susceptibility, we allude to Imai *et al.*'s [37] observation in order to try to explain the discrepancy in the numbers just listed and ours. Their observation is that lattice fluctuations occurring at high temperatures but slowing down below $50K$, could be due to the OH bonds slow freezing. As mediators of the superexchange mechanism between the Cu spins, the OH bonds are responsible for the crystalline electric field on the magnetic atoms, making them a relevant point in the discussion. As these OH bonds freeze into a fixed random orientation, one expects their effect to be significant on $\mathbf{D}$, which depend on their position. Stated differently, it could very well be that the the strength of $\mathbf{D}$ at low T is different than that suggested by the above references [98, 81]. Only a determination of D from low-temperature ESR data could tell whether or not this is the case.

One thing that gives confidence to our estimates of small D is the fact that, for sufficiently large D^z, the KHAF is expected to order magnetically. In the case of classical Heisenberg spins, Elhajal *et al.* [22] found that, regardless of how small the DM interactions are, the system would prefer a long-range three-sublattice 120° structure in the $x-y$ plane (the chirality being dependent on the sign of D^z). As a matter of fact, in the quantum limit, it is also anticipated that some magnetic order is induced [78, 31] by the presence of DM in an algebraic spin liquid description. However, as it has been noted throughout, herbertsmithite does not show any indication of order, in contradiction with both, the semiclassical and algebraic spin liquid pictures.

Another study investigating the KHAF with DM interactions is that of Cepas *et al.* [18], done by the exact diagonalization methods. The authors found that the nonmagnetic phase observed when $D = 0$, i.e. when only the Heisenberg Hamiltonian is considered [46, 92], persists up to a critical value $D_\mathrm{c} \sim 0.1J$. It is said that the system undergoes a phase transition

to a Néel state above this value. The fact that the system is not magnetically ordered below D_c is consistent with the current lack of any experimentally observed magnetic order or phase transition (of $ZnCu_3(OH)_6Cl_2$). According to these results, the system of Ref. [98] is very close to the transition, while ours is put deeper into the nonmagnetic phase. Overall, Ref. [18], together with our results, form a theoretically self-consistent picture because our calculation assumes a nonmagnetic phase.

In assuming the picture of a short-range valence bond phase, we worked within the limitations of our formalism. In particular, the reliability of our results directly depends on the accuracy of the overlap expansion. Obtaining a more accurate expansion is only possible if one were to work with systems having weaker fluctuations. Another question our formalism cannot answer is that of the nature of the phase. However, the place where our calculations can find application and do so more reliably are those phases that maximize the number of perfect hexagons. Studies concentrating on this aspect are those of Marston and Zeng [50], Nikolić and Senthil [68], and more recently that of Singh and Huse[86] (although recent DMRG studies question the VBC nature of the ground state [85]).

The discussion would not be complete if we omitted a mention of the long-range counterpart of the above picture. With this we mean an alternative nonmagnetic view based on a long-range valence bond phase. As it was stated early in the introduction, these phases are spin gapless by construction. This immediately would explain the absence of a spin gap in the experiments. However, it would not describe the spin gap feature of the KHAF, as determined numerically. On another study of the properties of a spin liquid [78], this phase was found to exhibit a susceptibility of the form $\chi \sim T$ at low temperatures. Again, this does not agree with the saturating susceptibility observed experimentally in this region of temperature. And, as stated before in regards to an algebraic spin liquid [31], DM interactions drive the system into a magnetically ordered state, contradicting observations.

We close this chapter by restating the principal result of our investigation. Starting with a system in a short-range valence bond phase, we were able to demonstrate that the presence of Dzyaloshinskii-Moriya interactions could account for a non-vanishing zero-temperature magnetic susceptibility, while keeping the magnetization at zero. As it applies to the herbertsmithite, we could establish agreement with experiment and this approach was good for estimating the strength of the DM coupling constants.

Chapter 3

Ghost-Mediated Interactions Between Domain Walls in the Diamondback Ladder

3.1 Introduction

Determining the ground state properties of low-dimensional frustrated magnets represents a difficult challenge. However, some advances have been made in this front for some systems, even if a consensus has not been entirely reached. Such is the case of the spin-1/2 antiferromagnetic Heisenberg model on the kagomé lattice whose ground state nature has been heavily investigated [50, 92, 68, 86, 87, 39, 85]. Also, despite these studies' concurrence on the existence and value of the spin triplet gap, there is still no good analytical understanding of the nature of the spin excitations. Hence, other ways have to be found that can yield some insight. One of these ways is considering *simpler* systems that could mimic the physics of the kagomé antiferromagnet. The study of Hao and Tchernyshyov [29] in 2009 is such an attempt.

There, the authors considered the Heisenberg model on the sawtooth chain and the Husimi cactus, in which spins occupy vertices of corner-sharing triangles – similar to the kagomé lattice, albeit some spins in the sawtooth chain (Fig. 3.1) are not shared among two triangles. As we will see later, the corner-sharing nature of these lattices is important; lattices such as the triangular lattice lack this feature leading to a markedly deferent physics. In this chapter, we consider the diamondback ladder (Fig. 3.2) which does possess this important component. We study its spin excitations in hope to shed some light on the paradigmatic kagomé .

Before getting into the heart of our problem, we first outline the results of Ref. [29]. Having an understanding of this previous work will make our objective more intuitive. First, we review the ground states of the chain, which are easier to understand if one considers the equivalent form of the Heisenberg Hamiltonian as given below,

$$\begin{aligned} H &= J \sum_{\langle ij \rangle} \mathbf{S}_i \cdot \mathbf{S}_j \\ &= J/2 \sum_{\triangle} \mathbf{S}_{\triangle}^2 + \text{const}, \end{aligned} \tag{3.1}$$

where the sum is taken over all triangles in the lattice of the total spin squared, $\mathbf{S}_{\triangle}^2$. Thus written, one immediately observes that the exchange energy in each triangle is minimized, and so is the total energy, when the total spin of each triangle attains its minimum value. This occurs when two of the spins are paired into a singlet, leaving a total spin of $S = 1/2$. Although there are three possible ways of pairing two spins, only two are linearly independent. This results in the system having two degenerate ground states, (L) and (R), which correspond to the singlet being on the left and right bond, respectively, of each triangle (Fig. 3.1). When a spin-1 excitation occurs, the two spinons (spin-1/2 quasiparticles) that are produced become the domain walls between the two ground states as shown in Fig. 3.1. The kink, separating the (L) and the (R), remains localized in a stationary state of the system at no energy cost, as can be observed from its position in a local ground state environment. The other spinon, the antikink, acts as a mobile

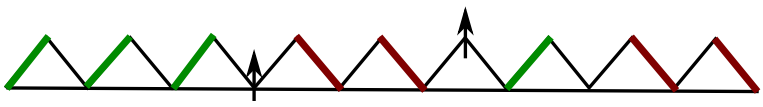


Figure 3.1: The sawtooth chain has two ground states, the (L), designated by the green singlets, and the (R), designated by the red singlets. When a spin-1 excitation decays into two spinons, a (stationary) kink – the boundary between the (L) and the (R) states –, and a (mobile) antikink – the boundary between the (R) and the (L) states – are released. The antikink, being a local non-zero excitation can gain energy by delocalization. See the text for more details.

domain wall between the (R) and the (L), only restricted in motion by the presence of a kink. The antikink is a non-zero energy excitation characterized as a triangle with spins not in their ground state, i.e., as a triangle with no singlet. While a kink incurs no energy penalty, it can only be created as a pair with an antikink, and for this reason kinks cannot freely proliferate. According to a tight-binding calculation [29], the antikink can significantly reduce its energy by delocalization, and the minimum energy of the pair is $J/4$. The antikinks discussed here are the subject of our study in this chapter. It turns out that the treatment in Ref. [29] of the antikinks as free non-interacting particles is a good approximation in the sawtooth chain, but not in our system of study, which is a better approximation of the actual kagomé lattice, and where interactions cannot be ignored.

The objective of this investigation is to determine a controlled approximation accounting for the interactions among the antikinks in the *diamondback* ladder, shown in Fig. 3.2. As we delve into this search, we stress the fact that the (excitation) interactions in the diamondback ladder cannot be ignored. The reason for this, which is also why neglecting the interactions in the sawtooth chain was permitted, is based on a counting argument first introduced by Elser [23]. A general conclusion that follows from this argument is that, for any finite-dimensional lattice of corner-sharing triangles[1], 1/4 of all triangles always appear without a dimer; this, in the

[1] In a lattice of corner-sharing triangles, all sites are shared between two triangles.

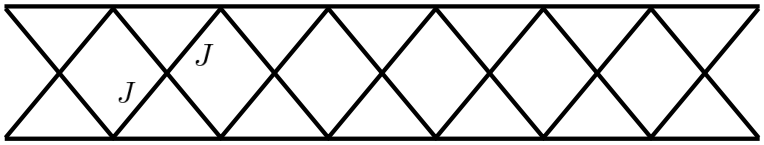


Figure 3.2: The diamondback ladder with coupling constant J. $S = 1/2$ spins occupy each site of the lattice.

case of a dimerized state. Differently stated, in lattices with these properties, there is *inevitably* a finite (1/4) concentration of "defects". These so-called defect triangles are equivalent to the antikinks, whose interactions we intend to investigate. This assertion tells us that, in the saw-tooth chain where not all sites are shared among two triangles, excitations can be very dilute and hence their interactions can be ignored. However, in lattices such as the kagomé , hyperkagome, and the diamondback that we consider here, the defects are not dilute, and their interactions are strong and consequential.

In the following, we develop a perturbative approach to treat the domain wall interactions in a regime where their concentration is still low. As will be demonstrated in this work, antikinks (created in pairs with kinks) become beneficial to the system at a critical point, above which they begin to proliferate. Our study also finds the *ghost-mediated*[2] antikink–antikink/kink interactions to 1) be an oscillatory function of their separation: attractive if the separation is even, repulsive if it is odd; 2) decay with a power-law of exponent less than 1. For a qualitative perspective, starting from a pure, non-interacting case, we also observe the effects of interactions on the wave function as the strength of the latter is gradually incremented. Finally, we make an attempt to speculate about the nature of the ground state in the presence of a finite concentration of interacting defects. The chapter closes with an overall discussion of the results and their implications for the state of the system, as well as possible future directions for the present project.

[2] "Ghosts" will be defined later in the text.

3.2 Model

We consider the Heisenberg model on the diamondback ladder, where each site is occupied by an $S = 1/2$ spin. The Heisenberg Hamiltonian

$$H = J \sum_{\langle ij \rangle} \mathbf{S}_i \cdot \mathbf{S}_j \tag{3.2}$$

is written for nearest-neighbor pairs $\langle ij \rangle$ with coupling constant $J > 0$. A direct manipulation of the many-body antikink interactions is an intractable problem, so next we develop a perturbative approximation that can account for these interactions.

3.2.1 Decoupling the diamondback ladder's chains by perturbation theory

The first step is the introduction of different coupling constants (Fig. 3.3(a)) in the upper (downward-pointing triangles) and lower (upward-pointing triangles) chains of the ladder. The couplings are J and K, respectively. With these definitions, we identify two extreme cases: (i) $K = 0$, corresponding to Hao and Tchernyshyov's sawtooth chain with non-interacting antikinks; (ii) $K = J$, representing the uniform diamondback ladder. In the latter case, according to the counting argument given before, the ladder contains a finite concentration of antikinks, indicating that interactions cannot be neglected. This regime is beyond the reach of our perturbation theory. With our theory, however, we consider the intermediate case of $0 < K \ll J$ (later on, we will relax this assumption in order to see where our approximation breaks down).

An immediate consequence of the assumption $J \gg K$ is that the system would like to optimize the upper chain first. This results in the formation of a valence bond (dimer) in each of its triangles, as illustrated in Fig. 3.3(b). One can also imagine placing domain walls in the upper chain: the antikinks, as indicated by the shaded triangle, and the kinks, represented by site 5. Note however, that in our system a different type of kink can arise as well, corresponding

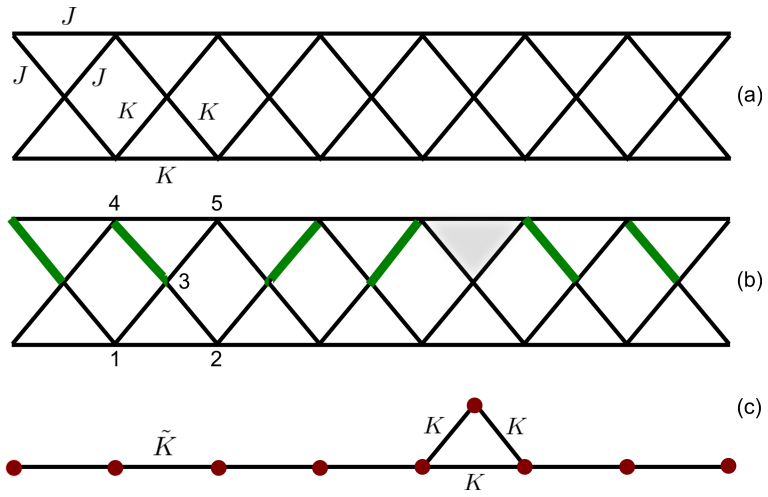


Figure 3.3: The diamondback ladder. (a) In order to treat the interactions in the system, we first allow for different couplings in the upper and lower chains under the assumption $K \ll J$. (b) The upper chain is optimized when (most of) all the triangles contain a singlet (green bond); an excitation of the system can be considered by placing some domain walls (kinks and antikinks). (c) With the strong couplings above dominating the picture, the lower chain can be effectively reduced to a renormalized Heisenberg chain with defects, *ghosts*, produced by the domain walls in the upper chain. Where no defects are present, the spins interact with a weaker coupling $\tilde{K} = K - \frac{K^2}{2J}$.

to the situation where a dimer forms along the upper leg, such as a singlet between sites 4 and 5. While this configuration is a perfectly valid ground state for the triangle, it leaves site 3 completely free. To denote the distinction between the two types of kinks, we refer to the first one discussed as type A, and the second as type B. A complete picture can only be acquired with a notion of the state of the lower chain. To determine this, we first employ perturbation theory to *disconnect* the lower from the upper chain. From Fig. 3.3(b), we see that accomplishing this means integrating out sites of the 3 type, which form a singlet with a spin in the upper chain, site 4. We proceed by considering the following terms in the Hamiltonian,

$$\begin{aligned}\tilde{H} &= J\mathbf{S}_3 \cdot \mathbf{S}_4 + K(\mathbf{S}_1 \cdot \mathbf{S}_2 + \mathbf{S}_2 \cdot \mathbf{S}_3 + \mathbf{S}_1 \cdot \mathbf{S}_3) \\ &= \frac{J}{2}(\mathbf{S}_3 + \mathbf{S}_4)^2 + K\mathbf{S}_3 \cdot (\mathbf{S}_1 + \mathbf{S}_2) + \frac{K}{2}(\mathbf{S}_1 + \mathbf{S}_2)^2, \end{aligned} \tag{3.3}$$

where the numbering refers to the sites indicated in Fig. 3.3(b) and an insignificant constant has been neglected. The unperturbed Hamiltonian corresponds to the case $K = 0$ so that $H_0 = J/2(\mathbf{S}_3 + \mathbf{S}_4)^2$. $H_1 = \tilde{H} - H_0$ is added perturbatively. As already anticipated, the ground state of H_0 is given by the singlet combination of spins 3 and 4, denoted as (34), with ground state energy $E_0 = 0$. To first order, the only non-vanishing energy correction is given by $E^{(1)} = \frac{K}{2}(\mathbf{S}_1 + \mathbf{S}_2)^2$, as determined from $E^{(1)} = \langle(34)|H^1|(34)\rangle$. Proceeding to second order,

$$E^{(2)} = \sum_i \frac{|\langle[34]_i|H_1|(34)\rangle|^2}{E_0 - E_1^{(i)}}. \tag{3.4}$$

Here, the sum is over the triplet states $[34]_{\pm 1}$ and $[34]_0$, where the subscript indicates the value of the total S^z component. In this order of perturbation, the term $K/2(\mathbf{S}_1 + \mathbf{S}_2)^2$ does not act upon the states and the calculation reduces to a simple inner product of orthogonal states. Then, Eq. (3.4) above reduces to

$$\begin{aligned} E^{(2)} &= \sum_i \frac{|K\langle[34]_i|\mathbf{S}_3 \cdot (\mathbf{S}_1 + \mathbf{S}_2)|(34)\rangle|^2}{E_0 - E_1^{(i)}} \\ &= -\frac{K^2}{4J}(\mathbf{S}_1 + \mathbf{S}_2)^2 \end{aligned} \tag{3.5}$$

after replacing $E_1^{(i)} = J$ for all i and taking $\mathbf{S}_1 + \mathbf{S}_2$ as the quantization axis, allowed since both spins remain fixed in the process. Thus, to second order in perturbation theory, the ground state energy of spins 1 – 4 is given by the expression below, where we have defined $\tilde{K} = K - \frac{K^2}{2J}$,

$$\begin{aligned} E &= E_0 + \frac{K}{2}(\mathbf{S}_1 + \mathbf{S}_2)^2 - \frac{K^2}{4J}(\mathbf{S}_1 + \mathbf{S}_2)^2 \\ &= \frac{1}{2}(K - \frac{K^2}{2J})(\mathbf{S}_1 + \mathbf{S}_2)^2 \\ &= \frac{\tilde{K}}{2}(\mathbf{S}_1 + \mathbf{S}_2)^2. \end{aligned} \tag{3.6}$$

Upon comparison of Eqs. (3.3) and (3.6), one observes two things in the energy correction: (i) there is no dependence on $\mathbf{S}_3$, indicating a successful separation of the chains; (ii) the coupling of $\mathbf{S}_1$ and $\mathbf{S}_2$ has been renormalized from K to $\tilde{K}$, which manifests a weakening

of the bottom bond whenever the middle spin is in a dimer. This is the situation for the majority of the bottom bonds. On the other hand, we see in Fig. 3.3(b) that whenever the middle spin is free, the corresponding bottom triangle remains unchanged from its original configuration. We describe this by saying that the antikink in the top has produced a *ghost* at the bottom. According to the discussion presented earlier about B kinks, we note that these too produce ghosts. The final outcome of this perturbative analysis is depicted in Fig. 3.3(c), where the bottom chain has been effectively reduced to a renormalized Heisenberg chain with an indeterminate number of "defects", the ghosts. It is this renormalized chain which we analyze next in order to get a more complete understanding of our system, in particular about the ghost-mediated interactions between the domain walls.

3.3 Methodology

Most of the results presented in this chapter were numerically obtained with the use of Algorithms and Libraries for Physics Simulations (ALPS) [10]. At this point we would like to thank Matthias Troyer, one of the creators of ALPS, for his helpful insights in this aspect of our calculations. ALPS is an open source software providing readily-available simulation codes for calculations of strongly correlated systems. The type we carried out with ALPS were Density Matrix Renormalization Group (DMRG) [96] calculations given the quasi one-dimensional nature of our systems. Prior to performing the energy computations, we first prepared our systems by defining the appropriate lattices and setting the corresponding parameters. We then submitted them for calculation in ALPS. In order to minimize the execution time, we specified the ground state sector according to the number of spins, thereby reducing the size of the Hilbert space. Results were not altered by this constraint. The calculations were partly performed remotely from computers at Caltech and the California Nanosystems Institute (CNSI) at UC Santa

Barbara. Other calculations, such as those regarding the qualitative effects of interactions, were done using Mathematica.

3.4 Self-energy calculations of the kinks, antikinks, and their ghosts

3.4.1 Energy of a single defect

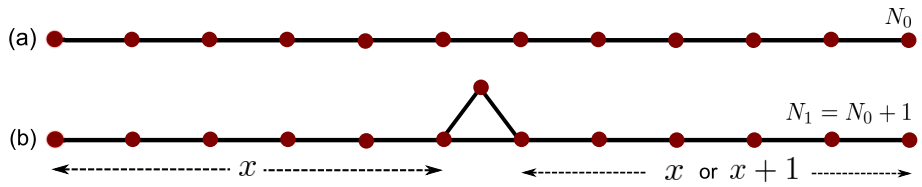


Figure 3.4: (a) A Heisenberg chain with N_0 spins in a chain of length $L = N_0 - 1$. (b) One defect is added to the bare chain at the middle or displaced toward one side depending on the parity of L. (a) and (b) are used to calculate the energy cost/gain ($\Delta\epsilon$) of introducing a single ghost.

In section 4.2, we saw how the lower portion of the ladder was reduced to a renormalized Heisenberg chain with a number of ghosts. In this part of our calculations, we begin by determining the energy cost/gain, $\Delta\epsilon$, of introducing a single one of these ghosts.[3] The ghost is added to the bare Heisenberg chain (Fig. 3.4(a)) of length L and $N_0 = L + 1$ spins. Introducing a defect constitutes adding one more spin, as shown in Fig. 3.4(b). For this calculation, we place the ghost in the middle, or shifted one unit to one side if the parity of L does not allow it. The distance from either edge of the chain is x (or x and $x + 1$). As the bond strength in the defect can assume any value $0 < K < J$, we proceed by determining the dependence of $\Delta\epsilon$ on K. We remind the reader that, choosing a particular value of K automatically determines the value of $\tilde{K}$ in the bonds of the lower chain.

To calculate $\Delta\epsilon$ we need E_1, the ground state energy of the chain with the defect

[3] Since ghosts correspond to the defects in the lower chain, we might at times refer to them as "defects". It will be clear from the context whether we speak of defects in the upper or the lower chain of the ladder.

(Fig. 3.4(b)), and E_0, the energy of the bare chain, both related through $E_1 = E_0 + \Delta\epsilon$. Obtaining what we need inevitably gives $\Delta\epsilon(K, L)$, that is, an unwanted dependence on L. We remove this dependence by performing a scaling analysis as we explain next. For a fixed value of K (or K/J), we calculate E_1 for various chain lengths L, as well as the corresponding E_0. Once we subtract these to obtain $\Delta\epsilon$, we plot the latter versus L^{-1} in order to extract the vertical intercept, which represents the L-independent value of $\Delta\epsilon(K/J)$. In reality, despite the fact that we are considering relatively large systems, the system is still not exempt from small-size effects. This is reflected in the separation of the data (in $\Delta\epsilon(K/J)$ vs L^{-1}) according to the parity of L, and then also depending on whether the x's (see Fig. 3.4(b)) are both even or both odd. In any case, the individual fits performed all converge, within some small error, to the same value. We take the average as the *true* intercept. We also take the difference in the intercept values, which happens to be greater than the individual standard errors of each vertical intercept, as the uncertainty in each data point. This procedure is repeated for each K/J so that at the end one has an ideally L-independent $\Delta\epsilon(K/J)$. A plot of this is given in Fig. 3.5 where $\Delta\epsilon$ is given in units of J. The uncertainties obtained are very small to be detected in the scales shown. A fit of the data yields the following expression,

$$\frac{\Delta\epsilon(K/J)}{J} = -0.20603\left(\frac{K}{J}\right)^2 - 0.30505\frac{K}{J} - 0.00146. \tag{3.7}$$

From Eq. (3.7) and Fig. 3.5 we make the important observation that $\Delta\epsilon$ is negative in the whole region of K/J. This $\Delta\epsilon$, which can be interpreted as the chemical potential of the ghosts, indicates that ghosts always represent an energy gain for the system, more specifically, to the lower part of the system.

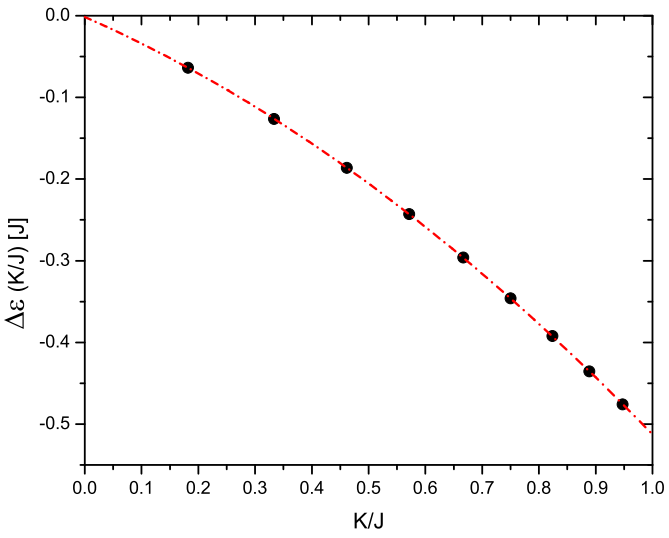


Figure 3.5: A plot of $\Delta\epsilon(K/J)$, measured in units of J. $\Delta\epsilon(K/J)$ can be interpreted as the chemical potential of ghosts. From $\Delta\epsilon(K/J) < 0$ for all K/J, one observes that ghosts are always beneficial to the system in the lower chain.

3.4.2 Proliferation of domain walls

The fact that $\Delta\epsilon$ is negative doesn't mean ghosts will instantaneously begin to populate the ladder. To determine whether, and if true when, this will occur, one needs to contemplate the system as a whole: kinks, antikinks and their ghosts. Figure 3.6 illustrates this. As was mentioned before, the diamondback ladder hosts two types of kinks, type A and type B. Although both energy costless, type B kinks are favored by the system since these produce a ghost with energy $\Delta\epsilon < 0$. The chemical potential of the kinks is then given by $\mu_{\text{kinks}} = 0 + \Delta\epsilon = \Delta\epsilon$. In terms of the antikinks, the price paid for them depends on their location. Their chemical potential is $\mu_{\text{antikinks}} = 3J/4 + \Delta\epsilon$. The $3J/4$ is the cost of the antikink and $\Delta\epsilon$ the energy gain of its ghost. We recall that antikinks are only created simultaneously in pairs with kinks. Hence, we consider the chemical potential of the pair, μ_{pair}, as the indicator of kink-antikink formation

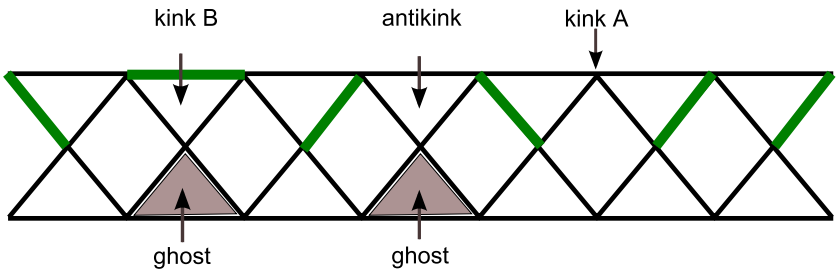


Figure 3.6: In the diamondback ladder, two types of kinks occur, both costless. Type B is preferred over type A since it produces a ghost, which is energetically beneficial. Antikinks (in the upper chain) are costly, but their image, the ghosts, always generate an energy gain in the system.

in the system. We plot

$$\mu_{\text{pair}}(K/J) = \frac{3}{4}J + 2\Delta\epsilon(K/J) \tag{3.8}$$

in Fig. 3.7. The most evident and, at the same time, most significant feature of this plot is the

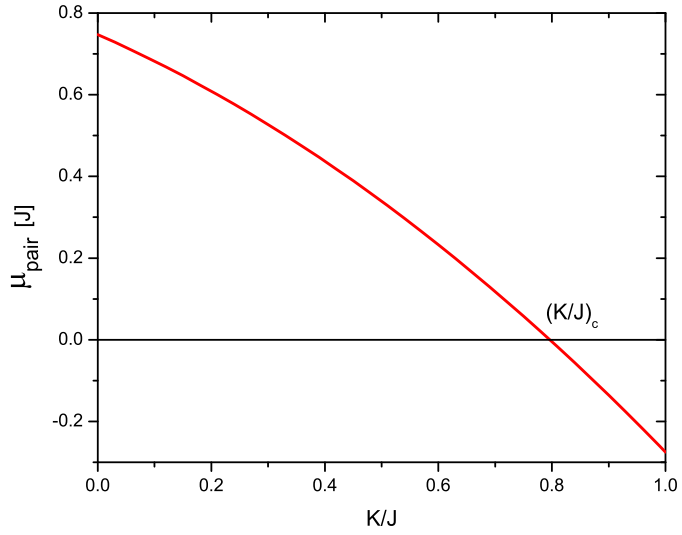


Figure 3.7: A plot of μ_{pair}, the chemical potential of kinks and antikinks. The presence of the critical point, $(K/J)_{\text{c}} \approx 0.8$, indicates the proliferation of domain walls (kinks and antikinks) as these become energetically beneficial to the system. Above this point, due to their increased numbers, the domain walls' interactions become very strong.

crossing of μ_{pair} from positive to negative values at $(K/J)_{\text{c}} \approx 0.8$, indicating a change in the system. Below this critical point, antikinks are found in dilute amounts and considering them, as Ref. [29] did, as non-interacting particles is likely a good approximation. Above, antikinks become energetically profitable for the system and domain walls begin to proliferate. As a result of this increase in number, their interactions become correspondingly stronger. As we stated at the beginning, this phase cannot be treated using our perturbative description.

3.5 Ghost-mediated domain wall interactions

So far, we have established that excitation interactions must be considered in the diamondback ladder since excitations do become significantly numerous in the system. Moreover, we have learned that not only antikinks interact, but kinks do as well via the ghosts that they produce. Thus, in the present section our objective is to investigate the ghost-mediated domain wall interactions. We first consider two-body interactions, that is, the case of the Heisenberg chain with two defects (ghosts). Here we will find this interaction potential to depend on the distance between the defects due to the critical nature of the Heisenberg chain. This dependence is essentially a reflection of a Casimir-like effect. After this numerical calculation, we will study the interaction effects from a qualitative perspective.

3.5.1 Two-body domain wall interactions

Fig. 3.8 depicts the scenario of two interacting ghosts. These are placed a distance s from each other as measured from their centers (Fig. 3.8(c)). The energy of the chain with the two defects is $E_2 = E_0 + 2\Delta\epsilon + U$, where the new variable U denotes the two-body interaction potential. From the definition of E_1 given previously, a little algebra gives $U = E_2 - 2E_1 + E_0$. As illustrated in Fig. 3.8(b), when calculating E_1, this time we put the single defect at a location

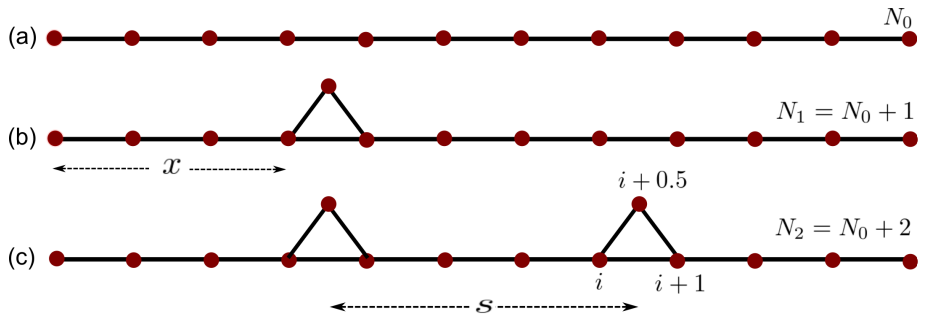


Figure 3.8: To obtain the two-body domain wall interaction potential, U, we calculate the total energy $E_2 = E_0 + 2\Delta\epsilon + U$ (c) of the system consisting of the Heisenberg chain plus two ghosts separated by a distance s. U is given by $U = E_2 - 2E_1 + E_0$, where E_1 is determined from (b), and E_0 is as before (a). Notice that the location of the single ghost in (b) corresponds to the position of the left ghost in (c), which is done in an attempt to cancel end effects.

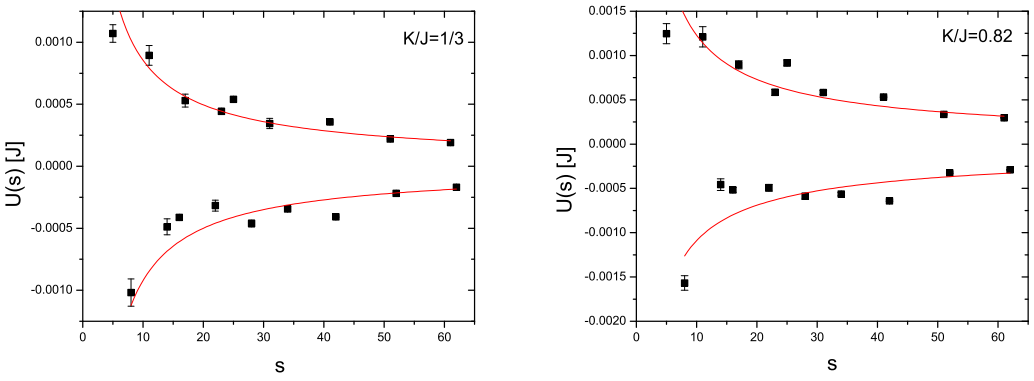
corresponding to one of the defects in the two-ghosts chain, not in the middle. We do this in order to minimize end effects. In the U data that we get, we again note a strong, undesired, dependence on the parameter x, in particular on its parity. Then, just as in section 3.4, we employ scaling analysis to remove it. Keeping s fixed this time, we plot U versus x^{-1} and obtain the vertical intercept $U(1/x \to 0)$. By letting $x \to \infty$, we ensure that end effects will be eliminated, or at least minimized. Also, although two separate fits corresponding to x odd and x even, respectively, have to be made, we enforce that they cross the vertical axis at exactly the same point, as it should not matter with what parity x approaches this limit. We implement this constraint by fitting the data to an expression of the form $U(x) = a/x + (-1)^x b/x + c$, where c is the value that we are after. The slope $a + b$ and the intercept c are obtained by fitting the x-even portion of the data. With c fixed, the x-odd portion is then fit, yielding $a - b$, and fully determining the fitting function. This is the procedure we follow to calculate each U for a given s. To compute its standard error, we apply the expression given below, where n is the number

of points used to calculate $U(s)$ and U_{orig} are the original calculated values,

$$\Delta U = \sqrt{\frac{\sum_{i=1}^{n}(U_{\text{orig}} - U_{\text{fit}})^2}{n-2}}. \tag{3.9}$$

Figure 3.9 gives a plot of $U(s)$ for two different values of K/J. Here we want to discuss the dependence of U on the coupling constants K and $\tilde{K}$ given in terms of J. Although physically $\tilde{K} = \tilde{K}(K, J) < K$, for the argument's sake, in the following we treat K and $\tilde{K}$ as independent parameters. The first observation we make is that $U(s)$ is independent of K, except at small s. This slight dependence at close separations has a physical explanation, relying principally on the strength of K. The explanation is that the latter determines the type of dimer patterns that can be accommodated within the segment between the defects. For instance, if $K > \tilde{K}$, a dimer will form in some bond of the defect; depending on its exact placement, another dimer might or might not form in the chain segment including the site connecting it to the defect. If $K < \tilde{K}$, then this site in question is certainly in a dimer. The essential issue here is that these effects, which determine the effective distance between the ghosts, are significant only when they are placed near each other. When far, these considerations do not arise. In contrast, we find that $U(s)$ does depend on $\tilde{K}$, a dependence that is reasonable and expected, as $\tilde{K}$ is the coupling constant in the bonds mediating the interactions. This, as well as the fact that U depends only on the separation (s) of the defects is the expression of a Casimir-like effect which gives rise due to our "imposition" of the defects on the chain.

There are some other features to be discussed in relation to Fig. 3.9. One is the oscillatory behavior of U as a function of s, which results in the separation of the data points into two branches according to the parity of s. The lower branch corresponds to an attractive potential for s even, and the upper branch to a repulsive potential for s odd. From this we gather that domain walls favor concentrating at small, even distances from each other. The other salient characteristic of $U(s)$ is the decay with increasing s, although conspicuously non monotonic.



(a) (b)

Figure 3.9: The two-body domain wall interaction potential as a function of separation, s; (a) K/J=1/3; (b) K/J=0.82. $U(s)$ is attractive for s even and repulsive for s odd. Solid lines represent the fits to the data obeying a power law $\sim 1/s^p$. See the text for a discussion of the exponent p.

To investigate the strength of the decay, we fit[4] the data to a power law of the form a/s^b, yielding the expressions below. Through these results, we are able to extract the order of magnitude for the ghost-mediated domain wall interactions.

$$\begin{aligned} U(K/J = 0.33, s) &\approx \frac{-0.0070}{s^{0.8822}} \quad s \quad \text{even} \\ &\approx \frac{0.0052}{s^{0.7876}} \quad s \quad \text{odd} \end{aligned} \tag{3.10}$$

$$\begin{aligned} U(K/J = 0.82, s) &\approx \frac{-0.0050}{s^{0.6593}} \quad s \quad \text{even} \\ &\approx \frac{0.0069}{s^{0.7519}} \quad s \quad \text{odd} \end{aligned} \tag{3.11}$$

Although there is an apparent difference in the powers of the two branches (it is unclear to us why this is the case), our main concern is that the decay is moderately weak with an exponent smaller than one. The significance or relevance of a power equal to one arises from results

[4] Although we considered several factors as potentially influential in the attainment of a "good" fit, we found none that we could control that would improve the convergence of the data.

of previous studies [40, 74] which have looked at interacting impurities in a one-dimensional Heisenberg chain. These studies have found the decay in U to go as $1/s$. Although our "impurities", the ghosts, have a somewhat extended nature, we can still relate to their findings, in some ways. For instance, they do find the same oscillatory behavior we observe. Also, in Ref. [74], the authors determine that attaining a $1/s$ power law requires very large impurity separations, something in the order of thousands. From Fig. 3.9, it is obvious that we have not considered such big distances, so expecting to get an exponent of one, based on the findings of [74], is impossible. However, when considering separations similar to ours, the effective exponent cited is comparable to those in Eqs. (3.10) and (3.11). One valid argument we can make to justify the weak decay we find is the following. Based on our previous observations, ghosts optimize their interaction energy when separated by short (even) distances. Thus, calculating U for relatively small s as we have is not inconsistent with this picture, making the calculations for bigger s unnecessary.

Here, we address the Casimir-like effect we mentioned above from a qualitative perspective. We have already observed that the interaction U is solely dependent on the separation of the ghosts, our "impurities"; this is demonstrated by the power law's only dependence on no other variable but s. Previously, we discussed the role of K in determining the effective length between the defects. Here, we take the aforementioned cases to the extreme, namely $K \gg \tilde{K}$ and $K \ll \tilde{K}$. The consequence of having a chain with defects in either of these situations is to effectively cut the chain into (3) parts. The middle, relevant segment is an interaction-mediating Heisenberg chain of length s. In other words, it is a finite-size Heisenberg chain which ultimately decides interaction effects. Finite-sized Heisenberg chains are well studied and are known [3, 8] to have size-dependent correction terms. One is a term $\mathcal{O}(1/s)$ whose origin is precisely the Casimir effect described. However, there are also logarithmic corrections $\mathcal{O}(1/s \ln s)$ which converge very slowly. We believe that it is these latter corrections which

are affecting the convergence of our data. However, addressing them in a controlled manner is beyond our capabilities.

3.5.2 Qualitative effects of interactions on the non-interacting wave function

Significant information was gathered from the numerical calculations in the previous sections. Although we learned about the tendency of ghosts – consequently of domain walls – to aggregate once they start to proliferate in the lattice, we still lack a complete picture of their ultimate arrangement. As we try to fill in this gap, in this section we analyze the effects of interactions from a qualitative perspective. In particular, we start from the pure, non-interacting case, and gradually turn on the interactions, observing how the non-interacting wave function is altered. Two situations are considered.

The first case we study is that of an antikink constrained to move between two kinks. To put it in more familiar terms, our antikink is a particle moving in a one-dimensional box whose walls are represented by the kinks. Note in Fig.3.10 that we have chosen kinks of type B for their energetic benefits to the system. We denote the distances from the antikink to the "walls" by s_1 and s_2, respectively, reminding the reader that, for this choice of kink, the location of the latter corresponds to the same location for the ghost in the other chain (of the ladder). We also define $R = s_1 + s_2$ as the width of the box. For the present purposes, we will assume an

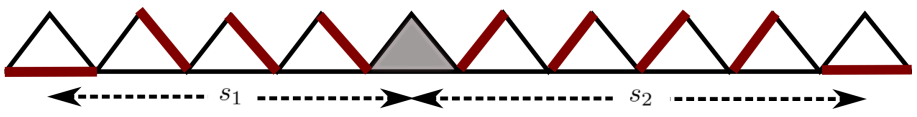


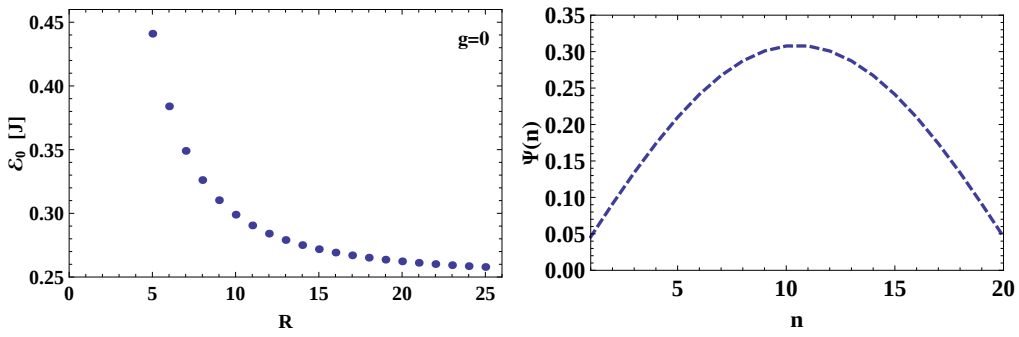
Figure 3.10: An antikink (shaded triangle) moving in a "1D-box", with the "walls" represented by the kinks (extreme triangles). These kinks (type B as opposed to type A) are energetically beneficial for the system, as they produced a ghost at a corresponding location in the other chain of the ladder. The antikink interacts with these ghosts. The width of the box is given by $R = s_1 + s_2$.

interaction potential of the form $U(s) = (-1)^{s+1}/s$, the sign being in accord with our findings. Hence, the total potential energy of the antikink is

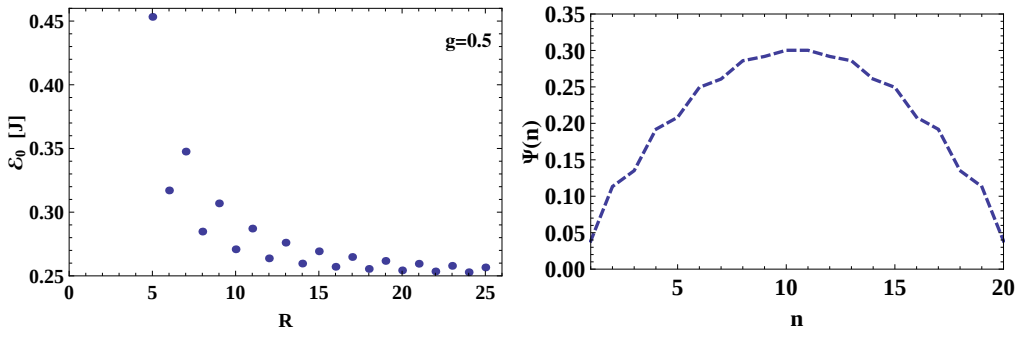
$$U_{total} = g\left[\frac{(-1)^{s_1+1}}{s_1} + \frac{(-1)^{s_2+1}}{s_2}\right] \tag{3.12}$$

where g, measured in units of the exchange coupling J, represents the strength of the interaction. This is our variable parameter. The kinetic energy is the antikink's tight binding Hamiltonian derived in Ref. [29] and given in Eq. (3.13), where n indicates the position – triangle of occupancy – of the antikink. Observe that, according to Fig. 3.10, i.e. to the way we have defined distances, n ranges from 1 to $R-1$, going from left to right.

$$H|n\rangle = \frac{5J}{4}|n\rangle - \frac{J}{2}\left[|n-1\rangle + |n+1\rangle\right] \tag{3.13}$$



(a) (b)



(c) (d)

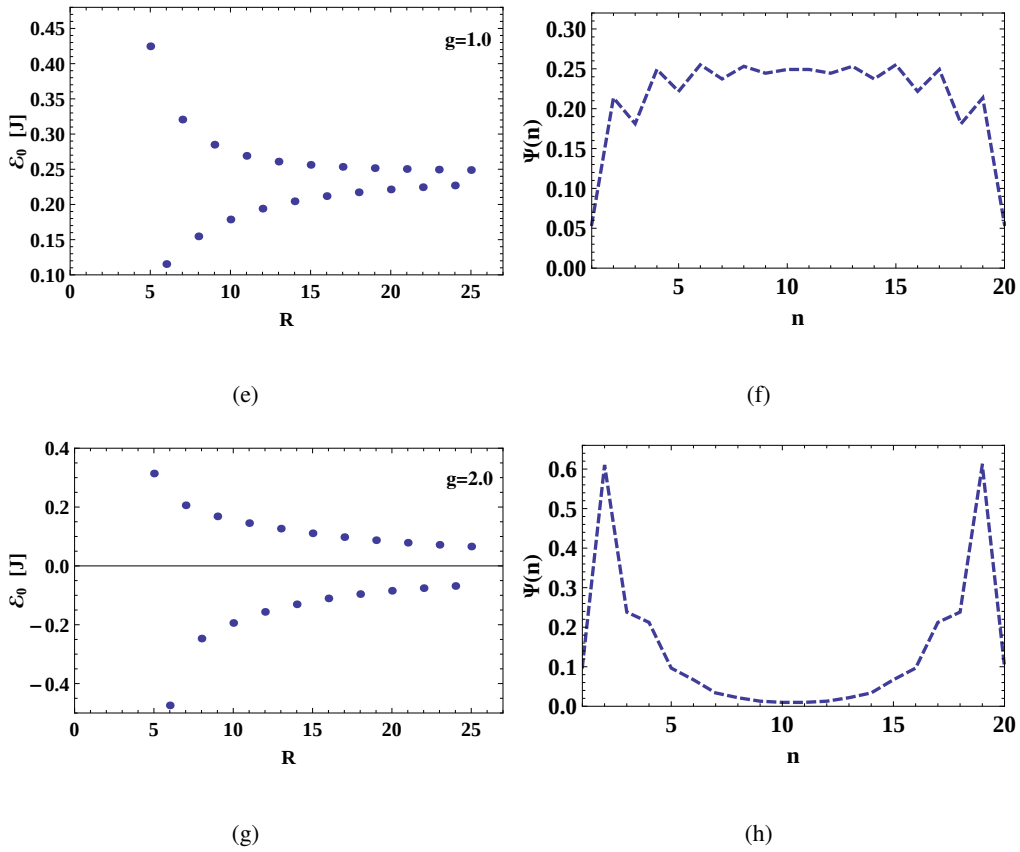


Figure 3.11: Ground state energy and wave function ($R = 21$) of an antikink constrained to move between two kinks, as in a particle-in-a-box problem. Strength of interaction, consecutive per row: $g = 0, 0.5, 1.0, 2.0$. See the text for a discussion of the plots.

In Fig. 3.11 we show a progression of both the ground state energy ($\mathcal{E}_0$(R)) and the wave function ($\Psi(n)$) as g is increased from zero. Figs. 3.11(a-b) depict the case $g = 0$. From this we observe an asymptotic behavior of $\mathcal{E}_0$ towards $J/4$, in agreement with Ref. [29]: as R tends to infinity, the antikink effectively becomes free, i.e. non-interacting. The corresponding $\Psi(n)$ is given for $R = 21$ (as is for the rest of the cases), where we see the all-familiar ground state wave function which is maximized at the center. From the point of view of the moving antikink, it is the middle position which allows for maximum delocalization. In the following figures, we show the results for $g = 0.5$ (c-d); $g = 1.0$ (e-f); $g = 2.0$ (g-h). By looking at the energy column, one sees how $\mathcal{E}_0$ gradually acquires the oscillatory behavior that we already

observed in $U(s)$. Similarly, from the column of $\Psi(n)$, we notice how the successive increments in g translate into a steady, to complete, reversal. We note, however, the presence of a critical $g_c \sim 1$ where the concavity of the middle of the wave function changes from down to up, indicating the point at which interactions start to dominate the motion of the antikink, as opposed to the kinetic energy. When the strength of g is large, we see how the antikink goes from favoring a central location to preferring a position close to either kink (or ghost, equivalently). For a kink-to-kink distance of $R = 21$, these locations correspond to $n = 2$ and $n = 19$, which locate the antikink 2 units away from either kink, as should be the case.

The second situation we consider is the interaction between two antikinks, as illustrated in Fig. 3.12. Of course, this necessarily means having a kink between the two, since antikinks cannot move past these. The immediate thought should be putting a B kink due to its energetic benefits. However, one must recall that this type of kink produces a ghost in the other chain, so placing this kink would result in additional interactions, which is not relevant to the situation at hand: studying the interaction between the two shown antikinks only. Thus, we place a kink of type A, which does not create any extra sources of interaction. At the extremes, we can, and do place type B kinks. Each antikink is confined to move within the region of the middle kink and its respective outer kink (Fig. 3.12). In the process, each can delocalize to any of the R (assumed the same for both) locations, i.e. triangles, within its range. We denote this location – counted from left to right – by n_i, where $i = 1, 2$ for the left and right antikinks, respectively. The distances from the center kink to the antikinks are s_1 and s_2, respectively, which relate to the n_i as $s_1 = R - n_1 + 0.5$ and $s_2 = n_2 - 0.5$. Hence, the antikinks' separation is $s = s_1 + s_2 = R - n_1 + n_2$, so that their interaction potential energy is given by

$$U(s) = g\frac{(-1)^{s+1}}{s}, \tag{3.14}$$

assuming the same exponent as before. The kinetic energy of each antikink is again given by

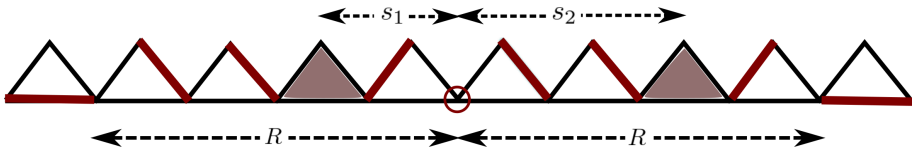


Figure 3.12: Two interacting antikinks (shaded triangles), each confined by their respective kinks to a region of length R. A type-A kink is chosen for the middle kink in order to avoid interaction of the antikinks with the ghost that a type-B kink would produce. The antikinks are separated by a distance $s = s_1 + s_2$, which determines their potential energy, Eq. (3.14). Each has kinetic energy as given in Eq. (3.13), where n_i takes the integer values from 1 to R.

Eq. (3.13).

The method is the same: vary the strength factor g and observe. This time, we have presented the probability density function of the ground state, $|\Psi|^2$, as it is easier to visualize than Ψ itself. By looking at the locations of maximum probability (density), we can infer the antikinks' configuration corresponding to a particular g, hence deducing their tendency of motion as interactions become stronger. But first, we explain some notation. From the definitions given previously, the antikink pair location is given by $\{n_1, n_2\}$ and the size of the Hilbert space for the two-antikinks system is R^2. We will index the wave functions as $\Psi(j)$ ($j \in [1, R^2] \cap \mathbb{N}$) according to $j = (n_1 - 1)R + n_2$. This means, for example, that $j = 1$ corresponds to $\{1, 1\}$; $j = 2$ corresponds to $\{1, 2\}$, ... and $j = R^2$ corresponds to $\{R, R\}$. Fig. 3.13 gives the plots of $|\Psi(j)|^2$ for $R = 15$ and various values of g. The first panel (3.13(a)) shows the probability density at $g = 0$. In this non-interacting case, $|\Psi(j)|^2$ is maximized at $j = 113$, corresponding to the state $\{8, 8\}$ in which both antikinks are situated exactly at the center of their allowed range. In other words, with no interactions present, the picture is just that of two particles in a box next to each other. Fig. 3.13(b) is there to illustrate how the antikinks begin to move as the interaction is increased: when $g = 4.8$, the maximum is at $j = 156$ with position $\{11, 6\}$,

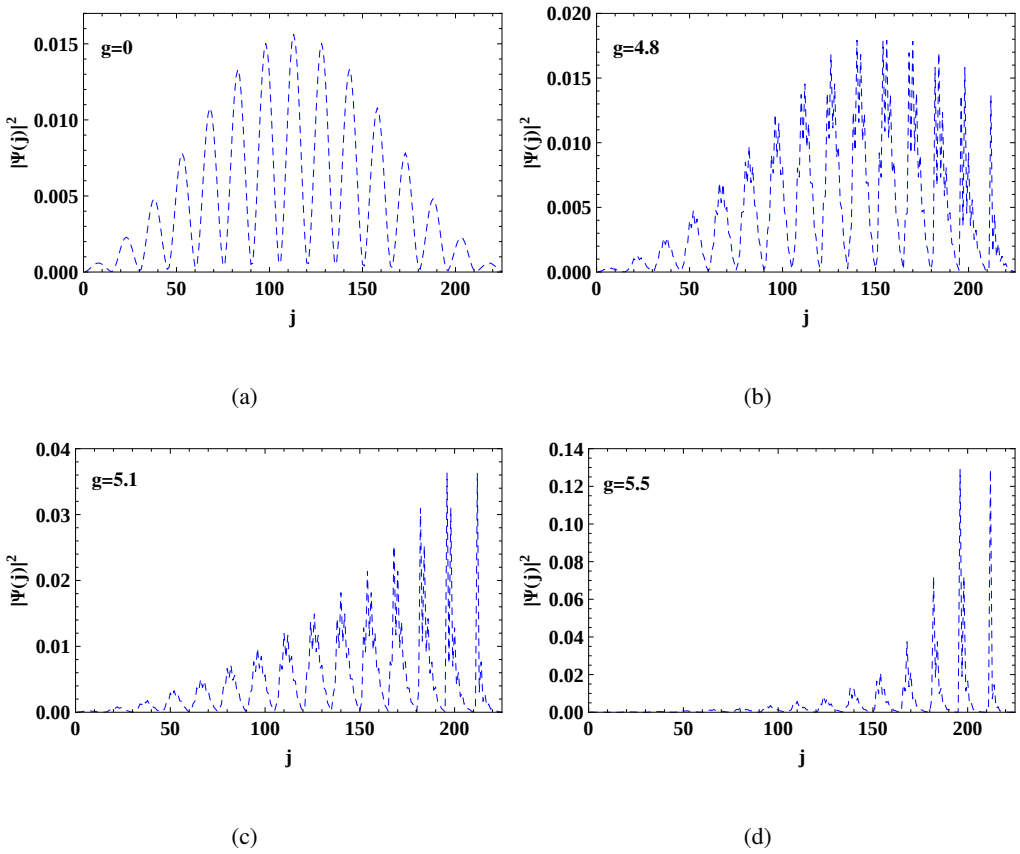


Figure 3.13: Probability density functions of the two-antikinks system plotted as a function of j, where j is any of the R^2 possible configurations, $\{n_1, n_2\}$, for the antikinks. Each plot is for a different value of the interaction strength g, as indicated. See the text for more details.

indicating motion of the antikinks towards each other. By the time $g = 5.1$ (3.13(c)), the antikinks are already at their position of maximum approach, $\{14, 1\}$ and $\{15, 2\}$ ($j = 196$ and $j = 212$, resp.). Further increment of g only serves to emphasize the latter situation as the ground states remain the same, but their probabilities become much larger (3.13(c)). There are two additional comments we would like to make in regards to this second case. One is a cautionary note about the oscillations in $|\Psi(j)|^2$: these are not physical; they are merely an artifact of the non-monotonic mapping between $\{n_1, n_2\}$ and j. The second point is that, unlike the case of the single antikink, in this case it is not as obvious to determine a critical strength of g.

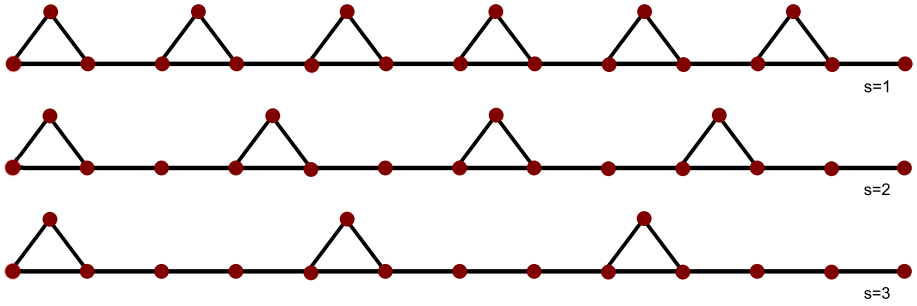


Figure 3.14: Chains with multiple defects arranged periodically at separations $s = 1$, $s = 2$ and $s = 3$, respectively. The cases $s = 4, 5, 6$ are also examined. These are considered in the study of many-body domain wall interactions.

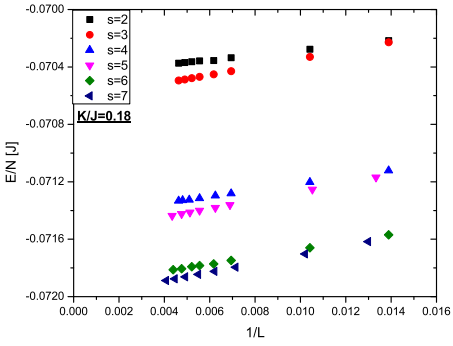
Being able to detect a change of concavity is not as direct as in the previous case. Nevertheless, the tendency of the system with increasing g is the same as before, namely, the preference of antikinks to be close together.

3.5.3 Many-body domain wall interactions

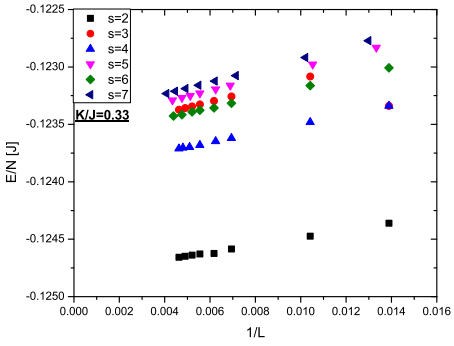
Thus far, we have looked at two-body interactions only but, based on the fact that in the diamondback ladder antikinks are found in finite concentrations, higher-order interactions among the domain walls are present as well. The ultimate objective of this study would be determining the ground state of our model in the presence of the excitations. In this section, we start digging in this direction by asking ourselves what happens when not two, but multiple defects are found in the system. We do this, just as we did before, from the point of view of the renormalized chain with the ghosts. To this end, we calculate the ground state energy of the chain with a periodic arrangement of defects. The cases we consider are chains with defects mutually separated by $s = 1, 2, 3, 4, 5, 6$. A partial illustration of these situations is given in Fig. 3.14. We denote the energy of these systems by E, expressed as $E = E_0 + N_\triangle \Delta\epsilon + W$, where $N_\triangle$ is the number of defects (ghosts) in the chain and W is the total, many-

body, interaction potential. Although similar chain lengths have been selected for the various cases, they are not exactly the same due to different unit sizes, but since we are interested in knowing which defect configuration is the least energetic, we need to implement some type of normalization. We choose to normalize E by dividing it by the the number of sites $N = N_0 + N_\triangle = \frac{N_0(s+2)-1}{s+1}$ in order to yield the energy per spin in each case. Recall that N_0 is the number of sites in the bare chain.

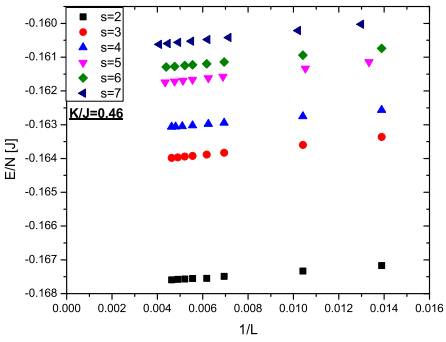
We present the results of this calculation in Fig. 3.15, where we plot E/N vs L^{-1} for various values of K/J. Notice that we are again plotting the data versus L^{-1} rather than L in order to extrapolate to the thermodynamic limit, our limit of interest. The overall observation we make in all plots is the linear behavior, indicating the convergence of the data as $L \to \infty$. At the smallest value $K/J = 0.18$ (Fig.3.15(a)), we see that the most to least favorable configurations correspond, respectively, to $s = 7$, $s = 6$, $s = 5$, ...$s = 2$. This appears to indicate that K is still not considerable enough to create any positive effect, meaning an energy gain, in the system. Thus, the fewer the defects the better. In Fig.3.15(a), $K/J = 0.33$, the separation is according to s parity: s-even configurations yield the lowest energy, while the s-odd the largest. Additionally, each set favors the arrangement with the densest defect distribution. Beyond this K/J value, incrementing this ratio correspondingly lowers the total energy, with one observation remaining constant: the more closely spaced the defects are, the more beneficial it results for the system, regardless of the parity of the separation.


s=2
s=3
s=4
s=5
s=6
s=7
K/J=0.18
E/N [J]
1/L

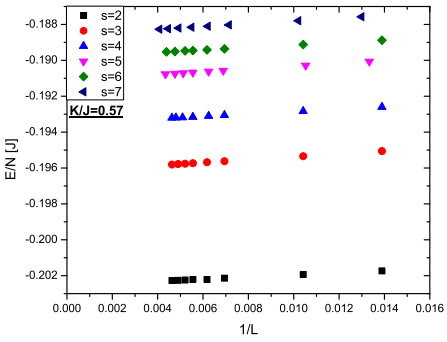
(a)


s=2
s=3
s=4
s=5
s=6
s=7
K/J=0.33
E/N [J]
1/L

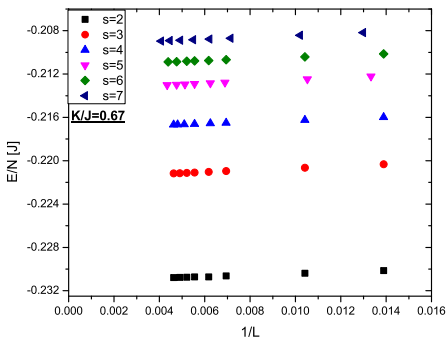
(b)


s=2
s=3
s=4
s=5
s=6
s=7
K/J=0.46
E/N [J]
1/L

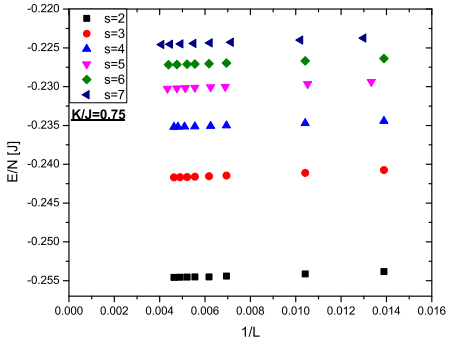
(c)


s=2
s=3
s=4
s=5
s=6
s=7
K/J=0.57
E/N [J]
1/L

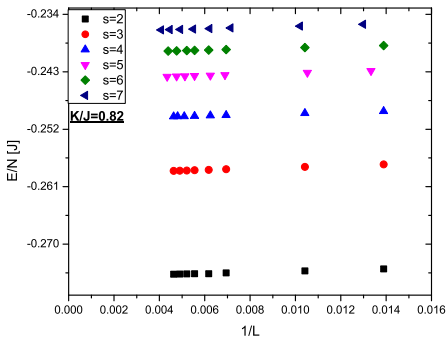
(d)


s=2
s=3
s=4
s=5
s=6
s=7
K/J=0.67
E/N [J]
1/L

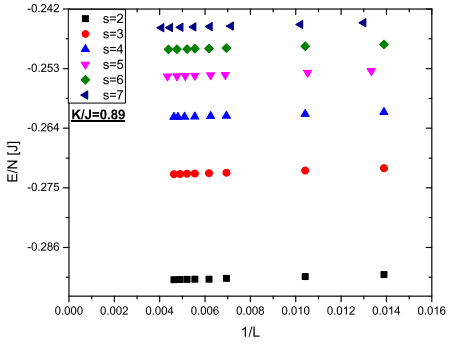
(e)


s=2
s=3
s=4
s=5
s=6
s=7
K/J=0.75
E/N [J]
1/L

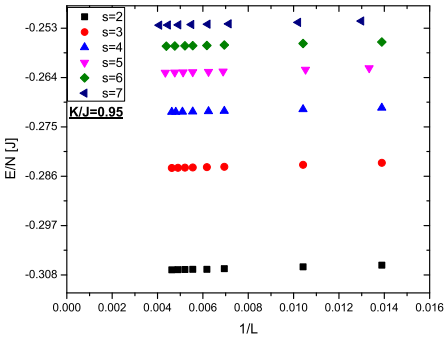
(f)


s=2
s=3
s=4
s=5
s=6
s=7
K/J=0.82
E/N [J]
1/L

(g)

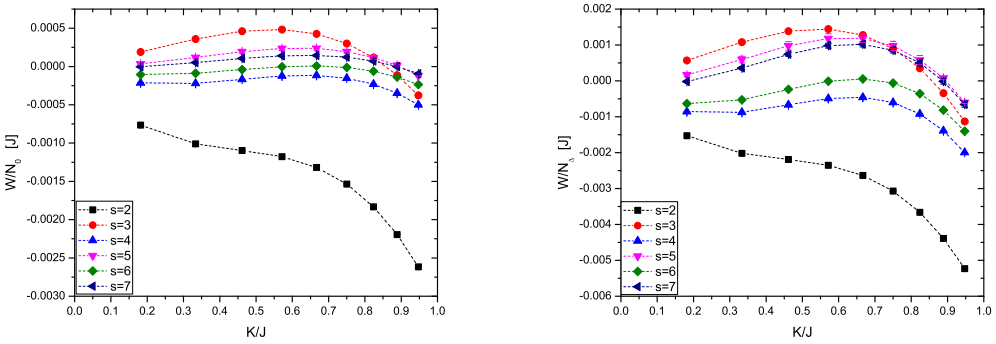

s=2
s=3
s=4
s=5
s=6
s=7
K/J=0.89
E/N [J]
1/L

(h)



(i)

Figure 3.15: E/N is the ground state energy per spin of the renormalized chain with multiple ($N_\triangle$) defects, where $N = N_0 + N_\triangle$. s is the separation between the defects, $L = N_0 - 1$ is the length of the chain, and K/J is the ratio of the coupling constants in the lower and upper chains of the ladder, respectively.



(a) (b)

Figure 3.16: The total, many-body, interaction potential as a function of K/J: (a) W/N_0 and (b) W/N_Δ. See the text for a discussion of the figures.

At this point, we are interested in finding out, if possible, any tendency of the domain walls towards some preferred arrangement. For that, we believe that W might be a useful tool. Hence, we calculate it from the E data using both $E = E_0 + N_{\triangle}\Delta\epsilon + W$ and Eq. (3.7). W, being different for each value of s, depends on both L and K, but our main concern is observing its progression with changing K/J. This means calculating $W(K/J)$ and eliminating the dependence on L. The procedure we utilize to do this is the same we employed for U. Thus, we refer the reader to section 3.5 for a reminder. The only additional fact we mention here is that, for a more meaningful result, we carried out the scaling analysis for W/N_{Δ} and W/N_0 instead of W alone. The corresponding plots are given in Fig. 3.16.

Figure 3.16(a) is a plot of $W/N_0(K/J)$, with each curve corresponding to a different s. There is a clear gap between the $s = 2$ curve, occurring at the lowest energies, and the rest. This places the $s = 2$ configuration as the most energetically favorable for the system in the whole region of K/J. The other curves remain more or less invariant and parallel to each other, with the exception of the $s = 3$ curve (initially at the upper extreme), which exhibits a rapid drop after $K/J \sim 0.7$, allowing it to overtake three other curves. At the end, the change is just enough to put it above the $s = 4$ curve. Overall, the division is again between the even and the odd, with the former being the arrangements of choice. And, just as it was observed in U, the total interaction potential is smaller in magnitude for the larger defect separations, as should be expected. In the next panel (Fig. 3.16(b)) we show $W/N_d(K/J)$. The behavior of this is very similar to the one just described. In this case, though, a gap opens up between the s-even curves and the s-odd curves. For this reason, the $s = 3$ curve is not able to reach as low as in W/N_0.

3.6 Conclusions

In this study we considered spin excitations in the diamondback ladder. These spin-1/2 quasiparticles are domain walls separating the ground states; as individual objects, one of them – the antikink – is energy costly given that it represents a local triangle not in its ground state; and the other, the kink, does not cost the system any energy. However, as we stated, kinks can only be created in pairs with antikinks. By means of perturbation theory, we were able to break the problem of the ladder into the study of its constituent upper and lower chains. Optimization of one chain led to the discovery that not only antikinks interact in the diamondback ladder (as was the case in the sawtooth chain), but kinks do as well, thanks to the ghosts that both objects produce in the other chain. From a study of these ghosts, we were able to establish an important fact: domain walls, i.e. antikinks and kinks, begin to proliferate in the system at a critical point $(K/J)_{\mathrm{c}} \approx 0.8$. According to the counting argument we gave about the defect concentration in the diamondback ladder (as well as in other corner-sharing lattices), this proliferation was not completely unexpected, but just when in our approximation this was to take place was our initial inquiry. As was pointed out, with our present formalism, the strong excitation interactions that ensue at and beyond this critical point cannot be treated. However, as a first treatment of these interactions we calculated the ghost-mediated two-body domain wall interaction potential, $U(s)$. According to our results, domain walls prefer a configuration where they appear mutually separated at even distances, an observation supported by studying W, the many-body interaction potential. Although a convincing conclusion, we are yet to know how this preference ultimately plays a role towards the achievement of a final arrangement. While our calculations were not able to provide us with this information, one thing we are convinced of is that interactions have an undeniable effect in the state of the system. As was presented in section 3.5.2, the non-interacting wave function definitely experiences a transformation when the interactions are

turned on, progressively changing into the wave function corresponding to the situation where domain walls are close to each other at even separations. Besides observing these changes, our qualitative "calculations" gave us an indication of how strong – with respect to the exchange coupling J – the interactions need to be in order to create the effect of domain wall aggregation.

Based on this observed domain walls' tendency of motion towards one another, we have the strong suspicion that the system will form some type of valence bond crystal. In order to determine whether this is indeed the case, one needs to consider not just the renormalized chain but the complete uniform ladder. Detecting how the presence of a particular valence bond has any influence in the formation of another (nearby) valence bond, requires calculating the four-spin correlation functions. On the other hand, one could also look into three-body interactions as a way of detecting this suspected crystal. These new approaches suggest themselves as future work on this project. We will pursue them in the near future. Finally, based on our calculational observations, it remains to be seen how big of a system one needs to consider in order to minimize as much as possible the size-dependent effects which affected the analysis of our data.

Chapter 4

A Spin-1 Kagomé Antiferromagnet

4.1 Introduction

One thing that was evident in Chapter 2 was the overwhelming number of studies that have been done on the spin-1/2 kagomé Heisenberg antiferromagnet (KHAF). This system is of enormous importance and relevance in the area of frustrated magnetism, and its intriguing features make it an interesting system to study. A natural question to ask is whether the intricacy of the $S = 1/2$ model persists in its $S = 1$ analogue. For example, does the system exhibit more classical features due to the larger spin value? Asking such questions is not fortuitous, as instances have occurred where the distinction between integer and half-odd integer values of the spin has been a determining factor. von Delft and Henley [90] encountered such an instance when calculating tunneling amplitudes between degenerate states of the KHAF, but this situation is also reminiscent of Haldane's [28] notable result that one-dimensional quantum chains with integer spin have a gap to the excited states, while half-odd integer chains do not.[1]

Independently of the spin-1/2 system, the $S = 1$ KHAF is deserving of investigation also. As will be noted below, there are experimental realizations of spin-1 kagomé antiferro-

[1] For a review of arguments leading up to this result see Refs. [3, 4].

magnets, so being able to understand their properties analytically is very useful in the context of 2D magnetism. Although the ultimate objective is to analytically extract knowledge about the spin-1 Heisenberg model, lacking the tools to tackle this problem directly, we consider an alternative means of arriving to that point. In this study, we propose an exactly soluble spin-1 model with an SU(2)-symmetric Hamiltonian which, among other terms, contains the nearest-neighbor Heisenberg interactions of interest. Starting with our spin-1 model, we perturbatively enhance the nearest-neighbor Heisenberg interactions by introducing an additional term of this type. The hope is that, in doing so, one can continuously connect to our original system of interest. But before we describe our model in more detail, in the remaining part of the introduction we give an overview of previous experimental and theoretical results on the spin-1 model, followed by a review of AKLT models which are of relevance to our investigation.

4.1.1 $\mathbf{S = 1}$ KHAF: experiment and theory

Remarkably, there exists a physical realization of the $S = 1$ KHAF. The synthesization of the organic material m-MPYNN· X·$(1/3)$(acetone) (X=BF_4, ClO_4) was effectuated by Agawa et al. [41] in 1994. 2D magnetic layers are composed of the radical cation m-MPYNN, of spin 1/2, and one third of X, the remaining two thirds acting as separation between them. The structure of each layer consists of m-MPYNN molecules existing as dimers as shown in Fig. 4.1. According to Ref. [41], there is a strong ferromagnetic intradimer interaction J_1 ($J_1/k_{\mathrm{B}} = -23.26 \pm 1.2$ K) which forms a triplet state between the constituent spins 1/2. The interdimer interaction, on the other hand, is weak and antiferromagnetic, $J_2/k_{\mathrm{B}} = 3.11 \pm 0.05$ K. Because of the strong ferromagnetic interactions in the dimers, the system can be effectively regarded as an $S = 1$ antiferromagnet on the kagomé lattice at temperatures sufficiently below J_1/k_{B}. A visualization of a layer is given in Fig. 4.1. Wada and company [91, 36] performed

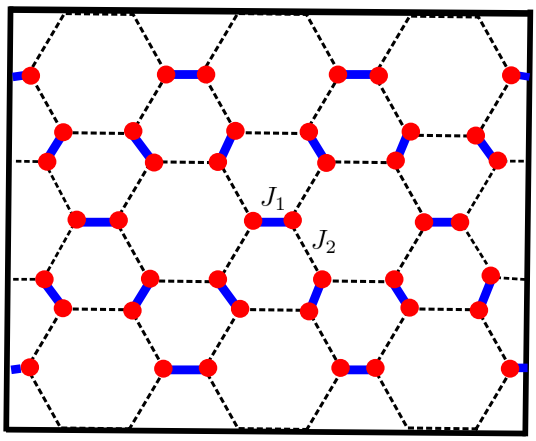


Figure 4.1: 2D layer of the organic compound m-MPYNN· X (X=BF_4, ClO_4). Red (solid) circles are m-MPYNN $S = 1/2$ molecules. The blue (dark) lines represent the dimers formed by the $S = 1/2$ molecules as they interact ferromagnetically (J_1) forming triplet states. The intradimer interaction is antiferromagnetic with coupling constant J_2. At low temperatures, the system can be effectively regarded as an $S = 1$ kagomé antiferromagnet.

experimental measurements of the material (X=BF_4 discussed here), finding very interesting features. For example, according to the magnetic susceptibility, the system has a spin gap and exhibits no sign of magnetic order down to mK temperatures. Also, based on the entropy obtained from the heat capacity measurements, there is an extensive number of nonmagnetic states below $T = 0.25K$, which are gapped too. As we will see, these features will be well captured by the model we present here. Similarly, studies of the $S = 1$ KHAF have also been done theoretically and numerically by Hida [32, 33], who proposed the hexagonal solid state as a caricature ground state for the system. We will discuss these and other relevant findings where appropriate in the context of our model.

4.1.2 AKLT models: Projective Hamiltonians

The model that we will be considering is a type of projective Hamiltonian that was originally introduced by Majumdar and Ghosh [48] for 1D spin-1/2 chains and was later gener-



Figure 4.2: In the AKLT model of an $S = 1$ quantum chain, a unique ground state is constructed by connecting two nearest-neighbor $S = 1/2$ spins (blue, dark circles) in a valence bond (brown, solid, line). Each site (yellow oval) consists of two symmetrized $S = 1/2$ spins. The state is known as a valence bond solid (VBS).

alized by Klein [44] for 2D lattices and by Affleck, Kennedy, Lieb and Tasaki [1, 2] for other values of spins. As these are specially pertinent to our discussion, here we give a description of the AKLT models, those introduced by the last people mentioned.

AKLT models get their names after Affleck, Kennedy, Lieb and Tasaki, who proposed them in 1987 [1]. The models have a unique ground state, named the valence bond solid (VBS) state, which has no broken symmetries. AKLT presented the VBS as an exact solution for the ground state of the $S = 1$ quantum spin chain. In this system, the VBS state is constructed by first assuming each $S = 1$ spin to consist of two $S = 1/2$ spins that have been symmetrized, and then by contracting two nearest-neighbor $S = 1/2$ spins into a singlet. As this is done, each site has two valence bonds emanating from it, leaving all symmetries unbroken. A pictorial representation of this description is given in Fig. 4.2.

In Ref. [1], AKLT also extended the notion of the VBS state to higher dimensions and higher spin values. In the general case, it is possible to find a model with a VBS ground state whenever $2S$ is a multiple n of the coordination number z, namely whenever $n = 2S/z$ is satisfied. With the premise that every site of spin S is effectively comprised of $2S$ spins 1/2, the ground state is obtained by having n valence bonds on each link. The corresponding model Hamiltonian consists of projection operators projecting out a total spin greater than $2S - n$ for every spin pair. However, since two of their (combined) effective constituents are in a valence bond, the projection is equal to zero. This serves as a proof that, indeed, VBS states are the

ground states. All this can be formally written. The AKLT model Hamiltonian is,

$$H_{\text{AKLT}} = \sum_{\langle ij \rangle} \sum_{S'=2S-n+1}^{2S} a_{S'} P_{S'}(\mathbf{S}_i + \mathbf{S}_j). \tag{4.1}$$

As just mentioned, the Hamiltonian consists of a sum of projection operators $P_{S'}$ onto total spin $S' > 2S - n$ of every pair of nearest-neighbor spins $\langle ij \rangle$; $a'_S > 0$. Concretely for the $S = 1$ spin chain, the Hamiltonian consists of a single projection operator onto $S = 2$. Since each site has an $S = 1/2$ spin coupled into a singlet with another one at a neighboring site (Fig. 4.2), the maximum total spin possible for the two sites is 1. Thus, the projection is zero and the VBS state is the ground state of (4.1).

Taking the route of an AKLT-like Hamiltonian as a solution to the spin-1 kagomé Heisenberg model stems from the fact that VBS states are good variational ground states of the Heisenberg Hamiltonian. For example, Ref. [1] discusses how in 1D chains the VBS state yields a lower expectation value energy for the Heisenberg part of the (AKLT) Hamiltonian when compared to either a dimerized state or a Néel state. They quote [67] an energy difference of only about 5% between this expectation and the real Heisenberg Hamiltonian. Similar conclusions have been made in 2D. Cai et al. [97] considered the Heisenberg model in the spin-1 fully frustrated square lattice, finding that the AKLT-like part of the Hamiltonian has degenerate ground states of two types, dimerized and VBS. However, they reported, the VBS states are selected and the degeneracy lifted when the remaining part of the Hamiltonian is added perturbatively.

4.2 The Model

4.2.1 The Hamiltonian

The SU(2)-symmetric parent Hamiltonian we propose is

$$H = I \sum_{\hat{\langle}} P^{(3)}\left(S_{\hat{\langle}}\right) = \frac{I}{720} \sum_{\hat{\langle}} \mathbf{S}^2_{\hat{\langle}} \left(\mathbf{S}^2_{\hat{\langle}} - 2\right) \left(\mathbf{S}^2_{\hat{\langle}} - 6\right). \tag{4.2}$$

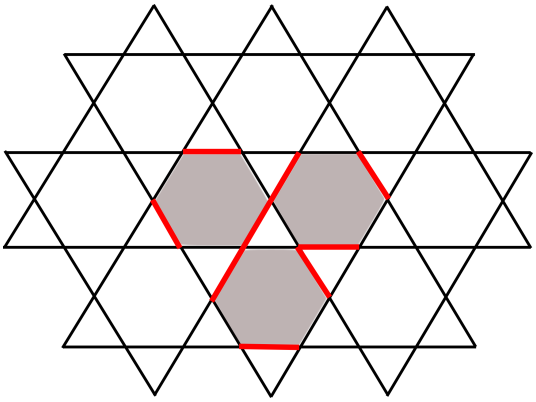


Figure 4.3: The sites of the kagomé lattice are occupied by $S = 1$ spins with interactions occurring between nearest and next-nearest neighbors around a hexagon. Shaded hexagons illustrate one of the many valence-bond (red line) configurations which are ground states of Hamiltonian (4.2).

The Hamiltonian is a sum of projection operators $P^{(3)}$ projecting out total spin 3 from each triad $\mathbf{S}_{\langle} = \mathbf{S}_1 + \mathbf{S}_2 + \mathbf{S}_3$ in the lattice. 1, 2, and 3 are consecutive sites taken around every hexagon, and $I > 0$ is a constant. Notice that despite its complicated form, the Hamiltonian involves only nearest and next-nearest neighbor interactions.

4.2.2 The ground states

We now turn to the discussion of the ground states of Hamiltonian (4.2). Since this Hamiltonian is a sum of projectors (with positive coefficients), any state annihilated by all of these projectors is automatically a ground state. Consider a state such as the one depicted for the three shaded hexagons in Fig. 4.3. The red lines represent the valence bonds, i.e., the spin singlets formed by the spin-1/2 constituents of the original $S = 1$ spins.[2] Note that each site participates in two valence bonds, each on adjacent hexagons. As in the original AKLT construction [1], the state is symmetrized with respect to these spin-1/2 constituents, projecting them on the total $S = 1$ spin state at each site. Note that this is a ground state since every projection operator in the Hamiltonian acting within the shaded hexagons annihilates this state:

[2]The nomenclature we use here follows the description given in section 4.1.2.

the placement of a valence bond in each spin triad reduces the maximum allowed value of $\mathbf{S}_\langle$ to 2. However, such a ground state is not unique; every hexagon can have two possible configurations of alternating valence bonds. We claim that while not orthogonal, these states form a complete basis of the ground state manifold. We address this in the following sections.

4.2.2.1 Schwinger boson representation

Before proceeding to prove these claims, we first give a more formal description of these ground states in terms of *Schwinger* bosons. In this formalism, each site i is populated by two species of bosons with corresponding creation operators $a_i^\dagger$ and $b_i^\dagger$. The spin-1 operators are then represented as follows:

$$S_i^+ = a_i^\dagger b_i, \quad S_i^- = b_i^\dagger a_i, \quad S_i^z = \frac{1}{2}\left(a_i^\dagger a_i - b_i^\dagger b_i\right), \tag{4.3}$$

subject to the additional constraint that $a_i^\dagger a_i + b_i^\dagger b_i = 2$. In this language, a valence bond between two sites is written as $\left(a_i^\dagger b_j^\dagger - b_i^\dagger a_j^\dagger\right)|\varnothing\rangle$, where $|\varnothing\rangle$ is the Schwinger boson vacuum. Numbering the corners of a hexagon from 1 to 6 clockwise, top left first, the two valence bond states possible for each hexagon are $|\sigma_h = 1\rangle = \left(a_1^\dagger b_2^\dagger - b_1^\dagger a_2^\dagger\right)\left(a_3^\dagger b_4^\dagger - b_3^\dagger a_4^\dagger\right)\left(a_5^\dagger b_6^\dagger - b_5^\dagger a_6^\dagger\right)|\varnothing\rangle$ and $|\sigma_h = -1\rangle = \left(a_2^\dagger b_3^\dagger - b_2^\dagger a_3^\dagger\right)\left(a_4^\dagger b_5^\dagger - b_4^\dagger a_5^\dagger\right)\left(a_6^\dagger b_1^\dagger - b_6^\dagger a_1^\dagger\right)|\varnothing\rangle$. Here, we have introduced the shorthand notation $|\sigma_h\rangle$, the (Ising) pseudospin, to denote the spin state of the hth hexagon: $\sigma_h = 1$, or "up" ($\sigma_h = -1$, or "down") if a valence bond is present on the top (bottom) horizontal edge of the hexagon.

The (unnormalized) ground states of Hamiltonian (4.2) can then be written as

$$\Psi_{\text{GS}} = \bigotimes_{h=1}^{N/3} |\sigma_h\rangle. \tag{4.4}$$

While indexing all hexagons in the kagomé lattice, we have assumed periodic boundary conditions. Then, since each hexagon contains six sites and each site is shared between two hexagons, there are $N/3$ hexagons in a lattice with N sites. Clearly, this gives $2^{N/3}$ ground states indexed

by their pseudospin variables. In what follows, a particular state of this ground state manifold will be denoted as $\Psi_{\rm GS}^{(m)}$.

4.2.2.2 Valence bond states basis

In this section we want to establish the validity of the valence bond states as a basis for the ground state manifold. For this, we need to prove that they are linearly independent. We demonstrate this by considering a single spin triad, namely a single term in the parent Hamiltonian (4.2). To ensure that an overcount of the states is not done, we verify that the number of linearly independent states we find for the triad exactly accounts for all the possible states.

As each spin-1 can be in any of the states with projections $S^z = 0, \pm 1$, there are a total of $3^3 = 27$ different states for the three-spins wedge. From these, the number with $S_{\rm total} = 3$ is $2S + 1 = 7$, corresponding to the excited states. Thus, we need to show that there are exactly 20 more states, thereby demonstrating linear independence. In order to be qualified as valence bond states, the (20) states to be considered must contain at least one singlet, i.e. a valence bond between two neighboring spin-1/2 constituents. In Fig. 4.4, we have indicated the distinct states for $S^z_{\rm total} = 0, 1, 2$. The corresponding diagrams for $S^z_{\rm total} = -1$ and $S^z_{\rm total} = -2$ are obtained by replacing $S^z = 1$ with $S^z = -1$ wherever they appear in the $S^z_{\rm total} = 1, 2$ pictures, respectively. Each of the states shown in fact represents three, one being of the present form, plus two others acquired upon rotation (moving the singlet/triplet bonds to either of the other two links). Note that in all the states that we have produced, there is at least one valence bond (solid line, $S^z = 0$). The dashed lines represent triplet bonds, and the S^z of these and the other site are as shown.

With all states identified in every S^z sector, the next thing we do is compute the overlap matrix in each, possible since different sectors do not mix. We also obtain the corresponding

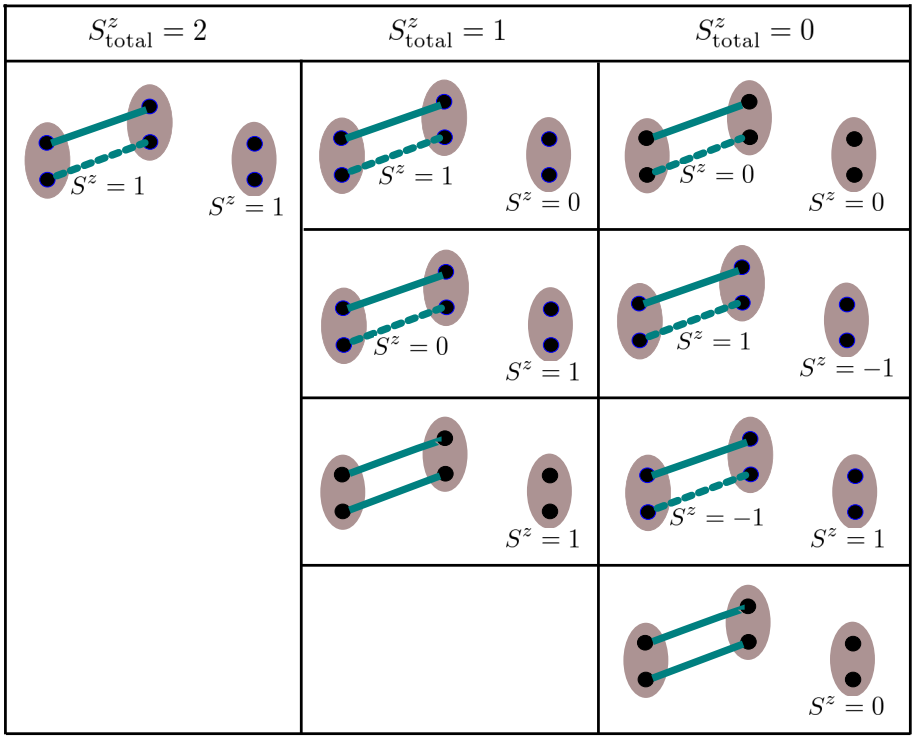


Figure 4.4: $S = 1$ spins (shaded oval) are comprised of two spin-1/2 constituents (black circles). Each column depicts the various possibilities for states in the triad with the indicated S^z_{total}. Solid lines denote dimers, i.e. singlet pairings ($S^z = 0$); dashed lines denote triplets with the indicated S^z for the pair. The S^z of the site not participating in a singlet or triplet is also indicated.

rank of the matrix, which tells us the number of linearly independent states in the sector. We use Mathematica for this. The ranks, r, that we find are as follows: (i) $S^z_{\text{total}} = 0$, $r = 6$; (ii) $S^z_{\text{total}} = 1$, $r = 5$; (iii) $S^z_{\text{total}} = -1$, $r = 5$; (iv) $S^z_{\text{total}} = 2$, $r = 2$; (v) $S^z_{\text{total}} = -2$, $r = 2$. Adding all the individual ranks, we get 20. With this result proving linear independence, we verify that the valence bond states are perfectly good states for a basis of the ground state manifold. An additional and important comment must be made. Although we have proven that these 20 states are ground states of any individual spin triad, this does not make all automatically a ground state of Hamiltonian (4.2). In order to be a ground state of the complete Hamiltonian, *all* triads must be able to host a singlet. This imposes the restriction that we have mentioned before: a site participates in two valence bonds, each in a *different* adjacent hexagon. Consequently, only

a subset of those states that we have considered here are qualified.

4.2.2.3 Non-orthogonality: A calculation of the ground states' overlaps

As has already been mentioned, the states of the kind given by Eq. (4.4) are not orthogonal. In this section we develop a description for calculating their overlaps. As will be apparent in section 4.3.1, the overlap matrix is necessary to orthogonalize the states. The first observation is that the valence bonds form loops as each site participates in exactly two bonds, one in each adjacent hexagon. We calculate the factor that one such loop $\mathcal{L}$ contributes to the norm squared of the above state (4.4),

$$Z(\mathcal{L}) = \langle \varnothing | \prod_{(i\to j)\in\mathcal{L}} (a_i b_j - b_i a_j) \prod_{(k\to l)\in\mathcal{L}} \left(a_k^\dagger b_l^\dagger - b_k^\dagger a_l^\dagger \right) | \varnothing \rangle; \tag{4.5}$$

the products are taken over all lattice bonds participating in a given loop. These bonds are oriented in some manner in order to fix a sign convention for the singlets residing there, but none of the physical quantities should depend on a particular choice. Before we proceed to calculate $Z(\mathcal{L})$, it should be noted that all legitimate loops $\mathcal{L}$ that can participate in a ground state discussed here are of *odd* length. This property will become important in what follows, and is fairly easy to establish. First of all, notice that any two subsequent bonds in a loop can either form a straight line or a 60° corner; this follows from the requirement that these bonds belong to two different hexagons. Then, by examining the lattice, we notice that all triangles – the only legitimate convex loops – have sides of odd length (and hence odd perimeters). Finally, all other loops can be deformed into triangles by repeated "filling in" of the concave corners either by rhombi with sides of length 2 (attaching such a rhombus does not change the length of a loop being modified) or by trapezoids with sides of lengths 3, 2, 1 and 2 (in which case the length of the affected loop is reduced by 6, without affecting its parity).

In order to evaluate the overlap $Z(\mathcal{L})$, as well as to help us evaluate the off-diagonal overlap matrix elements later, let us introduce the following graphical representation for the terms in the expansion obtained by multiplying all factors in Eq. (4.5). For a bond $(i \to j)$, we introduce an additional green arrow pointing from i to j if the corresponding term in the expansion contains $a_i^\dagger b_j^\dagger$ and pointing from j to i if the term contains $b_i^\dagger a_j^\dagger$ instead. Similarly, yet another, yellow arrow points from i to j if the term of interest contains $a_i b_j$ and from j to i if it contains $b_i a_j$. In other words, green (yellow) arrows always point from sites with $a^\dagger$ (a) operators to the sites with $b^\dagger$ (b) operators. According to this convention, the corresponding pair of $a^\dagger b^\dagger$ (ab) operators comes with a $(+)$ sign if the orientation of the (colored) arrow coincides with that of the bond and a $(-)$ sign if they are opposite. For example,

$$i \qquad\qquad j = (-b_i a_j)\, a_i^\dagger b_j^\dagger. \tag{4.6}$$

Notice that the order of operators in the terms resulting from the expansion of Eq. (4.5) is always *antinormal*, i.e. all creation operators are to the right of all annihilation operators. Also notice that for the purposes of calculating the overlap of a state with itself, all bonds belonging to a loop must carry both green and yellow arrows.

Let us now turn to the allowed vertices in this representation. Each site must have two Schwinger bosons (of any kind) created and subsequently annihilated there. Therefore the only possibilities for the operators on site i that produce a non-zero contribution to the expansion of Eq. (4.5) are $(a_i)^2(a_i^\dagger)^2$, $(b_i)^2(b_i^\dagger)^2$ and $a_i b_i a_i^\dagger b_i^\dagger$ with $\langle\varnothing|(a_i)^2(a_i^\dagger)^2|\varnothing\rangle = \langle\varnothing|(b_i)^2(b_i^\dagger)^2|\varnothing\rangle = 2$ and $\langle\varnothing|a_i b_i a_i^\dagger b_i^\dagger|\varnothing\rangle = 1$. Graphically, these possibilities correspond to:

$$i \qquad = (a_i)^2(a_i^\dagger)^2; \qquad\qquad i \qquad = (b_i)^2(b_i^\dagger)^2; \tag{4.7a}$$

$$i \qquad = \qquad i \qquad = \qquad i \qquad = \qquad i \qquad = a_i b_i a_i^\dagger b_i^\dagger. \tag{4.7b}$$

Notice that while all vertices in Eq. (4.7b) have the same operator content, they all originate from different terms in the expansion of Eq. (4.5) and hence are *distinct* vertices. Vertices in

Eq. (4.7a) represent sources/sinks for colored arrows while the vertices in Eq. (4.7b) conserve the flow of arrows of each kind.

A few observations are in order:

(i) Sources and sinks always come in pairs and must alternate along the loop – this is just another manifestation of the non-local (hidden) order in the AKLT chains [20, 4].

(ii) The presence of a single source/sink pair forces all flow-conserving vertices to have green and yellow arrows flow in parallel with one another (i.e. only the first two types of vertices in Eq. (4.7b) can be present). Consequently, the loops with counter flows of green and yellow arrows must contain no sources or sinks and can consist entirely of a single kind of vertices (of either third of fourth type in Eq. (4.7b)).

(iii) A bond with parallel flows of green and yellow arrows always comes with a positive sign while a bond with counter flows always comes with a negative sign, independently of the initial orientation of the singlet.

An immediate consequence of (ii) and (iii) is that all arrow configurations containing sources and sinks give strictly positive contributions to the expansion of Eq. (4.5), while the contributions of all source/sink-free configurations cancel each other: due to the odd loop perimeter, the contributions of counter-flowing configurations are always negative.

Therefore we have successfully reduced the problem of evaluating Eq. (4.5) to a purely combinatorial question of counting all possible (non-empty) configurations of alternating sources and sinks around the loop; each source or sink yields a factor of two to the overall matrix element. For a loop of perimeter p, there are $2\binom{p}{2m}$ distinct ways of placing m source/sink pairs. The factor of two results from the fact that once the locations of those vertices are chosen, one still has the freedom of designating the first one to be a source or a sink; the rest should follow

in an alternating order. Therefore

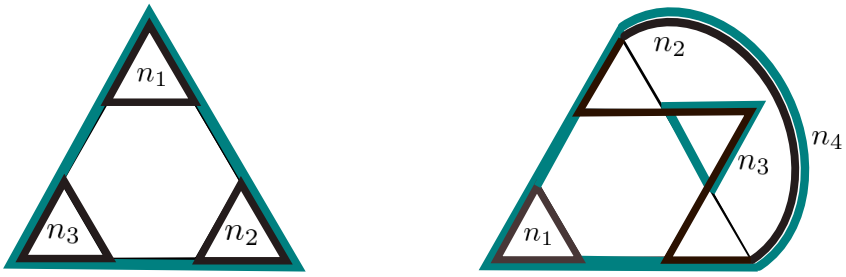
$$Z(\mathcal{L}) = \sum_{m=1}^{(p-1)/2} 2^{2m+1}\binom{p}{2m} = 2\sum_{m=0}^{(p-1)/2} 2^{2m}\binom{p}{2m} - 2$$
$$= \sum_{k=0}^{p}\left[2^k + (-2)^k\right]\binom{p}{k} - 2 = 3^p - 3. \quad (4.8)$$

The norm squared of a ground state represented by a collection of such loops is then

$$\langle\Psi_{\rm GS}|\Psi_{\rm GS}\rangle = \prod_{\mathcal{L}}\left(3^{p(\mathcal{L})} - 3\right) \quad (4.9)$$

which clearly depends on the details of a particular loop configuration (albeit its biggest term, $3^{\sum p(\mathcal{L})} = 3^N$, does not).

Next, we want to consider the off-diagonal elements of the overlap matrix. In the discussion, we will be restricting to the case where the two states involved have a single hexagon mismatch, that is, their pseudospins are antiparallel in only one hexagon . This gives rise to two possibilities for the loops that form in the overlap. Fig. 4.5 illustrates the situations, where the two states are indicated by the black and the teal colors. We first discuss Fig. 4.5(a), in which the hexagon flip changes a single loop into three loops: each black dimer in the mismatched hexagon belongs to a different loop. Although we have illustrated this using the smallest loop possible (of length 3), loops can be of any (odd) length. With the objective of calculating $Z(1 \text{ hexagon flip})$, we investigate the arrow configurations that can contribute to this overlap. First we look at the configurations of flow-conserving vertices, which we also refer to as "defect-free". Note that, for a fixed arrow orientation in the teal state, there are two choices for the arrows in the black: (1) parallel or (2) antiparallel. When in parallel, we learned above that all vertices will yield a positive contribution. However, for case (2), all contributions from a single (black, odd-length) loop come with a minus sign; this is completely independent of the other two loops. Hence, cases (1) and (2) cancel each other, demonstrating that there are no defect-free overlaps. Having eliminated these, we need to count how many of the other "defect" configurations – those that



(a) (b)

Figure 4.5: When two valence bond states (the teal and the black) overlap with a single hexagon mismatch (i.e. opposite pseudospins), loops around the hexagon can be of two different forms: (a) each dimer of the hexagon in the black state belongs to a different loop; (b) two dimers of the hexagon in the black state belong to the same loop, and the third to a different one. Everywhere outside this particular hexagon, the teal state is exactly the same as the black state. The n_i denote the lengths of the loops.

contain sources/sinks – there are. As sources and sinks alternate around a loop (according to point (i) above), an additional observation is made: arrows at the corners of the hexagon alternate in order (2 in - 2 out, along the hexagon), enforcing a new restriction. Using the result of Eq. 4.8 for a single loop, we get the following expression for the overlap in Fig. 4.5(a):

$$\begin{aligned} \Omega^{(3\text{ loops})} &= \frac{2}{\sqrt{|\Psi_{\text{green}}|^2}\sqrt{|\Psi_{\text{red}}|^2}} \left(\frac{3^{n_1}-3}{2}\right)\left(\frac{3^{n_2}-3}{2}\right)\left(\frac{3^{n_3}-3}{2}\right) \\ &= \frac{1}{4}\sqrt{\frac{(3^{n_1}-3)(3^{n_2}-3)(3^{n_3}-3)}{3^{n_1+n_2+n_3}-3}}. \end{aligned} \tag{4.10}$$

Notice that in each parenthesis of the first line we have divided by a factor of two; this is due to the restriction we mentioned previously, a choice that is absent here. Independent of this constraint though, the arrows along the hexagon still have the freedom to follow any of two orders, 2 in, 2 out, etc., or 2 out, 2 in, etc.; this freedom is represented by the factor of 2 in the numerator. The n_i are the loop lengths as indicated in Fig. 4.5(a). Note that the length of the teal loop is $n_1 + n_2 + n_3$, used in the normalization of the state.

We now calculate the overlap between the black and the teal states for the situation depicted in Fig. 4.5(b). In this instance, two of the black dimers belong to the same loop. In the figure, the curved part of the loop is supposed to represent an arbitrary loop shape beyond the immediate boundaries. The lengths of the loops are as follows: n_1 for the small black loop; n_2 for the big black loop; n_3 for the small teal loop; and n_4 for the large teal loop. The latter are related through the equation $n_1 + n_2 = n_3 + n_4$. Calculating the overlap involves counting the sinks/sources in each of the *inner* loops (n_1, n_2, n_3). For the loops of lengths n_1 and n_3, their respective contribution is $\left(\frac{3^{n_i}-3}{2}\right)$, following the same reasoning as for the loops of Fig. 4.5(a). The case for the big black loop is a little bit different. For the portion that overlaps with the small teal loop (segment one), we already know that two defects (and one non-defect) have to be present, so one can pay attention to the other loop portion (segment two) only. In segment two, the number of defects can be 0, 2, 4, ..., $n_2 - n_3$, the important thing being that 0 is a possibility since segment one already contains a pair of defects. Note that for segment two, the number of sites $(n_2 - n_3)$ available for the placement of a defect does not correspond to its length; the latter is only true for a complete loop. Hence its contribution to the overlap is $\left(\frac{3^{n_2-n_3}+1}{2}\right)$. Having a $(+1)$ instead of a (-3) in the numerator reflects the possibility of zero defects. After the appropriate normalization, the overlap is given by

$$\Omega^{(2\text{ loops})} = \frac{1}{4}\sqrt{\frac{(3^{n_1}-3)(3^{n_3}-3)}{(3^{n_2}-3)(3^{n_4}-3)}}(3^{n_2-n_3}+1), \tag{4.11}$$

where we have added the factor of two for choice of arrow alternation along the hexagon. There are a two additional points that must be made in relation to Eqs. (4.10) and (4.11). These are that (i) the "topology" of the loops matter; although in both of these cases discussed the overlap comes from a single hexagon mismatch, the exact details of the loops play a role; (ii) both Eq. (4.10) and Eq. (4.11) have the same limit for large loops, namely when $n_i \to \infty$; this limit is 1/4.

4.3 Perturbing the Hamiltonian back to the nearest-neighbor Heisenberg form

Hamiltonian (4.2) involves interactions between nearest and next-nearest neighbors. To move the system in the direction of the conventional nearest-neighbor Heisenberg Hamiltonian, our original interest and motivation, we enhance the interactions of this type already present by introducing an additional Heisenberg term perturbatively. As we do this, the questions we are trying to answer are: How has the system been altered? What new interactions has the Heisenberg perturbation generated? And finally, what type of ground state(s) emerge from these? In the next section, we first proceed by a general presentation of our calculations. The questions we just posed will be addressed more concretely in section 4.4.

4.3.1 Perturbation theory calculations

The Heisenberg perturbation Hamiltonian is

$$H_{\text{Heis}} = \sum_{\langle ij \rangle} H^{ij}_{\text{Heis}} = J \sum_{\langle ij \rangle} \mathbf{S}_i \cdot \mathbf{S}_j, \tag{4.12}$$

where the sum is over all nearest-neighbor spins $\langle ij \rangle$. The effect of this addition to the system can be captured by the energy corrections that it introduces. Here, we calculate first-order energy corrections by means of perturbation theory. Namely, we need to compute the matrix elements of the Heisenberg Hamiltonian in the ground states of the parent Hamiltonian,

$$\langle \Psi^{(m)}_{\text{GS}} | H_{\text{Heis}} | \Psi^{(n)}_{\text{GS}} \rangle \tag{4.13}$$

with $|\Psi^{(n)}_{\text{GS}}\rangle$ as given in Eq. (4.4). Since Eq. (4.12) is a sum over all the links, we can start our calculation by considering its effect on a single one of these, as indicated in Fig. 4.6, and then utilize the appropriate symmetry relations to get the full Hamiltonian. Note that this link

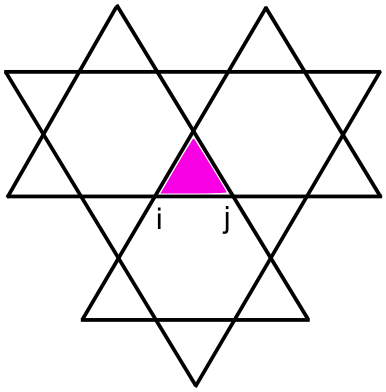


Figure 4.6: The sites of the link $< ij >$ involve only three hexagons. This allows reducing the calculation of the matrix elements (4.13) to the calculation of the matrix elements of (4.12) in the corresponding valence bond states of these three hexagons only. Once (4.12) is applied to the link $< ij >$, we apply the appropriate rotations to get the total contributions from the upward-looking (shaded) triangle. Downward-looking triangles are accounted for later in the effective Hamiltonian by application of symmetry relations.

is part of the triangle embedded within the three hexagons shown. Thus, the pseudospin, equivalently valence bond, state of these hexagons completely determine the state of said triangle, in particular of link $\langle ij \rangle$. For this reason, we can reduce the calculation of expression (4.13) to a calculation of $\langle \Psi_\alpha | H^{ij}_{\text{Heis}} | \Psi_\beta \rangle$, where $|\Psi_\alpha\rangle$ is one of the eight 3-hexagons states given in Fig. 4.7. Recall that since each hexagon can have two pseudospin states, up and down, the total number of states for the three hexagons is $2^3 = 8$. In each case, we have also indicated the corresponding valence bond state by the placement of the red dimers. We observe that the states can be divided into four categories, distinguished by the condition of sites i and j with respect to each other (although not indicated, i and j refer to the same locations as in Fig. 4.6): i and j (A) have a dimer in common and each makes a dimer with another common site, i.e. they are in a loop, state 1; (B) do not share a dimer, but are connected via others, state 2; (C) share a dimer, but are disconnected otherwise, states 3, 5, and 7; (D) are completely disconnected, states 4, 6, and 8. We next proceed to calculate first the diagonal elements $\langle \Psi_\alpha | H^{ij}_{\text{Heis}} | \Psi_\alpha \rangle$, for $\alpha = 1 - 8$.

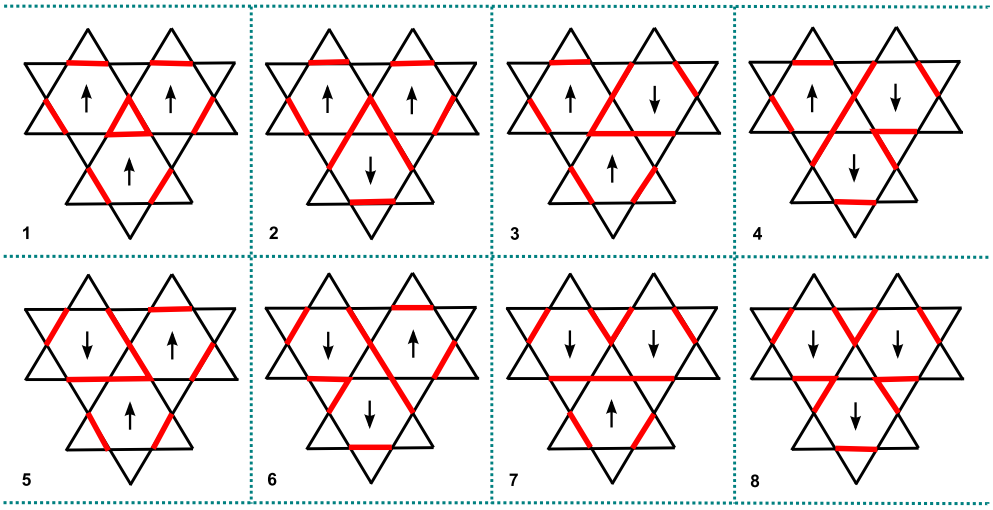


Figure 4.7: These are the $2^3 = 8$ states for the three hexagons used in the calculation of $\langle\Psi|H^{ij}_{\text{Heis}}|\Psi\rangle$. The figures display both the pseudospin states (denoted by the arrows), as well as the corresponding valence bond states (indicated by the red dimers).

For a moment, we pause to introduce the notion of hidden order, an occurrence present in AKLT-like spin states. This order is exemplified in Fig. 4.8 for $S = 1$ spins. As nearest-neighbor spins (the spin-1/2 constituents) are coupled into singlets, the following order results in the S^z component of each site: a non-zero S^z is always followed by a non-zero S^z of the opposite sign, independent of how many $S^z = 0$ occur in between. (We already employed this notion in the calculation of the overlaps in section 4.2.2.3.) This means that sites that share a dimer cannot have an S^z of the same non-zero value.

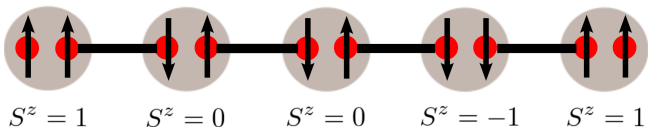


Figure 4.8: Hidden order: A non-zero S^z is always followed by a non-zero S^z of the opposite sign, independent of how many $S^z = 0$ occur in between.

We utilize this knowledge to help us derive a technique for calculating the matrix elements. Figure 4.9 depicts the only allowed states of a particular site i in terms of its Schwinger

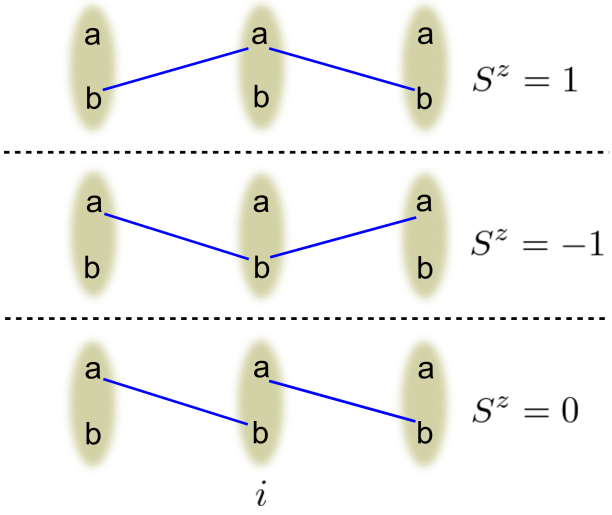


Figure 4.9: A site i with two species of bosons, a and b. The blue lines are the valence bonds between site i and its neighboring sites. These can connect bosons of different type only.

boson occupancy. The letters a and b denote the two boson species, and the shaded oval is meant to represent the site, comprised of the two types. The adjacent sites, not labeled, are there to illustrate that valence bonds, the solid lines, can only connect different species. Then, if two valence bonds emanate from a, the corresponding S_i^z is $S_i^z = 1/2(n_i^a - n_i^b) = 1/2(2-0) = 1$; if two valence bonds emanate from b, $S_i^z = 1/2(n_i^a - n_i^b) = 1/2(0-2) = -1$; and if a valence bond emanates each from a and b, $S_i^z = 1/2(n_i^a - n_i^b) = 1/2(1-1) = 0$. Here, $n_i^a = a^\dagger a$ is the number operator, which indicates the occupancy of a bosons in site i; similarly for b. With these definitions, the hidden order in mind, plus Eq. (4.12) written in the Schwinger boson formalism,

$$H_{\text{Heis}}^{ij} = \frac{J}{2}\left[\frac{1}{2}(n_i^a - n_i^b)(n_j^a - n_j^b) + a_i^\dagger b_i a_j b_j^\dagger + a_i b_i^\dagger a_j^\dagger b_j\right], \tag{4.14}$$

we compute the matrix elements $\langle\Psi_\alpha|H_{\text{Heis}}^{ij}|\Psi_\alpha\rangle$ for cases (A)–(D) described previously. The calculational technique we utilize here involves a representation of the states (four cases) in the language of Fig. 4.9 and the application of Eq. (4.14) on the bond $\langle ij\rangle$. For example, application of the operator $a_i^\dagger b_i$ on the third case (top bottom) of Fig. 4.9 would result in the first case, with an overall factor of $\sqrt{2}$; the same applies to site j. Each case ((A)–(D)) corresponds to differ-

ent hidden-order configurations, to which we apply Eq. (4.14) in order to obtain the complete contribution to the matrix element. Since this implicates considerable pictorial manipulation, we omit the calculations here and only report our findings: (A) $-J$; (B) $\frac{4}{9}J$; (C) $-\frac{4}{3}J$; (D) 0. Although correct, these results are not in final form (for missing states' othrogonalization), but we quote them to illustrate that the same numbers are obtained for all cases within each classification. Although we do not continue to calculate the off-diagonal matrix elements with this technique, we use our previous analytical results to verify the reliability and reproducibility of our Mathematica code, which we use to obtain the complete Heisenberg Hamiltonian.

Since we have only considered the link $\langle ij \rangle$, as we compute the full Hamiltonian, we also apply the necessary rotations to get the contributions from the other two sides of the triangle, thus determining the contribution of each upward-pointing triangle in the lattice. We also employ symmetry relations to obtain the corresponding contributions from downward-pointing triangles, subsequently accounting for all triangles, or equivalently, all the sites in the lattice. All this will be reflected later in the effective Hamiltonian when written in terms of pseudospin variables. But for now, in order to fully complete the calculation, we need to address the non-orthogonality of the states $|\Psi_\alpha\rangle$. Orthogonalization of these is necessary for a correct representation of the Heisenberg Hamiltonian in this basis. With the orthogonalized states[3] given by

$$|\tilde{\Psi}_\alpha\rangle = \sum_\beta (\Omega^{-1/2})_{\alpha\beta} |\Psi_\beta\rangle, \tag{4.15}$$

where $\Omega_{\mu\nu} = \langle \Psi_\mu | \Psi_\nu \rangle$ is the overlap matrix (element) between the non-orthogonal valence bond states, the final Heisenberg matrix elements are

$$\langle \tilde{\Psi}_\alpha | H_{\text{Heis}} | \tilde{\Psi}_\beta \rangle = \sum_{\mu\nu} (\Omega^{-1/2})_{\alpha\mu} \langle \Psi_\mu | H_{\text{Heis}} | \Psi_\nu \rangle (\Omega^{-1/2})_{\beta\nu}. \tag{4.16}$$

[3]For a reminder of valence bond states' orthogonalization, the reader is encouraged to go back to Chapter 2 where this was discussed in more detail.

A few comments about the expression above are in order. In section 4.2.2.3, we discussed the non-orthogonality of the valence bond states, that is, the fact that they have non-zero overlaps. In particular, it was shown that, when restricted to small loops, overlaps have a dependence on the lengths of these loops, as seen in Eqs. (4.10) and (4.11). In fact, loops in the transition graph can in principle be large, meaning beyond the elementary loop. This non-locality is a strong feature of the overlap matrix. The inevitable, and admittedly undesirable, consequence of this is a dependence of the overlaps on the size of the system being used. To obtain the matrix elements in Eq. (4.16), we computed the overlap matrix in the limit of large loops ($n_i \to \infty$ in (4.10) and (4.11)), where the dependence on loop length vanishes. However, calculation of the same when restricting to small loops (i.e. when using the above equations) is of no effect on the overall conclusions that we make about the system, more specifically about the state of the resulting effective Hamiltonian. A further comment will be made about this in section 4.4.

4.3.2 Effective Hamiltonian

Once the matrix elements in expression (4.16) have been calculated, we can write the Heisenberg Hamiltonian in the following way,

$$\begin{aligned}\tilde{H}_{\text{Heis}} &= -2.97J|\uparrow\uparrow\uparrow\rangle\langle\uparrow\uparrow\uparrow| + 0.20J|\downarrow\downarrow\downarrow\rangle\langle\downarrow\downarrow\downarrow| \\ &\quad -6.47J|\uparrow\uparrow\downarrow\rangle\langle\uparrow\uparrow\downarrow| - 3.66J|\downarrow\downarrow\uparrow\rangle\langle\downarrow\downarrow\uparrow| \\ &\quad -0.79J|\uparrow\uparrow\downarrow\rangle\langle\uparrow\uparrow\uparrow|. \end{aligned} \tag{4.17}$$

Here, the arrows in the projectors represent the pseudospins of the three hexagons, where $\uparrow$ is for $\sigma^z = 1$ and $\downarrow$ for $\sigma^z = -1$. One observes that, with the exception of the last, the rest of the terms correspond to operators that do not change the original pseudospin orientations. In contrast, the last operator flips one pseudospin. Although two- and three-pseudospins flips are also possible, we find their coefficients to be negligibly small.

Next, we write the effective Hamiltonian that can reproduce the actions of Eq. (4.17); we write it in terms of the pseudospin variables σ^z that live at the centers of the hexagons. We note that these centers form a triangular lattice and so, as we write the Hamiltonian, we remark that the interactions are not among the $S = 1$ spins on the kagomé lattice, but between pseudospins residing on the sites of a triangular lattice. As we stated we would do, in the following we have already accounted for all triangles, i.e., for all the sites. The effective Hamiltonian is

$$\tilde{H} = K_2 \sum_{\langle ij \rangle} \sigma_i^z \sigma_j^z + K_3 \sum_{i,j,k \in \triangle} \sigma_i^z \sigma_j^z \sigma_k^z - K_3 \sum_{i,j,k \in \triangledown} \sigma_i^z \sigma_j^z \sigma_k^z + h_1 \sum_i \sigma_i^x + g_3 \sum_{i,j,k \in \triangle, \triangledown} \sigma_i^x \sigma_j^z \sigma_k^z. \quad (4.18)$$

In the first sum, the two-pseudospin interactions are taken over all nearest-neighbor sites $\langle ij \rangle$. The next two terms represent three-body interactions on the upward- and downward-pointing triangles, respectively. In the fourth sum over all sites, the operator σ_i^x flips the pseudospin at site i. As we noticed a dependence of the coefficient associated with this flip on the state of the other two pseudospins in the plaquetette, the last term in Eq. (4.18) became necessary; it is a sum over all triangles. Operators of the type σ_i^z as well as energy constants are left out given their immateriality in the face of the other terms. Using Eq. (4.17), we calculate the coefficients in Hamiltonian (4.18). The results are these: $K_2 = 1.84J$, $K_3 = 0.66J$, $h_1 = -0.79J$ and $g_3 = -0.01J$.

4.4 Analysis of effective Hamiltonian

4.4.1 Discussion of the effective Hamiltonian's interactions

According to the values obtained, Hamiltonian (4.18) is, and consequently any ground state of it, fundamentally governed by the K_2 term. Given that $K_2 > 0$, since J is, the system favors the antiparallel alignment of any pair of pseudospins. Due to the geometry of the lattice, this antiferromagnetic arrangement results in a fully frustrated system [93]. The least frustration, and hence an optimal state, is achieved when each triangular plaquette has at most one unsatisfied bond. There are many ways that this can be accomplished; consequently, a largely degenerate ground state gives rise. The configuration (per plaquette) $\uparrow\uparrow\downarrow$ gives such a state, as does its inverse. To such a background one must incorporate the effects of the K_3 terms. To investigate what happens, we consider the following. The fact that each triangle has a frustrated bond is accounted for first by placing said bond in the middle of a rhombus that comprises two triangles, so that the frustrated bond is the same for both (see Fig. 4.10). To ensure that this "grouping" puts exactly one unsatisfied bond per triangle, one needs to show that the rhombi are non-overlapping. This is done by referring to the dual lattice, in which a frustrated link is represented by a dimer drawn perpendicular to it, i.e., completely contained inside the rhombus. Since dimers do not touch[4], this means that rhombi do not intersect. Hence, all triangles are covered in this rhombus representation. From the signs of the pseudospins, two distinct cases arise for the rhombi, Fig. 4.10 illustrates them. The circled sign is the overall sign of the operator product $\sigma_i^z \sigma_j^z \sigma_k^z$. In each case we see that the signs are the same for the upward- and the downward-pointing triangles in each rhombus. Therefore, the total contribution from the up-pointing triangles is equal to that of the down-pointing triangles. Since their respective

[4] In this case of "Ising" pseudospins, a site in the dual lattice can only participate in one dimer, so these do not come into contact.

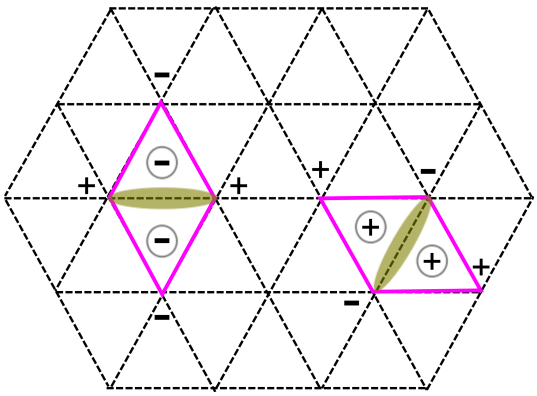


Figure 4.10: In the ground state of the K_2 term of Hamiltonian (4.18), there are two possibilities for a rhombus (pink outline) with a frustrated bond (shaded ellipse) in the middle. The circled signs are the overall signs of the operator product $\sigma_i^x \sigma_j^z \sigma_k^z$ in the plaquette. Account of these signs on the upward- and downward-looking triangles lead to the vanishing of the K_3 terms in Eq. (4.18).

sums appear in (4.18) with the opposite sign, their contributions vanish. Restated in different words, the K_3 terms have no effect on the ground state when the latter is dominated by the antiferromagnetic interactions of the K_2 term.

The next term we consider is $h_1 \sum_i \sigma_i^x$, which represents a transverse magnetic field in the system. As stated in section 4.3.2, σ_i^x is a "flipping" operator. As it is applied to all the sites of the lattice, its effect is to simply change the location of the unsatisfied bond in the plaquettes; effectively, this term in the Hamiltonian moves the system from one optimal state to another. And finally, we look at the last term of Eq. (4.18). As observed earlier, this operator takes care of the fact that a single pseudospin flip yields different outcomes depending on the orientations of the other two. Albeit an interesting and potentially determining feature, the relatively small strength of this term makes its influence insignificant. Hence, based on the preceding discussion, our effective Hamiltonian is reduced to an antiferromagnetic Ising model in a transverse field on the triangular lattice, namely,

$$\mathcal{H} = K_2 \sum_{\langle ij \rangle} \sigma_i^z \sigma_j^z + h_1 \sum_i \sigma_i^x. \tag{4.19}$$

4.4.2 Order by disorder

It has been stated at some point in this dissertation that systems with competing interactions exhibit a high degree of frustration that is manifested as an extensive ground state degeneracy. Lifting this degeneracy becomes possible only with the introduction of quantum fluctuations.[5] Among the degenerate states, those that are particularly flexible to these fluctuations are selected as most favorable. Moreover, these states are distinct thanks to some type of order which is absent in the others. This mechanism of degeneracy-breaking is known as *order by disorder*.

As was explained in the previous section, the large ground state degeneracy of Hamiltonian (4.19) comes from the antiferromagnetic Ising interactions, which constitute the dominant term. Knowledge of the classical Ising antiferromagnet has been around since 1950 [93, 34]: the system does not order at any finite temperature, and at $T = 0$ it possesses a nonzero ($0.323k_{\mathrm{B}}$) residual entropy per spin indicative of a highly disordered degenerate ground state. The state also has spin–spin (pseudospin in our case) correlations that decay algebraically as $\langle \sigma^z_{\mathbf{0}} \sigma^z_{\mathbf{r}} \rangle \propto r^{-1/2} \cos(\frac{2}{3}\pi r)$ [88]. However, as indicated above, our system consists of more than just the AF Ising part. It also contains the transverse field term, which introduces the quantum fluctuations into the system; these are the same that make the system move from ground state to ground state to eventually adopt a unique ordered state from among the present disorder. The system thus exhibits an order-by-disorder mechanism that is manifested as a phase transition in the temperature–field ($T - h_1$) phase diagram [62, 60]. The transition at $T = 0$ is from a fully disordered state above a critical point, into an order-by-disorder phase below this point. Utilizing the mapping from a $(d+1)$-dimensional classical model to a d-dimensional quantum model [13, 60], we determine the critical value for the transition to be $(h_1/K_2)_{\mathrm{c}} \approx 1.37$.

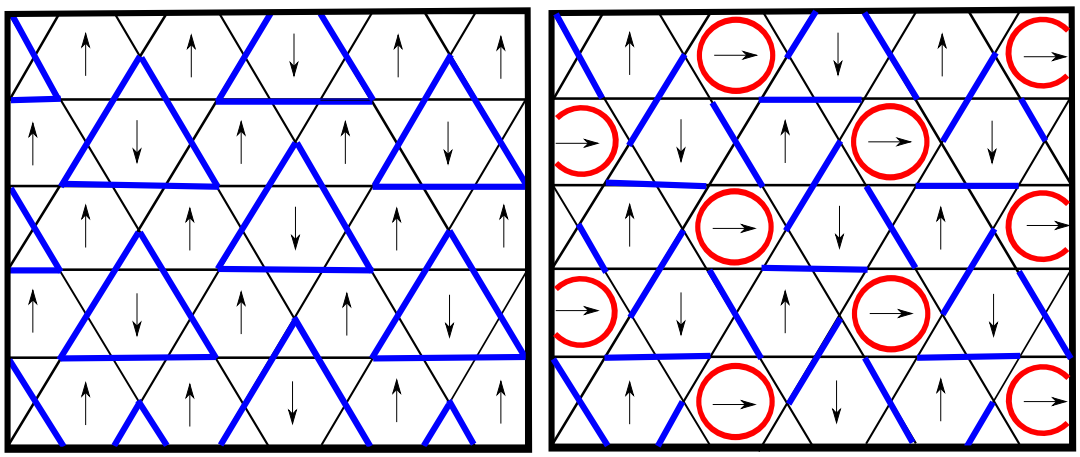
[5] This is the case in quantum frustrated systems. Classically, the degeneracy lifting occurs due to thermal fluctuations.

According to the values we quoted before, we find $h_1/K_2 \approx 0.43$ for our system, putting it well below the transition in the order-by-disorder phase. Previously, we stated that calculating the overlap matrix in the large-loop limit vs the short-loop limit was of no consequence to our results. This is what we meant: although calculation of the overlap matrix in the latter limit yields a different value for h_1/K_2, this value (shifted to the right) is still within the region of the order-by-disorder phase; it does not get near the phase boundaries. For this reason, everything that we say now is consistent with either limit used in the calculation.

4.4.3 Low-energy states

In this section we look at the order-by-disorder state that describes the ground state of Hamiltonian $\mathcal{H}$ in (4.19). The discussion revolves around two competing order-by-disorder states. One of these was already alluded to previously; it is the state where each triangular plaquette has the pseudospin configuration $\uparrow\uparrow\downarrow$. This state, depicted in Fig. 4.11(a), is denoted by its sublattice magnetizations (+, -, +). Also shown in the figure by the blue dimer pattern is its valence bond representation in the original kagomé lattice. The state's selection as an order-by-disorder state originates from the 2/3 of the total pseudospins being flippable; this number is the maximum possible. Here, the term "flippable" refers to the capacity of a plaquette to change from the configuration $\uparrow\uparrow\downarrow$ to the configuration $\uparrow\downarrow\downarrow$ or $\downarrow\uparrow\downarrow$. In possessing such capacity, quantum fluctuations are facilitated. This flexibility, however, becomes the state's own demise: as soon as one pseudospin is flipped, the once maximal 'flippability' is annulled. This condition, or rather the avoidance of, gives rise to the second competing order-by-disorder state, as explained next.

Figure 4.11(b) illustrates the other candidate order-by-disorder ground state, which is characterized by the sublattice magnetizations (+, 0, -). In this state, a constant maximum flippability is secured in the following manner: one of the sublattices is made invariably flippable



(a) (b)

Figure 4.11: Caricatures of the competing order-by-disorder ground states of Hamiltonian (4.18), the triangular Ising model in a transverse field. The states are characterized by the sublattice magnetizations (a) (+, -, +) and (b) (+, 0, -). Conventions: Blue lines and red circles (see text for explanation) represent the dimer states in the original kagomé lattice. The arrows are the corresponding pseudospins in the triangular lattice, where $\rightarrow = (\uparrow + \downarrow)/\sqrt{2}$.

by forming a superposition of up and down states, $\rightarrow = (\uparrow + \downarrow)/\sqrt{2}$ (see Fig. 4.11(b)); meanwhile, the other two sublattices form an ordered state. In the usual valence bond description, the pseudospin superpositions (horizontal arrows) are expressed as red benzene rings representing the configuration $\hexagon = (\therefore + \because)/\sqrt{2}$, where dots denote dimers.

4.4.3.1 Discussion of the ground state

To assist us in the determination of *the* ground state of Eq. (4.19), we revisit the literature since, as has been pointed out before, the triangular Ising model in a transverse field is a well-studied system. We discuss next the findings of some of these studies. Independent of the individual approach taken, all these works [38, 63, 60] seem to draw their conclusions, at least in part, from a mapping of the quantum d-dimensional transverse Ising model onto a $(d+1)$-

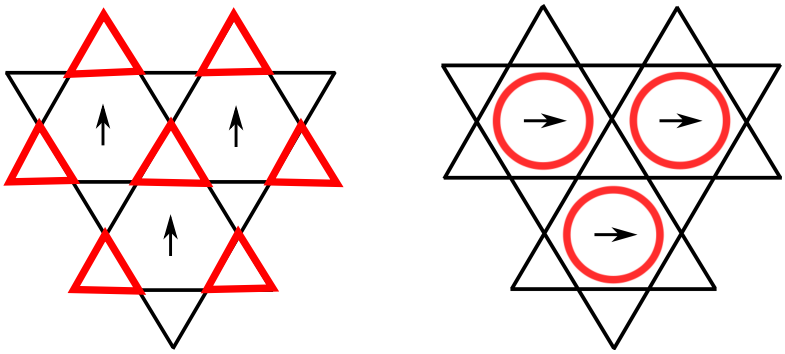
dimensional ferromagnetically stacked classical model. The classical study these allude to is that by Blankschtein et al.[13], whose Landau-Ginzburg-Wilson (LGW) Hamiltonian contained a so-called sixfold clock term. Two ordered phases, each characterized by a three-sublattice structure (corresponding to those discussed above), emerged according to the sign of the clock term's coefficient, one when positive, the other when negative. According to quantum Monte Carlo (QMC) calculations of the spin–spin correlations along the x direction and the correlation matrix of sublattice magnetizations, Moessner and Sondhi [60] confirmed the state with the sublattice structure (+, 0, -) as the ordered state at low temperature. Similar conclusions were reached by Isakov and Moessner in Ref. [38] where they investigated the interplay of quantum and thermal fluctuations in the system. Their results from QMC calculations predicted the extended critical KT phase where both types of fluctuations are important, but once again the (+, 0, -) state was found in the order-by-disorder phase part of the diagram. The authors also present in detail their findings for the ratio $h_1/K_2 = 0.4$ (Γ/J in their notation), reiterating what was just said in regards to the ordered phase. They also confidently asserted that the ordered phase is the (+, 0, -) state for h_1 values up to $h_1/K_2 = 1.2$. Given that our Hamiltonian parameters yield $h_1/K_2 \approx 0.43$, almost exactly as the value referred to above, we are also confident to say that our model is in the order-by-disorder phase with sublattice structure (+, 0, -).

Although there seems to be no doubt about *the* ground state of Hamiltonian (4.19), there is yet another way of looking at the problem that leads to the same conclusions. This view is given from the perspective of the quantum dimer model of the hexagonal lattice, which is the dual lattice[6] to the triangular. This was discussed briefly in section 4.4.1. The ground states of the (classical) Ising antiferromagnet on the triangular lattice translate into the complete dimer coverings of the honeycomb lattice, where the dimers occupy the bonds dual to the frustrated

[6]The dual lattice is constructed by connecting the centers of the triangular plaquettes.

bonds. In this dimer picture, the transverse magnetic field simply exchanges alternating dimers and empty bonds around *flippable* hexagons, in such a way that the one-dimer-per-site rule is preserved in the low-energy dynamics. After this quick review, we can refer now to the work of Moessner et al. [63], which establishes the presence of the *plaquette* phase right in between the *columnar* and the *staggered* states in phase space. Of relevance to our case is the fact that, when reduced to the Ising (plus fluctuations) model on the triangular lattice, the plaquette phase corresponds to the same sublattice structure (+, 0, -) which we have been talking about. The "plaquette" designation results from the benzene ring dimer structures mentioned before (see Fig. 4.11(b)). Just for reference, the columnar phase corresponds to the (+, -, +). This finding goes to support, once more, the proposal of the (+, 0, -) state as the ground state. Reference [63] makes a good argument as to why the latter prevails over its opponent (+, -, +); we paraphrase it here. The idea that a partially ordered state (due to the sublattice with magnetization 0) is selected over the other more ordered one is a bit surprising. However, the presence of the fluctuations cannot be ignored, as they themselves help stabilize the states in the first place. The former can, also, destroy the order as they become stronger. In the end, the state (+, 0, -) with its partial disorder can benefit from the fluctuations and actually survive them.

To complete the discussion of the ground state, one should mention the states that have been previously proposed as ground states of the spin-1 Heisenberg antiferromagnet on the kagomé lattice. Two such states are given in Fig. 4.12. The state in Fig. 4.12(a) is a fully pseudospin-polarized state proposed by Bluteau [15] from exact diagonalization studies on small spin clusters. Meanwhile, the state in Fig. 4.12(b) is the hexagonal solid state (HSS) proposed by Hida from variational methods [32]. This state corresponds to having all three sublattices polarized in the x-direction (we are using the same notation as before, where a circle or a horizontal arrow represents an up-down superposition of pseudospins). Given that both of these states are within the same Hilbert (valence bond) space as our state (i.e., the (+, 0, -)



(a) (b)

Figure 4.12: Previously proposed ground states of the spin-1 Heisenberg antiferromagnet. (a) A fully pseudospin-polarized state proposed in Ref. [15]. (b) The hexagonal solid state proposed in Ref. [32]. Red lines represent the valence bond states in the original kagomé lattice, and the arrows denote pseudospin orientations. Circles and horizontal arrows denote the superposition $\rightarrow = (\uparrow + \downarrow)/\sqrt{2}$.

state), we can make the statement that these ground states are not correct. The reason for this can be illustrated by considering the following different perspective of our study. What we have done in this investigation is basically consider a subset of the full Hilbert space of the Heisenberg Hamiltonian. We selected this subspace by utilizing our parent Hamiltonian and asked ourselves how the Heisenberg Hamiltonian would look when projected onto it. This process took us to the effective Hamiltonian, having made no uncontrolled approximations. Once at this point, we can completely ignore the fact that we used the parent Hamiltonian to get here. Then, we did an *honest* analysis of the effective Hamiltonian, finding it to be in the order-by-disorder phase. These two states that have been proposed are in the same subspace of valence bond ground states. We observe that the state in Fig. 4.12(a) would correspond to $K_2 < 0$, which is obviously not the case. The HSS (Fig. 4.12(b)), on the other hand, being quantum disordered is located in the disordered phase, once again contradicting our results.

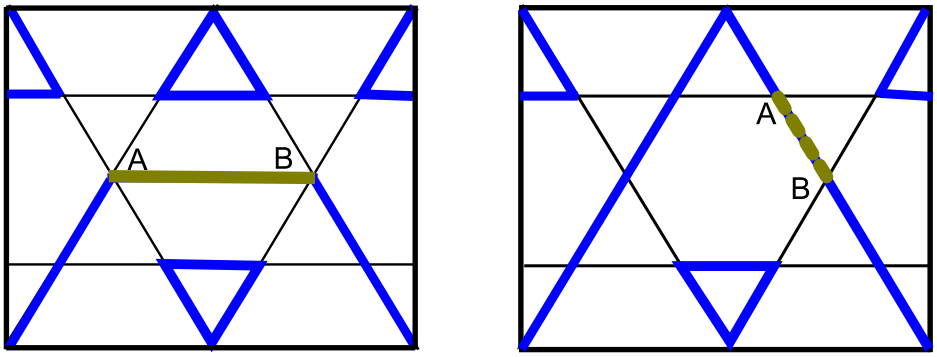
4.5 More features of the parent Hamiltonian

In this last section, we want to touch upon a few more extra points. One is to relate the coupling constant J of the perturbation in Eq. (4.12) to the Heisenberg coupling of the parent Hamiltonian (4.2). For this, we first do an expansion of the Hamiltonian as follows,

$$\begin{aligned} H &= \frac{I}{720}\sum_{\widehat{}}(\mathbf{S}_1+\mathbf{S}_2+\mathbf{S}_3)^2 \\ &\quad [(\mathbf{S}_1+\mathbf{S}_2+\mathbf{S}_3)^2-2][(\mathbf{S}_1+\mathbf{S}_2+\mathbf{S}_3)^2-6] \\ &= \frac{I}{720}\sum_{\widehat{}}(6+2\sum_{ij}\mathbf{S}_i\cdot\mathbf{S}_j) \\ &\quad (4+2\sum_{ij}\mathbf{S}_i\cdot\mathbf{S}_j)(2\sum_{ij}\mathbf{S}_i\cdot\mathbf{S}_j) \\ &= \frac{2}{15}I\sum_{ij}\mathbf{S}_i\cdot\mathbf{S}_j+\mathcal{O}(\mathbf{S}^4). \end{aligned} \tag{4.20}$$

From this we see that the parent Hamiltonian can be written in terms of a nearest-neighbor Heisenberg part plus some other quartic interactions. This tells us that, in order for our perturbative treatment to be valid, J must be much smaller than $\frac{2}{15}I$. As an extra comment, according to susceptibility measurements made by Wada et al. [91] on m-MPYNNBF4, the organic compound introduced early in the chapter, the antiferromagnetic coupling constant is $J_{\text{AF}} = 3.11K$ which, if we were to compare with our approximate treatment of the spin-1 Heisenberg model, should be related to $\frac{2}{15}I + J$.

Next, we want to discuss the energy excitations exhibited by the parent Hamiltonian, Eq. (4.2); both magnetic and non-magnetic. Non-magnetic excitations occur when a singlet, previously restricted to form between nearest neighbors, is now created from spin-1/2 constituents of non-nearest neighboring sites (Fig. 4.13(a)). On the other hand, a magnetic excitation gives rise as a singlet is raised to a triplet (Fig. 4.13(b)). In both cases, the excitations involve two triads, A and B, which fail to satisfy the local requirement for a ground state, namely, that each (triad) contains a singlet. We expect both types of excitations to be gapped and, for the reason



(a) (b)

Figure 4.13: In the ground states of the parent Hamiltonian (4.2), represented by the blue dimer coverings, an excitation (represented by the different color) that is (a) nonmagnetic occurs when the dimer is between non-nearest neighbors; (b) magnetic gives rise when the singlet pairing breaks into a triplet. In both cases, A and B indicate the triads not satisfying the local requirement for a ground state.

just stated, we expect them to be of the same order of magnitude. Reference [91] observed a spin gap $\Delta/k_{\mathrm{B}} = 0.25 \pm 0.01K$. Meanwhile, according to a numerical study of the effective Hamiltonian, namely the triangular Ising AF in a transverse field, Mostovoy et al. [47] determined a T^2 dependence of the specific heat at low temperatures, indicating a gapless nonmagnetic spectrum. They obtained this for strong transverse field, $h_1 = K_2$ ($h = J$ in their notation). However, being able to compare this behavior with the corresponding behavior in Ref. [91] is not possible due to missing data at low temperature values. In order to establish with complete certainty whether or not our model is indeed gapped requires knowledge of the energy spectrum which we don't have. The value of $h_1/K_2 = 1$ used by Mostovoy et al. is more than twice the value we found for our system, so whether one can make the same conclusions about the present case is dubious. One thing though that remains true about the system of Mostovoy et al. is that it is in the order-by-disorder phase, according to the quantum critical point we quoted before.

4.6 Conclusions

We close the chapter with a restatement of the points we believe should be the take-home message of this investigation. Here, we have studied a spin-1 kagomé antiferromagnet which, despite having a bigger spin, appears to be no more classical, yet different from its spin-1/2 counterpart. Our approach to studying the Heisenberg model on this system was to consider a "soluble point" of a parent SU(2)-symmetric Hamiltonian. Although this Hamiltonian's interactions were up to next-nearest neighbors and involved three-spin terms, it included the conventional nearest-neighbor Heisenberg interactions that were of interest to us, a good starting point for our goal. The ground states of such a Hamiltonian could be easily analyzed and we found there to be an exponential ground state degeneracy. We perturbed the parent Hamiltonian back towards the nearest-neighbor Heisenberg (Hamiltonian) by introducing an additional term of this type. Such a perturbation was found to break the exponential degeneracy. Upon analysis of the effective Heisenberg Hamiltonian, we found that the resulting low-energy sector can be described in terms of an effective transverse field Ising AF on the triangular lattice. Based on the parameters obtained for this effective model, our system is found to be in the order-by-disorder phase which is described by a pseudospin sublattice ordering with magnetization (+,0,-). It remains to be seen whether the ground state of the pure Heisenberg model is within the same quantum phase.

Bibliography

[1] I. Affleck, T. Kennedy, E. H. Lieb, and H. Tasaki. Rigorous results on valence-bond ground states in antiferromagnets. *Phys. Rev. Lett.*, 59:799–802, 1987.

[2] I. Affleck, T. Kennedy, E. H. Lieb, and H. Tasaki. Valence bond ground states in isotropic quantum antiferromagnets. *Comm. Math. Phys.*, 115:477–528, 1988.

[3] Ian Affleck. Quantum spin chains and the haldane gap. *J. Phys.: Condens. Matter*, 1:3047–3072, 1989.

[4] Ian Affleck. The haldane gap in antiferromagnetic heisenberg chains. *Rev. Math. Phys.*, 6:887–899, 1994.

[5] P. W. Anderson. New approach to the theory of superexchange interactions. *Phys. Rev.*, 115:2, 1959.

[6] P. W. Anderson. Resonating valence bonds: a new kind of insulator? *Mat. Res. Bull.*, 8:153–60, 1973.

[7] P. W. Anderson. The resonating valence bond state in La_2CuO_4 and superconductivity. *Science*, 235:1196–8, 1987.

[8] F. Anfuso and S. Eggert. Interaction effects between impurities in low-dimensional spin-(1/2) antiferromagnets. *Europhys. Lett.*, 73:271–277, 2006.

[9] Assa Auerbach. *Interacting Electrons and Quantum Magnetism*. Graduate Texts in Contemporary Physics. Springer-Verlag, New York, 1998.

[10] H G Evertz A Feiguin J Freire S Fuchs L Gamper J Gukelberger E Gull S Guertler A Hehn R Igarashi S V Isakov D Koop P N Ma P Mates H Matsuo O Parcollet G Pawlowski J D Picon L Pollet E Santos V W Scarola U Schollwock C Silva B Surer S Todo S Trebst M Troyer M L Wall P Werner B Bauer, L D Carr and S Wessel. The alps project release 2.0: open source software for strongly correlated systems. *J. Stat. Mech.*, 2011:P05001, 2011.

[11] L. Balents, M. P. A. Fisher, and S. M. Girvin. Fractionalization in an easy-axis kagome antiferromagnet. *Phys. Rev. B*, 65:224412, 2002.

[12] F. Bert, S. Nakamae, F. Ladieu, D. L'Hote, P. Bonville, F. Duc, J.-C. Trombe, and P. Mendels. Low temperature magnetization of the $s = 1/2$ kagome antiferromagnet $ZnCu_3(OH)_6Cl_2$. *Phys. Rev. B*, 76:132411, 2007.

[13] Daniel Blankschtein, M. Ma, A. Nihat Berker, Gary S. Grest, and C. M. Soukoulis. Orderings of a stacked frustrated triangular system in three dimensions. *Phys. Rev. B*, 29(9):5250–5252, May 1984.

[14] Stephen Blundell. *Magnetism in Condensed Matter*. Oxford Master Series in Condensed Matter Physics. Oxford University Press, Great ClarendonStree, Oxford OX2 6DP, 2008.

[15] Michel Bluteau. The spin 1 heisenberg kagomé antiferromagnet, August 1994.

[16] Steven T. Bramwell and Michel J. P. Gingras. Spin Ice State in Frustrated Magnetic Pyrochlore Materials. *Science*, 294(5546):1495–1501, 2001.

[17] W. J. Caspers, K. M. Emmett, and W. Magnus. The Majumdar–Ghosh chain. twofold ground state and elementary excitations. *J. Phys. A: Math Gen.*, 17:2687–2696, 1984.

[18] O. Cepas, C. M. Fong, P. W. Leung, and C. Lhuillier. Quantum phase transition induced by dzyaloshinskii-moriya interactions in the kagome antiferromagnet. *Physical Review B (Condensed Matter and Materials Physics)*, 78(14):140405, 2008.

[19] O. Cépas, K. Kakurai, L. P. Regnault, T. Ziman, J. P. Boucher, N. Aso, M. Nishi, H. Kageyama, and Y. Ueda. Dzyaloshinski–Moriya interaction in the 2D spin gap system $SrCu_2(BO_3)_2$. *Phys. Rev. Lett.*, 87:167205, Oct 2001.

[20] Marcel den Nijs and Koos Rommelse. Preroughening transitions in crystal surfaces and valence-bond phases in quantum spin chains. *Phys. Rev. B*, 40(7):4709–4734, Sep 1989.

[21] I. Dzyaloshinsky. A thermodynamic theory of 'weak' ferromagnetism of antiferromagnetics. *J. Phys. Chem. Solids*, 4:241–255, 1958.

[22] M. Elhajal, B. Canals, and C. Lacroix. Symmetry breaking due to Dzyaloshinsky–Moriya interactions in the kagome lattice. *Phys. Rev. B*, 66:014422, 2002.

[23] Veit Elser. Nuclear antiferromagnetism in a registered ^{3}he solid. *Phys. Rev. Lett.*, 62:2405, 1989.

[24] Veit Elser and Chen Zeng. Kagome spin-1/2 antiferromagnets in the hyperbolic plane. *Phys. Rev. B*, 48:13647–13653, 1993.

[25] G. Evenbly and G. Vidal. Frustrated antiferromagnets with entanglement renormalization: Ground state of the spin-1/2 heisenberg model on a kagome lattice. *Phys. Rev. Lett.*, 104:187203, 2010.

[26] John E. Greedan. Geometrically frustrated magnetic materials. *J. Mater. Chem.*, 11:37–53, 2001.

[27] Karol Gregor and Olexei I. Motrunich. Nonmagnetic impurities in the spin-1/2 kagome antiferromagnet. *Phys. Rev. B*, 77:184423, 2008.

[28] F. D. M. Haldane. Nonlinear field theory of large-spin heisenberg antiferromagnets: Semiclassically quantized solitons of the one-dimensional easy-axis néel state. *Phys. Rev. Lett.*, 50:1153, 1983.

[29] Zhihao Hao and Oleg Tchernyshyov. Fermionic spin excitations in two- and three-dimensional antiferromagnets. *Phys. Rev. Lett.*, 103:187203, 2009.

[30] J. S. Helton, K. Matan, M. P. Shores, E. A. Nytko, B. M. Bartlett, Y. Yoshida, Y. Takano, A. Suslov, Y. Qiu, J.-H. Chung, D. G. Nocera, and Y. S. Lee. Spin dynamics of the spin-1/2 kagome lattice antiferromagnet $ZnCu_3(OH)_6Cl_2$. *Phys. Rev. Lett.*, 98:107204, 2007.

[31] Michael Hermele, Ying Ran, Patrick A. Lee, and Xiao-Gang Wen. Properties of an algebraic spin liquid on the kagome lattice. *Phys. Rev. B*, 77:224413, 2008.

[32] Kazuo Hida. Ground-state and elementary excitations of the $S = 1$ kagome Heisenberg antiferromagnet. *J. Phys. Soc. Jpn.*, 69:4003–4007, 2000.

[33] Kazuo Hida. Magnetization process of the $S = 1$ and 1/2 uniform and distorted kagome Heisenberg antiferromagnets. *J. Phys. Soc. Jpn.*, 70:3673–3677, 2001.

[34] R. M. F. Houtappel. Order-disorder in hexagonal lattices. *Physica*, 16:425–455, 1950.

[35] H.J. Schulz I. Affleck, D. Gepner and T. Ziman. Critical behaviour of spin-s heisenberg antiferromagnetic chains: analytic and numerical results. *J. Phys. A: Math. Gen.*, 22:511–529, 1989.

[36] H. Yano T. Okuno K. Awaga S. Ohira K. Nishiyama I. Watanabe, N. Wada and K. Nagamine. Muon-spin-relaxation study of the ground state of the two-dimensional $s = 1$ kagomé antiferromagnet [2-(3-n-methyl-pyridinium)-4,4,5,5-tetramethyl-4,5-dihydro-1 h-imidazol-1-oxyl 3-n-oxide]bf_4. *Phys. Rev. B*, 58:2438, 1998.

[37] T. Imai, E. A. Nytko, B. M. Bartlett, M. P. Shores, and D. G. Nocera. ^{63}Cu, ^{35}Cl, and ^{1}H NMR in the s=1/2 kagome lattice $ZnCu_3(OH)_6Cl_2$. *Phys. Rev. Lett.*, 100:077203, 2008.

[38] S. V. Isakov and R. Moessner. Interplay of quantum and thermal fluctuations in a frustrated magnet. *Phys. Rev. B*, 68:104409, Sep 2003.

[39] H. C. Jiang, Z. Y. Weng, and D. N. Sheng. Density matrix renormalization group numerical study of the kagome antiferromagnet. *Phys. Rev. Lett.*, 101(11):117203, Sep 2008.

[40] A. Recati J.N. Fuchs and W. Zwerger. Oscillating casimir force between impurities in one-dimensional fermi liquids. *Phys. Rev. A*, 75:043615, 2007.

[41] A. Yamaguchi M. Hasegawa T. Inabe Y. Maruyama K. Awaga, T. Okuno and N. Wada. Variable magnetic interactions in an organic radical system of (m-n-methylpyridinium α-nitronyl nitroxide)$\cdot x^{-1}$: A possible kagomé antiferromagnet. *Phys. Rev. B*, 49:3975, 1994.

[42] H. Kageyama, K. Yoshimura, R. Stern, N. V. Mushnikov, K. Onizuka, M. Kato, K. Kosuge, C. P. Slichter, T. Goto, and Y. Ueda. Exact dimer ground state and quantized magnetization plateaus in the two-dimensional spin system $SrCu_2(BO_3)_2$. *Phys. Rev. Lett.*, 82:3168–3171, Apr 1999.

[43] K. Kanô and S Naya. Antiferromagnetism. the kagomé ising net. *Prog. Theor. Phys.*, 10:158–172, 1953.

[44] D. J. Klein. Exact ground states for a class of antiferromagnetic Heisenberg models with short-range interactions. *J. Phys. A: Math. Gen.*, 15:661–71, 1982.

[45] K. Kodama, S. Miyahara, M. Takigawa, M. Horvatic, C. Berthier, F. Mila, H. Kageyama, and Y. Ueda. Field-induced effects of anisotropic magnetic interactions in $srcu_2(bo_3)_2$. *J. Phys.: Condens. Matter*, 17:L61–L68, 1999.

[46] P. W. Leung and V. Elser. Numerical studies of a 36-site kagome antiferromagnet. *Phys. Rev. B*, 47:5459, 1993.

[47] D. I. Khomskii M. V. Mostovoy and J. Knoester. Frustrated spin model as a hard-sphere liquid. *Phys. Rev. Letters*, 90:147203, 2003.

[48] C. K. Majumdar and D. K. Ghosh. On next-nearest-neighbor interaction in linear chain. I. *J. Math. Phys*, 10:1388–98, 1969.

[49] M. Mambrini and F. Mila. RVB description of the low-energy singlets of the spin 1/2 kagome antiferromagnet. *Eur. Phys. J. B*, 17:651–659, 2000.

[50] J. B. Marston and C. Zeng. Spin-Peierls and spin-liquid phases of kagome quantum antiferromagnets. *J. Appl. Phys.*, 69:5962, 1991.

[51] P. Mendels, F. Bert, M. A. de Vries, A. Olariu, A. Harrison, F. Duc, J. C. Trombe, J. S. Lord, A. Amato, and C. Baines. Quantum magnetism in the paratacamite family: Towards an ideal kagomé lattice. *Phys. Rev. Lett.*, 98:077204, 2007.

[52] F. Mila. Low-energy sector of the $s = 1/2$ kagome antiferromagnet. *Phys. Rev. Lett.*, 81:2356–2359, 1998.

[53] G. Misguich, C. Lhuillier, B. Bernu, and C. Waldtmann. Spin-liquid phase of the multiple-spin exchange hamiltonian on the triangular lattice. *Phys. Rev. B*, 60:1064–74, 1999.

[54] G. Misguich, D. Serban, and V. Pasquier. Quantum dimer model on the kagome lattice: Solvable dimer-liquid and Ising gauge theory. *Phys. Rev. Lett.*, 89:137202, 2002.

[55] G. Misguich, D. Serban, and V. Pasquier. Quantum dimer model with extensive ground-state entropy on the kagome lattice. *Phys. Rev. B*, 67:214413, 2003.

[56] Grégoire Misguich and Claire Lhuillier. Two-dimensional quantum antiferromagnets. *arXiv:cond-mat*, 1:0310405, 2003.

[57] S. Miyahara and F. Mila. The effects of Dzyaloshinsky–Moriya interaction in the orthogonal dimer Heisenberg model for $\mathrm{srcu_2(bo_3)_2}$. *Progr. Theor. Phys. Suppl.*, 159:33–38, 2005.

[58] S. Miyahara, F. Mila, K. Kodama, M. Takigawa, M. Horvatic, C. Berthier, H. Kageyama, and Y. Ueda. The effects of intra-dimer Dzyaloshinsky–Moriya interaction on the properties of $SrCu_2(BO_3)_2$ in an external magnetic field. *J. Phys.: Condens. Matter*, 16:S911–S916, 2004.

[59] Shin Miyahara and Kazuo Ueda. Exact dimer ground state of the two dimensional heisenberg spin system $SrCu_2(BO_3)_2$. *Phys. Rev. Lett.*, 82:3701–3704, May 1999.

[60] R. Moessner and S. L. Sondhi. Ising models of quantum frustration. *Phys. Rev. B*, 63:224401, 2001.

[61] R. Moessner and S. L. Sondhi. An RVB phase in the triangular lattice quantum dimer model. *Phys. Rev. Lett.*, 86:1881, 2001.

[62] R. Moessner, S. L. Sondhi, and P. Chandra. Two-dimensional periodic frustrated Ising models in a transverse field. *Phys. Rev. Lett.*, 84:4457–60, 2000.

[63] R. Moessner, S. L. Sondhi, and P. Chandra. Phase diagram of the hexagonal lattice quantum dimer model. *Phys. Rev. B*, 64:144416, 2001.

[64] R. Moesssner. Magnets with strong geometric frustration. 2000.

[65] Tôru Moriya. Anisotropic superexchange interaction and weak ferromagnetism. *Phys. Rev.*, 120:91–98, Oct 1960.

[66] B. Nienhuis. Coulomb gas formulation of two-dimensional phase transitions. In C. Domb and J. L. Lebowitz, editors, *Phase Transitions and Critical Phenomena*, volume 11, pages 1–53. Academic Press, London, 1987.

[67] M. P. Nightingale and H. W. J. Blöte. Gap of the linear spin-1 heisenberg antiferromagnet: A monte carlo calculation. *Phys. Rev. B*, 33(1):659–661, Jan 1986.

[68] P. Nikolić and T. Senthil. Physics of low-energy singlet states of the kagome lattice quantum heisenberg antiferromagnet. *Phys. Rev. B*, 68:214415, 2003.

[69] H. Nojiri, H. Kageyama, K. Onizuka, Y. Ueda, and M. Motokawa. Direct observation of the multiple spin gap excitations in two-dimensional dimer system $srcu_2(bo_3)_2$. *J. Phys. Soc. Japan*, 68:2906–9, 1999.

[70] Z. Nussinov, C. D. Batista, B. Normand, and S. A. Trugman. High-dimensional fractionalization and spinon deconfinement in pyrochlore antiferromagnets. *Phys. Rev. B*, 75:094411, 2007.

[71] Oren Ofer and Amit Keren. Symmetry of the spin hamiltonian for herbertsmithite: A spin-$\frac{1}{2}$ kagome lattice. *Phys. Rev. B*, 79(13):134424, Apr 2009.

[72] Oren Ofer, Amit Keren, Emily A. Nytko, Matthew P. Shores, Bart M. Bartlett, Daniel G. Nocera, Chris Baines, and Alex Amato. Ground state and excitation properties of the quantum kagomé system $ZnCu_3(OH)_6Cl_2$ investigated by local probes. 2006.

[73] A. Olariu, P. Mendels, F. Bert, F. Duc, J. C. Trombe, M. A. de Vries, and A. Harrison. $^{1}7$O NMR study of the intrinsic magnetic susceptibility and spin dynamics of the quantum kagome antiferromagnet $ZnCu_3(OH)_6Cl_2$. *Phys. Rev. Lett.*, 100:087202, 2008.

[74] V. Meden P. W*ä*chter and K. Schoönhammer. Indirect forces between impurities in one-dimensional quantum liquids. 2007.

[75] Linus Pauling. The structure and entropy of ice and of other crystals with some randomness of atomic arrangement. *J. Am. Chem. Soc.*, 57:26802684, December 1935.

[76] K. S. Raman, R. Moessner, and S. L. Sondhi. SU(2)-invariant spin-1/2 hamiltonians with RVB and other valence bond phases. *Phys. Rev. B*, 72:064413, 2005.

[77] A. P. Ramirez. Strongly geometrically frustrated magnets. *Annu. Rev. Mater. Sci.*, 124:453–480, 1994.

[78] Ying Ran, Michael Hermele, Patrick A. Lee, and Xiao-Gang Wen. Projected-wavefunction-study of the spin-1/2 heisenberg model on the kagome lattice. *Phys. Rev. Lett.*, 98:117205, 2007.

[79] N. Read and S Sachdev. Valence-bond and spin-Peierls ground states of low-dimensional quantum antiferromagnets. *Phys. Rev. Lett.*, 62:1694–7, 1989.

[80] Marcos Rigol and Rajiv R. P. Singh. Kagome lattice antiferromagnets and Dzyaloshinsky–Moriya interactions. *Phys. Rev. B*, 76:184403, 2007.

[81] Marcos Rigol and Rajiv R. P. Singh. Magnetic susceptibility of the kagome antiferromagnet $ZnCu_3(OH)_6Cl_2$. *Phys. Rev. Lett.*, 98:207204, 2007.

[82] D. S. Rokhsar and S. A. Kivelson. Superconductivity and the quantum hard-core dimer gas. *Phys. Rev. Lett.*, 61:2376–79, 1988.

[83] B. Sriram Shastry and Bill Sutherland. Exact ground state of a quantum mechanical antiferromagnet. *Physica B*, 108:1069–1070, 1981.

[84] M. P. Shores, E. A. Nytko, B. M. Bartlett, and D. G. Nocera. A structurally perfect s=1/2 kagomé antiferromagnet. *J. Am. Chem. Soc.*, 127:13462–13463, 2005.

[85] David A. Huse Simeng Yan and Steven R. White. Spin liquid ground state of the $s = 1/2$ kagome heisenberg model. 2010.

[86] Rajiv R. P. Singh and David A. Huse. Ground state of the spin-1/2 kagome-lattice Heisenberg antiferromagnet. *Phys. Rev. B*, 76:180407(R), 2007.

[87] Rajiv R. P. Singh and David A. Huse. Triplet and singlet excitations in the valence bond crystal phase of the kagome lattice Heisenberg model. *Phys. Rev. B*, 77:144415, 2008.

[88] Stephenson. A structurally perfect s=1/2 kagomé antiferromagnet. *J. Phys*, 127:13462–13463, 2005.

[89] Raman K.S. Shtengel K. Tovar, M. Dzyaloshinskii–moriya interactions in valence–bond systems. *Phys. Rev. B*, 79:024405, 2009.

[90] Jan von Delft and Christopher L. Henley. Destructive quantum interference in spin tunneling problems. *Phys. Rev. Lett.*, 69:3326, 1992.

[91] N. Wada, T. Kobayashi, H. Yano, A. Yamaguchi T. Okuno, and K. Awaga. Observation of spin-gap state in two-dimensional spin-1 kagomé antiferromagnet m-MPYNN·BF_4. *J. Phys. Soc. Jpn.*, 66:961, 1997.

[92] Ch. Waldtmann, H.-U. Everts, B. Bernu, C. Lhuillier, P. Sindzingre, P. Lecheminant, and L. Pierre. First excitations of the spin 1/2 heisenberg antiferromagnet on the kagome lattice. *Eur. Phys. J. B*, 2:501, 1998.

[93] G. H. Wannier. Antiferromagnetism. the triangular ising net. *Phys. Rev.*, 79:357, 1950.

[94] F. Wegner. *J. Math. Phys*, 2259:12, 1971.

[95] X. G. Wen. Mean-field theory of spin-liquid states with finite energy gap and topological orders. *Phys. Rev. B*, 44:2664–72, 1991.

[96] Steven R. White. Density matrix formulation for quantum renormalization groups. *Phys. Rev. Lett.*, 69(19):2863–2866, Nov 1992.

[97] Supeng Kou Zi Cai, Shu Chen and Yupeng Wang. Two-dimensional spin-1 frustrated heisenberg model with valence-bond ground states. *Phys. Rev. B*, 76:054443, 2007.

[98] A. Zorko, S. Nellutla, J. van Tol, L. C. Brunel, F. Bert, F. Duc, J.-C. Trombe, M. A. de Vries, A. Harrison, and P. Mendels. Dzyaloshinsky–Moriya anisotropy in the spin-1/2 kagome compound $zncu_3(oh)_6cl_2$. *Phys. Rev. Lett.*, 101:026405, 2008.